
UNIVERSITY OF ICELAND

**Ph.D. Dissertation**
**in Chemistry**

# Calculations of photoinduced energy relaxation and atomic rearrangement of molecules

**Benedikt Orri Birgisson**

December 2024

FACULTY OF PHYSICAL SCIENCES

# Calculations of photoinduced energy relaxation and atomic rearrangement of molecules

Benedikt Orri Birgisson

Dissertation submitted in partial fulfillment of a
*Philosophiae Doctor* degree in Chemistry

Ph.D. Committee
Hannes Jónson
Gianluca Levi
Asmus Ougaard Dohn
Elvar Örn Jónsson

Opponents
Raffaela Cabriolu
Jakob Schiøtz

Faculty of Physical Sciences
School of Engineering and Natural Sciences
University of Iceland
Reykjavik, December 2024

Calculations of photoinduced energy relaxation and atomic rearrangement of molecules

(Photoinduced Energy Relaxation & Atomic Rearrangement)

Dissertation submitted in partial fulfillment of a *Ph.D.* degree in Chemistry



Faculty of Physical Sciences
School of Engineering and Natural Sciences
University of Iceland
Dunhagi 5
107 Reykjavik
Iceland

Telephone: 525-4000

Bibliographic information:
Benedikt Orri Birgisson, 2024, *Calculations of photoinduced energy relaxation and atomic rearrangement of molecules*, Ph.D.Dissertation, Faculty of Physical Sciences, University of Iceland, 120 pp.

Author ORCID: 0000-0001-9230-2249
ISBN: 978-9935-9826-1-2

Printing: Háskólaprent
Reykjavik, Iceland, December 2024

# Abstract

The excitation of molecules by the absorption of photons has wide applicability, for instance in sensitizers and photocatalysts for systems driven by energy carried by light. A key issue is how the energy is then distributed and how the atomic structure rearranges after the photoexcitation, as such processes can critically affect the outcome and efficiency of light energy conversion. The pathways of energy and atomic structure relaxation of three widely studied molecules, two binuclear photocatalytic transition metal complexes and one organic photoactive compound, are investigated using density functional theory (Density Functional Theory (DFT)) calculations. The vibrational decoherence and energy dissipation channels of the photoexcited $[Pt_2(P_2O_5H_2)_4]^{4-}$ (PtPOP) molecule in solution are studied using multiscale molecular dynamics simulations where the Excited State (ES) of the complex is calculated with a time-independent density functional approach. It is found that the energy delivered to the Pt-Pt pinching mode upon photoexcitation is released to the solvent through the ligand atoms rather than directly from the Pt atoms. Differences in energy relaxation channels in water and acetonitrile are explained in terms of the differences in solvation structure and interaction of the solvent molecules with the platinum atoms. The Ground State (GS) potential energy surface of the $[Ir_2(dimen)_4]^{2+}$ (dimen = para-diisocyanomenthane) (IrDimen) complex is explored to assist the interpretation of ultrafast experiments of the dynamics of conversion between two GS conformers induced by light absorption. A range of density functional approximations is assessed, finding that hybrid exchange-correlation functionals with added dispersion interactions are needed to reproduce the experimental observations. The minimum energy path between the two conformers is computed and a population analysis performed to support the experimentally observed depletion and restoration of the nearly equal GS populations. Lastly, the potential energy surface of the N,N'-dimethylpiperazine (DMP) cation, a diamine, is investigated with various density functional approximations. This has become an important test case for the balance between localized and delocalized charge density and has recently raised some controversy. The original hybrid functional of Becke as well as some double hybrid functionals produce a minimum on the energy surface corresponding to a localized electronic state where the charge sits mainly on one of the N-atoms, in addition to the global, delocalized state minimum with the charge evenly shared by the two N-atoms. But, commonly used functionals such as PBE and PBE0, as well as recent neural network trained functionals do not produce the localized state. It is also found that explicit Perdew-Zunger self-interaction correction produces a localized state, while downscaled correction by a half does not. The calculated energy surfaces for the DMP cation thus provide valuable information about the delicate balance between localized and delocalized charge distribution in the various density functional approximations.

# Ágrip

Örvun sameinda við upptöku ljóseinda hefur víðtæka notkun, til dæmis í ljósgjafaefnum fyrir kerfi sem eru knúin af orku frá ljósi. Lykilatriði þar er auðkenna hinar ýmsu rásir sem orkan getur dreifst um hvernig atóm endurröðun er háttað eftir ljósörvun þar sem slíkir ferlar geta haft gríðarleg áhrif á útkomu og skilvirkni á upptöku ljósorku. Dreifirásir orkulosunar og slökun á atómuppbyggingu þriggja víð rannsakaðra sameinda, tveggja ljóshvatandi flóka sem eru með tvíkjarna hliðarmálma og lífræn sameind sem er ljósvirk, eru kannaðar með útreikningum byggðum á þéttnifallskenningu (DFT). Titringsóstyrkur og orkulosunarleiðir ljósörvaðrar PtPOP flóka í lausn eru rannsakaðar með fjölþátta sameindahreyfingarhermun, þar sem örvuða ástandið er reiknað með tíma óháðri þéttnifallsnálgun. Niðurstöður sýna að orkan sem berst til Pt-Pt klemmuhamsins við ljósörvun losnar út í leysinn í gegnum tengla flókans fremur en beint frá Pt atómunum. Munurinn á orkulosunarleiðum í vatni og acetonítríl er skýrður með mismun í byggingu og víxlverkun leysissameinda við platínuatómin. Orkuyfirborð grunnástands IrDimen flókans er kannaður til að styðja túlkun á ofurhraðri tilraunadýnamík við umbreytingu milli tveggja stellingarhverfa við örvun með ljósi. Ýmis felli byggð á þéttnifallskenningunni eru metnar, og kemur í ljós að hýbríð felli að viðbættum dreifiáhrifum eru nauðsynleg til að endurskapa tilraunaniðurstöður. Lágmarksorkuleiðin milli stellingarhverfa er reiknuð og framkvæmd til að styðja við tilraunaathuganir á rýrnun og endurheimt nánast jafns stór hluta af stellingarhverfunum tveimur. Að lokum var orkuyfirborð DMP katjónarinnar, tvíamíns, rannsakað með ýmsum fellum byggt á þéttnifallskenningu. Þetta hefur orðið mikilvægt prófunartilvik til að skoða jafnvægið milli staðbundinnar og óstaðbundinnar hleðsluþéttleika og hefur nýlega vakið umræður. Upprunalega hýbríð fellið frá Becke sem og nokkur tvöföld hýbríð felli mynda lágmark á orkufletinum sem samsvarar staðbundnu rafrænu ástandi þar sem hleðslan situr að mestu á einu af N-atómunum, til viðbótar við lágmark óstaðbundins ástands þar sem hleðslan er jafnt dreifð milli tveggja N-atómanna. Algeng felli eins og PBE og PBB0, ásamt nýlegu taugakerfisþjálfuðu felli, mynda ekki staðbundna ástandið. Einnig kemur í ljós að sjálfsvíxlverkunarleiðréttingu Perdew-Zunger myndar staðbundið ástand, en niðurstillt leiðrétting um helming gerir það ekki. Útreiknuðu orkufletirnir fyrir DMP katjónina veita því dýrmætar upplýsingar um fínstillt jafnvægi staðbundinnar og óstaðbundinnar hleðsludreifingar í mismunandi þéttnifallsnálgunum.

# Table of Contents

# List of Figures

# List of Tables

# List of Publications

**Publications included in this thesis**

**Paper I:** Benedikt O. Birgisson, Asmus Ougaard Dohn, Hannes Jónsson, and Gianluca Levi. Decoherence and vibrational energy relaxation of the electronically excited PtPOP complex in solution. *Accepted for publication in Journal of Chemical Physics*

**Paper II:** Natalia E. Powers-Riggs, Benedikt O. Birgisson, Sumana L. Raj, Elisa Biasin, Philipp Lenzen, Diana Bregenholt Zederkof, Morten Haubro, Dagrún K. V. Tveiten, Robert W. Hartsock, Tim B. van Driel, Kristjan Kunnus, Matthieu Chollet, Joseph S. Robinson, Silke Nelson, Ruaridh Forbes, Kristoffer Haldrup, Kasper S. Pedersen, Gianluca Levi, Asmus Ougaard Dohn, Hannes Jónsson, Klaus Braagaard Moller, Adi Natan,* Martin Meedom Nielsen, and Kelly J. Gaffney, Characterization of Deformational Isomerization Potential and Interconversion Dynamics with Ultrafast X-ray Solution scattering *J. Am. Chem. Soc. 2024, 146, 20, 13962–13973*

.

**Paper III:** Benedikt O. Birgisson, Hemanadhan Myneni, Elvar Ö. Jónsson, Ragnar Bjornsson, and Hannes Jónsson, Localized and Delocalized Charge Distribution in a Diamine Cation: A Challenging Test for Density Functionals. *To be submitted*

**Other publications not included in this thesis**

**Paper IV:** Vilhjálmur Ásgeirsson, Benedikt O. Birgisson, Ragnar Bjornsson, Ute Becker, Frank Neese, Christoph Riplinger, and Hannes Jónsson, Nudged Elastic Band Method for Molecular Reactions Using Energy-Weighted Springs Combined with Eigenvector Following. *J. Chem. Theory Comput. 2021, 17, 8, 4929–4945*

# Abbreviations

**CI** Climbing Image

**CI-NEB** Climbing Image Nudged Elastic Band

**CPCM** Conductor-like Polarizable Continuum Model

**DFT** Density Functional Theory

**DMP** N,N'-dimethylpiperazine

**ES** Excited State

**GGA** Generalized Gradient Approximations

**GS** Ground State

**HTST** Harmonic Transition State Theory

**IrDimen** $[Ir_2(dimen)_4]^{2+}$ (dimen = para-diisocyanomenthane)

**L-J** Lennard-Jones

**MD** Molecular Dynamics

**MEP** Minimum Energy Path

**MM** Molecular Mechanics

**MOM** Maximum Overlap Method

**NEB** Nudged Elastic Band

**OTAS** Optical Transient Absorption Spectroscopy

**PES** Potential Energy Surface

**PtPOP** $[Pt_2(P_2O_5H_2)_4]^{4-}$

**PZ-SIC** Perdew-Zunger Self Interaction Correction

**SCF** Self Consistent Field

**SIC** Self Interaction Correction

**TST** Transition State Theory

**QM** Quantum Mechanics

**QM/MM** Quantum Mechanics / Molecular Mechanics

**XSS** X-ray Solution Scattering

# Acknowledgements

I would like to thank the Icelandic Research fund for funding this work.

# 1 Introduction

In pursuit of sustainable energy solutions and environmental remediation, the development of efficient photocatalytic systems presents significant potential. These systems absorb light to initiate chemical reactions such as pollutant degradation, hydrogen production, organic synthesis and energy storage with the promise of transforming multiple industries. In order to accelerate the identifiction and design of photocatalytic systems, quantum chemical calculations play a crucial role, as they can provide insights into the electronic structure of photoactive molecules and materials at the atomic levels, which are often not available experimentally. By combining the theoretical predictions with experimental observations, the discovery of next-generation photocatalytic materials with transformative potential to address global energy and environmental challenges can be accelerated.

Using methods such as DFT[1], [2], the energy levels, electronic transitions, and charge transfer processes that are essential for photocatalytic activity can be predicted. These calculations can also provide mechanistic insights into the pathways of energy and structural relaxation unfolding after light absorption when combined with energy path and molecular dynamics methods. By computing reaction mechanisms, energy profiles, and spectroscopic properties, quantum chemical methods can elucidate the complex kinetics and dynamics of photocatalytic reactions, assisting in the design of more efficient and selective catalysts[3], [4].

Despite their promise, quantum chemical calculations face challenges related to the accurate description of excited states, transient species, and complex reaction environments. Ongoing research efforts focus on the development of advanced computational methodologies, improving accuracy and scalability. The development of multiscale modeling approaches is one way to address these challenges[5].

This dissertation consists of three articles presenting the results of calculations of the energy relaxation and atomic structural rearrangements induced by photoexcitation in three well-studied molecules, with a preceding introduction to the theoretical and computational methods applied in these studies. The 2nd chapter introduces the electronic structure method used, namely DFT together with the corrections employed in the present studies to improve the commonly used density functional approximations.

The 3rd chapter outlines the multiscale simulation scheme used in article I. The 4th chapter introduces the methods used for the exploration of potential energy surfaces in articles II-III. The 5th chapter illustrates the approach used to identify the channels of vibrational energy relaxation of a photoexcited molecule, which is used in acticle I. Finally, a summary of articles I-III can be found in the 6th chapter.

# 2 Electronic Structure Methods

In this chapter, the electronic structure methods used for the computational study of atoms and molecules in Articles I-III are presented. First, the widely used DFT is presented, followed by the corrections to standard Kohn-Sham functionals[2] used in Articles I-III. Common Kohn-Sham functionals fail to describe long-range interactions, which are important in, e.g., bimetallic complexes. Long-range dispersion interactions can be included in DFT using Grimme's dispersion corrections [6], which are here used to get a better description of the two bimetallic complexes studied in Article I-II. Another limitation of DFT is the presence of the self-interaction of electrons. Sometimes, the self-interaction is not problematic, thanks to a cancellation of errors. However, in systems with a localized electron, the application of a Self Interaction Correction (SIC) is necessary, as shown in Article III for an organic molecule. Variational, time-independent DFT calculations of ESs offer in many cases an improvement over the commonly used time-dependent DFT approach. However, they can prove difficult to perform in practice. This is due to the fact that the excited state solutions represent saddle points on the electronic energy surface, and therefore, variational collapse to the GS can occur. Here, a novel direct optimization approach based on saddle point search methods [7]–[10]together with Maximum Overlap Method (MOM) [11] is used in Articles I and III.

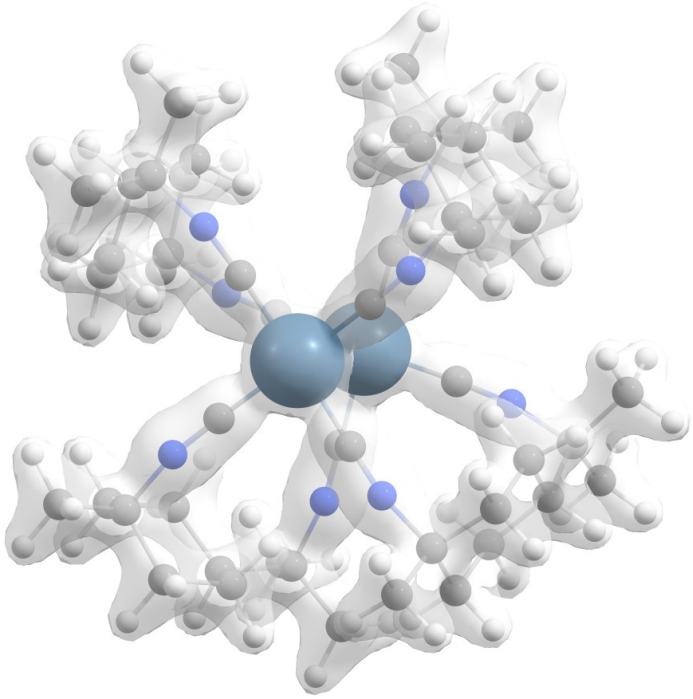

*Figure 2.1. Isosurface representation of the electron density for the short isomer of IrDimen, studied in article II, calculated with Kohn-Sham DFT.*

## 2.1 Density Functional Theory

The theoretical study of atoms and molecules requires a methodology providing a reasonably accurate description of the electronic structure. The methodology should also be efficient enough to enable studies of systems including several atoms. DFT has seen widespread application as it provides relative accuracy and efficiency. It is based on the principles of quantum mechanics and provides a computationally efficient approach to understand the behavior of electrons in complex systems.

At the core of DFT lie the Hohenberg-Kohn theorems, which provide the theoretical foundation of the method[12]. The first theorem states that the GS electronic density, $\rho$(r), determines the external potential, $V_{ext}$(r), given by:

$$V_{ext}(r) = V_{ext}[\rho(r)] \tag{1}$$

The second theorem states that there exists a universal function, $F[n(\mathrm{r})]$, of the electron density, which determines the GS energy, $E_0$, for a given external potential:

$$E_0 = F[\rho(r)] + \int \rho(r) V_{ext}(r) dr \tag{2}$$

The Kohn-Sham equations provide a practical way to solve the electronic structure problem in DFT[2]. They introduce a set of fictitious non interacting electrons moving in an effective potential, $V_{eff}$(r), such that the electron density of these fictitious electrons matches the electron density of interacting electrons. The Kohn-Sham equations are:

$$(-\frac{1}{2}\nabla^2 + V_{eff}(r))\phi_i(r) = \varepsilon_i \phi_i(r) \tag{3}$$

where $\phi_i$(r) are the Kohn-Sham orbitals and $\varepsilon_i$ the corresponding orbital energies. The exchange-correlation functional, denoted as $E_{XC}[\rho(\mathrm{r})]$, approximates the exchange and correlation effects between electrons[13]. It is typically the most challenging part of DFT due to the lack of an exact expression and requires approximations. The total energy functional in DFT is expressed as.

$$E[\rho(r)] = T[\rho(r)] + V_{ext}[\rho(r)] + \int\int \frac{\rho(r)\rho(r')}{|r-r'|} dr dr' + E_{XC}[\rho(r)] \tag{4}$$

Kohn-Sham DFT finds widespread applications in various fields such as chemistry, physics, materials science, and biology[14]. However, challenges remain in accurately describing van der Waals interactions[15], removing the self-interaction error, and calculating excited electronic states, which require further advancements in computational methodologies and approximations, as described in the next section.

### 2.1.1 Dispersion Interaction

Dispersion interaction, in the context of molecular chemistry and physics, refers to the attractive forces between molecules or atoms that arise due to fluctuations in their electron distributions. Even in nonpolar molecules or atoms, electrons are in constant motion, leading to transient dipole moments. These induced dipoles can then induce similar dipoles in

neighboring molecules, resulting in an attractive force between them. These forces are often referred to as van der Waals forces, London dispersion forces, or simply dispersion forces, and play a crucial role in determining the properties of materials, including their structure, stability, and interactions[16].

Grimme's approximation to the dispersion interaction [6], [17] is designed to address the deficiencies of standard DFT functionals by adding an empirical correction term to the total energy expression [18]. This correction term accounts for the attractive dispersion forces between molecules by approximating it as a pairwise interaction of atoms and their distance-dependent contributions to the energy:

$$E_{disp} = -\sum_{i<j}\sum_{n=3}^{5} \frac{C_{2n}^{ij}}{r_{ij}^{2n}} f_n(\alpha_{ij}^D) \tag{5}$$

where $C_n^{ij}$ is a dispersion coefficent for atom pairs $i$ and $j$ , $r_{ij}$ the distance between atoms $i$ and $j$, and $f_n(\alpha_{ij}^D)$ a damping function that turns off the interaction at short distance. The total energy $E_{total}$ in a DFT-D calculation is the sum of the electronic energy $E_{elec}$ obtained from a Kohn-Sham DFT functional plus the long range dispersion energy contribution $E_{disp}$:

$$E_{total} = E_{elec} + E_{disp} \tag{6}$$

This represents an efficient but highly approximate way to include dispersion interactions in quantum mechanical calculations and Grimme has been steadily improving his DFT-D methodology. The first release of DFT-D only had a two-body dispersion term with a simple damping function. This damping function was improved upon with the DFT-D2 version. With the release of DFT-D3, an optional three body dispersion term is added and further improvements made to the damping function as well as the addition of a geometry-dependent dispersion coefficient, which takes into account the geometric space of each atom and parametrizes accordingly, improving the accuracy. In the most recent release DFT-D4 a many body dispersion term was added as well as a charge dependent term. Furthermore a reparametrization of the empirical parameters was performed. This again significantly improves the accuracy of the DFT-D methodology as can be seen in Article II.

### 2.1.2 Self-Interaction Correction

The self-interaction of electrons in Kohn-Sham DFT functionals arises from the use of only the total electron density in the estimate of the classical Coulomb interaction, often referred to as the Hartree term. Even if the system only contains a single electron, this estimate gives a non-zero interaction. The exchange-correlation term in the functional attempts to cancel out the self-interaction error, but a semi-local approximation cannot fully cancel the non-local Coulomb self-interaction. This leads to inaccuracies in determining the energy of systems, especially for atoms and molecules with localized electrons. The remaining error can be somewhat mitigated with the use of hybrid functionals, which include a portion of the Fock exchange from Hartree-Fock theory. Alternatively, an explicit self-interaction correction can be applied as proposed by Perdew and Zunger, Perdew-Zunger Self Interaction Correction (PZ-SIC) [19]. This is an orbital-by-orbital correction and the self-interaction corrected energy $E_{SIC}$ is:

$$E_{SIC} = E_{DFT}[\rho] - \sum_{i=1}^{N_e} (E_H[\rho_i] + E_{XC}[\rho_i]) \tag{7}$$

where $E_{DFT}$ is the total energy computed using a Kohn-Sham DFT functional, $E_H[\rho_i]$ and $E_{XC}[\rho_i]$ are the Hartree and exchange-correlation energy evaluated for a single orbital, and $\rho_i$ is the orbital density of orbital $i$.

The PZ-SIC has been found to improve the accuracy of DFT calculations[20], [21], particularly for systems with localized electrons, such as transition metals, and electrons in diffuse orbitals, such as dipole-bound molecular anions and Rydberg states[22], [23]. However, it can also overcorrect in some cases, such as for atomization energies of molecules. For these cases, a scaled down version of PZ-SIC has been found to perform better[24], [25].

## 2.2 Excited State Calculations

Electronic excitations, where electrons are excited to energy levels above the ground state, typically occur due to the absorption of photons by molecules or materials. High level wave function methodologies, such as multireference configuration interaction and coupled cluster methods, provide accurate calculations of excited electronic states[26]. However, the computational cost of these methods increases rapidly with the system size, significantly limiting their applicability to large systems or to the simulation of the dynamics of atoms in excited states. Thus, less expensive methods have been developed, which calculate excited states more efficiently.

A commonly used method for calculations of excited states of large systems is the time-dependent formulation of DFT (TD-DFT)[27], [28]. Practical implementations of TD-DFT typically employ linear-response theory and ground state functionals within the adiabatic approximation, neglecting the time dependence of the exchange-correlation kernel. With these approximations, TD-DFT usually provides an accurate description of low-lying excited states with character of valence excitation. However, it tends to fail for excitations involving a large change of the electron density. For example, when TD-DFT is employed with a semi-local functional, it is prone to severely underestimating the excitation energy of charge transfer excited states[29], [30]. Hybrid functionals, particularly range-separated functionals that add Fock exchange in the long-range part of the interaction potential, can improve the results[31], [32]. However, this comes at an increase of the computational cost, and moreover the fraction of Fock exchange and the range separation parameters are typically treated as empirical parameters, meaning that they are expected to perform well only for the systems for which they have been optimized.

Time-independent, variational formulations of DFT for excited states have also been developed[33]–[35]. While these extensions of DFT provide the theoretical foundations for calculating excited states in a time-independent density functional framework, they often involve state-specific functionals with a complicated form. A pragmatic approach is to use ground state functionals and compute the excited states as solutions to the Kohn-Sham equations with energy higher than the ground state[36]. This approach is often referred to as ΔSelf-Consistent Field (ΔSCF), indicating that the excitation energy is computed as the difference between the energy of the excited and ground states, both obtained self-consistently. Although this approach is less commonly used than TD-DFT, it provides a better approximation of Rydberg[37], [38], charge transfer[29], [39] and doubly excited states[36], often yielding good results already with semi-local functionals. Furthermore, since the excited states are calculated variationally, atomic forces can be computed using the Hellman-Feynman

theorem, making it possible to perform geometry optimizations and molecular dynamics simulations in excited states[40]–[42]. This is exploited in article I, where molecular dynamics simulations of a photoexcited complex are presented.

Since the variationally optimized excited states correspond to solutions to the Kohn-Sham equations higher in energy than the ground state with a non-aufbau occupation of the orbitals, any variation of the orbitals leading to the ground state lowers the energy. Thus, excited states typically represent saddle points on the surface describing the variation of the energy as a function of the electronic degrees of freedom[43]. This poses a challenge to the variational optimization of orbitals in time-independent density functional calculations of excited states. SCF algorithms commonly used for ground state calculations, which are based on sequential diagonalization of the Kohn-Sham matrix and interpolation schemes, often struggle in excited state calculations, leading to collapse to the ground state or exhibiting erratic convergence behavior[7], [44]. A common approach to reduce the risk of variational collapse is the Maximum Overlap Method (MOM)[11], [45]. However, MOM alone does not ensure convergence to a target saddle point on the electronic energy surface. In the work presented here, a recently developed methodology is used[7], [10], which is based on direct optimization of the orbitals using quasi-Newton algorithms for saddle points.

### 2.2.1 Direct Optimization

In direct optimization, the orbitals are variationally optimized by directly finding a unitary transformation $\mathbf{U}$ that makes the energy stationary:

$$\boldsymbol{\phi}_{\text{stat}} = \mathbf{U}\boldsymbol{\phi}_0 \tag{8}$$

where $\boldsymbol{\phi}_0$ is the vector of initial guess orbitals, and $\boldsymbol{\phi}_{\text{stat}}$ is the vector of optimal orbitals. The unitary transformation is conveniently parametrized as the exponential of an anti-Hermitian matrix $\boldsymbol{\kappa} = -\boldsymbol{\kappa}^{\dagger}$:

$$\mathbf{U} = e^{\boldsymbol{\kappa}} \tag{9}$$

In this way, stationary points of the electronic energy surface can be found by optimizing the energy with respect to the elements of $\boldsymbol{\kappa}$, and since anti-Hermitian matrices form a linear space, this can be done using efficient iterative unconstrained optimization techniques, such as quasi-Newton algorithms. The excited state calculations performed in this work use linear combination of atomic orbital (LCAO) basis sets, where the initial orbitals are expanded in a linear combination of basis functions $\boldsymbol{\varphi}$:

$$\boldsymbol{\phi}_0 = \boldsymbol{\varphi}\boldsymbol{C}_0 \tag{10}$$

Therefore, in this case, the objective of direct optimization is to find a set of optimal coefficients making the energy stationary:

$$\boldsymbol{C}_{\text{stat}} = \boldsymbol{C}_0 e^{\boldsymbol{\kappa}} \tag{11}$$

The initial orbitals for an excited state calculation are usually chosen as the orbitals from a ground state calculation with occupation numbers changed to reflect the promotion of electrons from occupied to unoccupied orbitals. The initial electronic Hessian is constructed using a diagonal approximate Hessian with elements[46], [47]

$$\frac{\partial^2 E}{\partial \kappa_{ij}^2} \approx -2\left(\varepsilon_i - \varepsilon_j\right)\left(f_i - f_j\right), \tag{12}$$

where $\varepsilon_i$ and $f_i$ are the orbital energies and occupation numbers, respectively. Thus, the initial electronic Hessian has one negative eigenvalue for each pair of occupied-unoccupied orbitals where the unoccupied orbital is lower in energy, i.e. for each pair of orbitals involved in excitations of electrons between the ground state occupied and unoccupied spaces. Since excited states correspond to saddle points on the electronic energy surface, a quasi-Newton method that is able to propagate a non-positive-definite approximate Hessian is needed. In article I, a limited-memory symmetric rank-one (L-SR1) algorithm is used, as implemented in the GPAW software[48]. A description of the calculation of the energy gradient and other details of the implementation can be found in references[7], [10].

While designed to converge to saddle points, the direct optimization method with the L-SR1 quasi-Newton algorithm can still be affected by variational collapse. Therefore, it is usually supplemented with MOM (see next section). A more robust direct optimization method that does not require MOM has been recently developed[43] in the research group were the present work was conducted (the calculations of article I were performed before these latest developments).

### 2.2.2 Maximum Overlap Method

In order to further reduce the risk of variational collapse in the ES calculations presented in article I, the MOM [11], [45] is utilized. It reduces the risk of converging to a solution other than the desired excited state by selecting the occupied orbitals as the orbitals that overlap the most with the orbitals of previous iterations or with the orbitals of the initial guess.

At each iteration of the SCF, the following projections of the orbitals on the space of the reference orbitals are computed

$$\omega_j = \sqrt{\sum_{i=1}^{N_e} |O_{ij}|^2} \tag{13}$$

where $O_{ij}$ are the elements of the overlap matrix

$$O_{ij} = \langle \phi_i^{ref} | \phi_j \rangle \tag{14}$$

Then, the $N_e$ orbitals with largest $\omega_j$ are occupied. Thus, MOM ensures that at each iteration, the orbitals with the largest overlap with the reference orbitals are occupied, reducing the risk that the optimization drifts away from the saddle point closest to the initial guess.

# 3 Multiscale Simulations

Within, this chapter, the multiscale simlulation scheme used in Article I is presented. Such hybrid approach allows to efficiently simulate large systems. The area of interest is simulated with a higher level of accuracy, while the rest of the system is described with a more efficient but less accurate methodology.

In Article I, the QM/MM method[49] is used, modelling a solvated complex with Quantum Mechanics (QM) and the surrounding solvent molecules with classical Molecular Mechanics (MM). The interactions between the two regions are computed according to a so-called electrostatic embedding scheme[50], where the long-range electrostatic interactions are described using the classical Coulomb potential of point charges in the MM region embedded in the effective Hamiltonian of the QM region, while short-range repulsive and attractive interactions are represented with a L-J[51] potential. Finally, in order to simulate the nonequilibium time evolution of a photoexcited molecule in solution the nuclei are propagated classically with a Langevin thermostat applied to solvent molecules to include a heat bath.

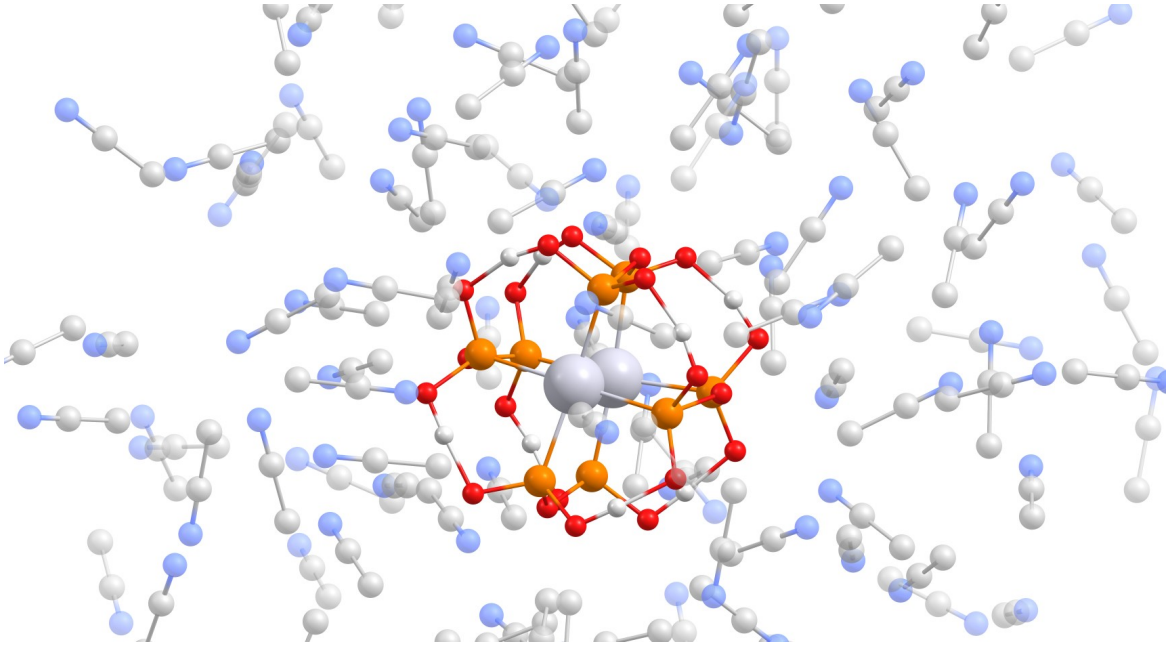

*Figure 3.1. Visualization of a QM/MM system. Here, the electronic structure of the solvated PtPOP complex is described with DFT, a higher level of theory than the classical force field potentials used to describe the surrounding acetonitrile solvent molecules (see Article I).*

## 3.1 Quantum Mechanics/Molecular Mechanics

QM methods solve the Schrödinger equation to obtain accurate descriptions of electronic structure and chemical bonding. These methods include ab initio techniques such as Hartree-Fock theory, post-Hartree-Fock methods and DFT, which has been briefly described in the previous chapter. QM calculations provide detailed information about bond breaking and formation, electronic transitions, and reactive intermediates. The MM part approximates the potential energy surface of a system using classical force fields, which describe interatomic interactions based on empirical parameters. MM methods are computationally efficient and can handle large systems. However, they cannot accurately describe chemical reactions and electronic structure effects. Therefore, they are most suited for modeling an environment, such as a solvent, a protein, and other biomolecules, where it is not important to describe large electronic rearrangements.

The total energy in a QM/MM additive scheme is the sum of contributions from the QM region, the MM region, and the interaction between these two regions:

$$E_{total} = E_{QM} + E_{MM} + E_{QM/MM} \tag{15}$$

where $E_{QM}$ is the energy obtained with QM calculations, $E_{MM}$ is the energy obtained with classical MM methods and $E_{QM/MM}$ is the interaction between the QM and MM regions, which is handled in various ways depending on the coupling method. This hybrid approach allows for the study of complex chemical systems where both quantum effects and the interactions with an environment play significant roles[52], [53].

### 3.1.1 Long-Range Electrostatic Interactions

Electrostatic embedding involves embedding the QM region, where the description of electronic structure effects is important, within the MM environment, which represents the rest of the system[50], [53], [54]. This embedding ensures that the QM region is influenced by the electrostatic field generated by the surrounding MM atoms, i.e. the QM region is polarized by the MM region. In electrostatic embedding, the electrostatic potential generated by the MM point charges is included in the QM Hamiltonian as an external potential and is expressed as:

$$V_{ext} = -\sum_{i \in MM} \frac{q_i}{|\mathbf{r} - \mathbf{r}_i|} \tag{16}$$

where $q_i$ and $\mathbf{r}_i$ are the charge and positions of the $i$-th MM atom, and $\mathbf{r}$ are the positions of the QM electrons. $V_{ext}$ represents the potential of Coulomb interaction between QM electrons and MM point charges. This potential acts on the QM electrons, affecting their energies and wave functions, while the QM electrons in turn contribute to the total electrostatic potential experienced by the MM atoms[55], [56].

### 3.1.2 Short-Range Interactions

In the context of QM/MM simulations, the L-J potential plays a crucial role in describing non-bonded interactions between atoms or molecules within the classical MM region and between the MM and QM regions. It represents the van der Waals interactions, which contribute significantly to the overall stability and structure of molecular systems. The L-J potential is a simple yet effective model used to describe the interactions between neutral

atoms or molecules. It consists of two terms: a short-range repulsive and attractive terms. Mathematically, the L-J potential $V_{LJ}$ between two atoms or molecules is given by:

$$V_{LJ}(r) = 4\varepsilon[(\frac{\sigma}{r})^{12} - (\frac{\sigma}{r})^{6}] \tag{17}$$

where $r$ is the distance between atoms, $\varepsilon$ is the depth of the potential well, and $\sigma$ is the distance of the potential well.

While the L-J potential provides a useful approximation for non-bonded interactions in QM/MM simulations, it is important to consider its limitations, such as the neglect of electronic polarization effects[57], [58] and the reliance on empirical parameters.

## 3.2 Molecular Dynamics

Langevin dynamics is a computational method used to simulate the classical dynamics of atoms in molecular systems in the presence of thermal fluctuations and frictional forces[59]. In QM/MM simulations, Langevin dynamics is typically employed for the classical MM region, incorporating both the effects of classical interatomic interactions and the influence of thermal fluctuations on molecular motion, while the QM region is propagated in the microcanonical ensemble. Langevin dynamics accounts for the effects of thermal fluctuations by introducing random forces that mimic the collisions between particles. Additionally, frictional forces are included to simulate the damping effect experienced by molecules as they move through a viscous environment, such as a solvent[60]. The equation of motion for a particle in Langevin dynamics is described by:

$$m\frac{d^2r}{dt^2} = -\nabla V(r) - \gamma\frac{dr}{dt} + R(t) \tag{18}$$

where $m$ is the mass of the particle, $\frac{d^2r}{dt^2}$ is the acceleration, $\nabla V(r)$ is the force derived from the potential energy, $\gamma\frac{dr}{dt}$ represents the frictional force, with $\gamma$ as the friction coefficient,and $R(t)$ is a random force term representing thermal fluctuations, with a zero mean and variance proportional to the temperature.

For the nonequilibrium molecular dynamics simulations presented in Article I, the Langevin thermostat is applied only to solvent molecules far from the solute, while the PtPOP complex and the closest solvent molecules are not coupled to a heat bath, to minimize the influence of the thermostat on the dynamics of the complex and solvation shell. The thermostat is gradually switched on, increasing the friction coefficient linearly from 0 to 1 $ps^{-1}$ within a 2 Å buffer region extending radially in the simulation cell starting from a radius of 12 Å from the geometric center of the solute.

# 4 Mechanism and rate of transitions

In this chapter, the theories and methods used in Articles II-III to explore mechanisms and rates of transitions on a given Potential Energy Surface (PES) are presented. First, the PES is scanned between minima with the Nudged Elastic Band (NEB) method, obtaining a MEP and the transition state between two minima. With these critical points identified, Harmonic Transition State Theory (HTST) can be applied to obtain the reaction rate of a given reaction and subsequently population analysis can be performed. Key processes such as photoexcitation, vibrational relaxation, internal conversion, intersystem crossing, and reaction pathways all depend on how the molecule moves on and between different acPESs. Understanding the structure of these surfaces especially at key points like conical intersections and reaction coordinates is crucial for predicting the behavior of molecules following photoexcitation.

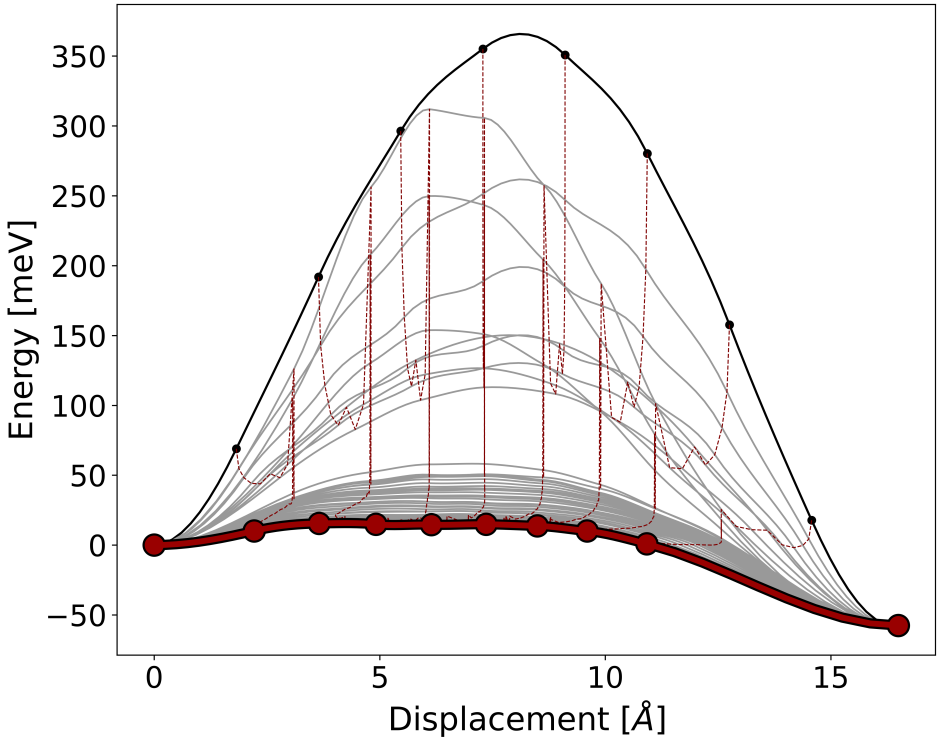


*Figure 4.1. NEB optimization profile of the interversion between the long and short isomer of IrDimen. Here, the elastic band is optimized from an inital guess towards the MEP, revealing a very flat energy surface with a low barrier height.*

## 4.1 Nudged Elastic Band Method

The NEB method is a computational technique used to find the MEP or transition pathway between two stable configurations or states of a system[61]. It is particularly useful for studying chemical reactions, phase transitions, and other processes involving the rearrangement of atoms or molecules[62], [63]. In NEB, the MEP is represented as an elastic band connecting the initial and final states, where the band is subject to both internal elastic forces and external forces that drive the system to the MEP. The elastic band is discretized into a set of images and the positions of these images are iteratively optimized to minimize the energy of the band. The total force acting on an image $i$ in the NEB method is divided into two components, the perpendicular component of the true force from the potential energy surface that pushes the image toward the MEP given as:

$$F_i^{\perp} = -\nabla V(r_i) + (\nabla V(r_i) \cdot \hat{\tau}_i)\hat{\tau}_i \tag{19}$$

where $\nabla V(r_i)$ is the gradient of the potential energy at image $i$, and $\hat{\tau}_i$ is the tangent to the path at image $i$ and the spring force, which keeps the images evenly spaced along the band given as:

$$F_i^{||} = k_i[(r_{i+1} - r_i) - k_{i-1}(r_i - r_{i-1})] \cdot \hat{\tau}_i \hat{\tau}_i \tag{20}$$

where $k$ is the spring constant, and $r_i$ represents the position of the $i$-th image. The forces from both components are then combined as:

$$F_i = F_i^{\perp} + F_i^{||} \tag{21}$$

This combined force is used to optimize the pathway to ensure that the images converge to the MEP. The Climbing Image Nudged Elastic Band (CI-NEB) method is an extension of NEB, designed to improve the accuracy of the highest energy point along the path and thereby the estimate of the activation energy[64]. In the standard NEB method, all images between the reactant and product states are optimized simultaneously along the MEP, but point of highest energy along the MEP, which is a saddle point on the PES is not explicitly targeted. CI-NEB addresses this by refining the highest energy image to converge directly to the saddle point. In CI-NEB, the image with the highest energy (Climbing Image (CI)) is identified, and the forces acting on it modified to eliminate the spring force and drive it up in energy. Specifically, the parallel component of the true force is inverted, allowing this image to climb to the saddle point:

$$F_{CI} = -\nabla V(r_i) + 2(\nabla V(r_i) \cdot \hat{\tau}_i)\hat{\tau}_i \tag{22}$$

This modification ensures that the climbing image moves up to the point of maximum energy along the path, thus providing a more accurate location of the saddle point, and thereby the transition state.

## 4.2 Harmonic Transition State Theory

Classical Transition State Theory (TST)[65] postulates that the rate of a chemical reaction is determined by the rate at which reactant molecules cross a transition state dividing surface. The key assumption is that once a trajectory crosses the dividing surface and is heading away

from the reactant region, it represents a reactive trajectory. Recrossings of the dividing surface are neglected. TST provides an expression for the rate constant $k$ of a reaction as:

$$k = \frac{k_B T}{h} \, e^{-\Delta G^{\ddagger}/k_b T} \tag{23}$$

where $k_B$ is the Boltzmann constant, $T$ is temperature, $h$ is the Planck constant, and $\Delta G^{\ddagger}$ the Gibbs free energy of activation. TST is a fundamental method in chemical kinetics that provides a theoretical framework for predicting the rate of chemical reactions based on the properties of the energy surface. The harmonic approximation, HTST, builds upon the principles of classical transition state theory but makes the further approximation that the PES near the initial state minimum and within the transition state can be approximated as harmonic[66], [67]. This is expressed as:

$$k = \frac{k_B T}{h} \frac{Q^{\ddagger}_{vib}}{Q^{R}_{vib}} \, e^{-\Delta E^{\ddagger}/k_b T} \tag{24}$$

where $Q^{\ddagger}_{vib}$ is the vibrational partition function of the transition state, $Q^{R}_{vib}$ is the vibrational partition function of the reactant, $\Delta E^{\ddagger}$ is the energy difference between the reactant minimum and the saddle point. HTST is an approximation to TST by incorporating harmonic approximations for the vibrational modes of the reactant and transition states.

# 5 Calculation of Energy Fluxes

In the following chapter, the method newly introduced in article I, used to map the energy flow of vibrational relaxation within a QM/MM framework is presented. Vibrational relaxation, where an excited molecule loses vibrational energy and returns to a lower energy state, is a crucial process in Molecular Dynamics (MD), as it impacts phenomena such as heat transfer, molecular reactivity, and the efficiency of energy conversion. The study of vibrational relaxation to understand how energy dissipation occurs in molecular systems in an environment, such as a solvent, is therefore essential.

A novel approach to estimate the flux of excess vibrational energy of a photoexcited molecule in solution within a QM/MM framework is presented in article I. First the vibrational modes of the solute are computed, and then the pathways of intra- and intermolecular energy dissipation are tracked using the power of the solvent calculated from the QM/MM embedding atomic forces projected on the vibrational modes. The generalized normal mode scheme[68] used in article I is presented below, followed by a description of the energy flux analysis based on the power of the solvent.

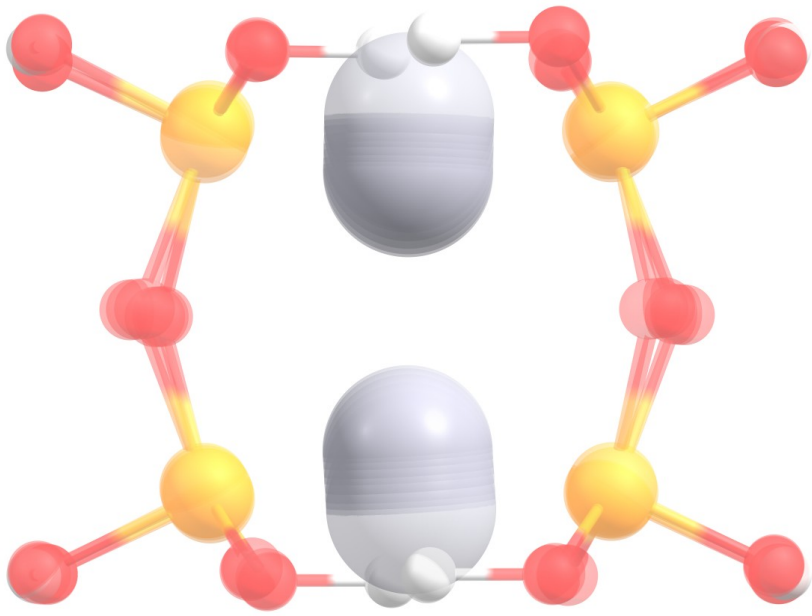

*Figure 5.1. Visualization of the highest energy vibrational mode of PtPOP, obtained using a generalized normal mode analysis. Here, the Pt atoms (grey) are moving symmetrically in a pinching fashion, with simultaneous small distortions of the ligand cage.*

## 5.1 Generalized Normal Modes

A generalized normal mode analysis of a system of atoms is a vibrational analysis at any finite temperature, which generalizes the definition of normal modes as the collection of independent harmonic oscillators obtained as the eigenvectors of the Hessian matrix at low temperature.

Generalized normal modes can be obtained from MD simulations. An approach presented by Strachan [68], [69] is utilized in article I. In this method, the generalized normal modes for a system consisting of $N$ atoms at a finite temperature are defined as the $3N$ modes with velocities $\dot{Q}_i$ that fulfill the following condition:

$$\left\langle \dot{Q}_i(t)\dot{Q}_j(t)\right\rangle \propto \delta_{ij} \qquad i,j = 1,2,\ldots,3N \tag{25}$$

where $\langle \ldots \rangle$ denotes time averaging and $\delta_{ij}$ is the Kronecker delta. These modes are obtained by diagonalizing the covariance matrix of the mass-weighted velocities:

$$K = \frac{1}{2}\left\langle \dot{q}'(t)\dot{q}'^{\dagger}(t)\right\rangle \tag{26}$$

where, $\dot{q}'$ represents a column vector of mass-weighted velocities $\dot{q}'_k = \sqrt{m_k}\dot{q}_k$, for $k = 1,2,\ldots,3N$. These velocities are expressed in a body-fixed reference frame that both translates and rotates with the molecule, derived from MD simulations. The instantaneous velocities of the generalized normal modes are then expressed as:

$$\dot{Q}(t) = L^{\dagger}\dot{q}'(t) \tag{27}$$

where $L$ is the unitary matrix that diagonalizes the covariance matrix $K$. The generalized normal mode velocities $\dot{Q}_i$ satisfy the condition in equation 25, as $\left\langle \dot{Q}(t)\dot{Q}^{\dagger}(t)\right\rangle = 2T$, where $T$ is a diagonal matrix whose elements represent the average kinetic energy of the generalized normal modes. The total instantaneous kinetic energy can be represented as a sum over all generalized normal modes:

$$T(t) = \frac{1}{2}\dot{Q}^{\dagger}(t)\dot{Q}(t) = \frac{1}{2}\sum_{i}^{3N}\dot{Q}_i^2(t) = \sum_{i}^{3N}T_i(t) \tag{28}$$

This formulation allows for a representation of the system's kinetic energy in terms of its generalized normal modes.

## 5.2 Energy Flux Analysis

The time variation of the kinetic energy of a generalized normal mode $i$ (referred to as power, $P_i$) can be expressed as:

$$P_i(t) = \frac{dT_i(t)}{dt} = \dot{Q}_i(t)L_i^{\dagger}\cdot\frac{\mathrm{d}\dot{q}'(t)}{\mathrm{d}t} = \dot{Q}_i(t)L_i^{\dagger}\cdot F'(t) \tag{29}$$

where $L_i$ represents a column vector of the transformation matrix $L$ (see eqs 26 and 27), which corresponds to mode $i$, and $F'(t)$ is a vector of mass-weighted atomic force components $F'_k(t) = F_k(t)/\sqrt{m_k}$, $k = 1,2,\ldots,3N$, as obtained from MD simulations. The change in kinetic

energy of a generalized normal mode $i$ (referred to as work, $W_i$) over a time interval $\tau$ is calculated as:

$$W_i(\tau) \equiv \Delta T_i(\tau) = \int_0^\tau P_i(t)dt = \int_0^\tau \dot{Q}_i(t) L_i^\dagger \cdot F'(t)dt \tag{30}$$

In QM/MM simulations of a solute-solvent system, the instantaneous power of a generalized normal mode of the solute can be decomposed into contributions from each solute atom as follows:

$$P_i(t) = \sum_{\alpha \in \mathrm{QM}} P_i^\alpha(t) = \sum_{\alpha \in \mathrm{QM}} \dot{Q}_i(t) L_i^{\alpha\dagger} \cdot F'_\alpha(t) \tag{31}$$

where, $L_i^{\alpha\dagger}$ contains only the coefficients of the generalized normal mode transformation that correspond to solute atom $\alpha$ and $F'_\alpha(t)$ is the vector representing the mass-weighted instantaneous force acting on solute atom $\alpha$. Consequently, the kinetic energy change for mode $i$ can be broken down into contributions from the work of each solute atom:

$$W_i(\tau) = \sum_{\alpha \in \mathrm{QM}} W_i^\alpha(\tau) = \sum_{\alpha \in \mathrm{QM}} \int_0^\tau \dot{Q}_i(t) L_i^{\alpha\dagger} \cdot F'_\alpha(t)\mathrm{d}t \tag{32}$$

In the QM/MM embedding scheme of a solute-solvent system, the force on a QM atom includes components due to the QM interactions ($F_\alpha^{\mathrm{QM}} = \partial E^{QM}/\partial R_\alpha$), the electrostatic interaction between the solute and solvent ($F_\alpha^{el} = \partial E^{\mathrm{el}}/\partial R_\alpha$, see section 3.1.1), and other short-range interactions between the solute and solvent ($F_\alpha^{\mathrm{sr}} = \partial E^{\mathrm{sr}}/\partial R_\alpha$), here described with an L-J potential (see section 3.1.2), where $R_\alpha$ is the position vector of QM atom $\alpha$. Thus:

$$F_\alpha(t) = F_\alpha^{\mathrm{QM}}(t) + F_\alpha^{\mathrm{el}}(t) + F_\alpha^{\mathrm{sr}}(t) \tag{33}$$

Therefore, the kinetic energy change of a solute vibrational mode can be separated into contributions from the work of QM forces, and the forces exerted by the solvent on the solute atoms, both electrostatic and short-range interactions. This can be expressed as:

$$W_i(\tau) = \sum_{\alpha \in \mathrm{QM}} \left[ W_i^{\alpha,QM}(\tau) + W_i^{\alpha,\mathrm{el}}(\tau) + W_i^{\alpha,\mathrm{sr}}(\tau) \right] = W_i^{\mathrm{QM}}(\tau) + W_i^{\mathrm{el}}(\tau) + W_i^{\mathrm{sr}}(\tau) \tag{34}$$

where:

$$\begin{aligned} W_i^{\mathrm{QM}} &= \sum_{\alpha \in \mathrm{QM}} W_i^{\alpha,\mathrm{QM}} \\ W_i^{\mathrm{el}} &= \sum_{\alpha \in \mathrm{QM}} W_i^{\alpha,\mathrm{el}} \\ W_i^{\mathrm{sr}} &= \sum_{\alpha \in \mathrm{QM}} W_i^{\alpha,\mathrm{sr}} \end{aligned} \tag{35}$$

By neglecting the polarization of the solute due to the solvent electrostatic potential, the first term on the right side of equation 34 represents intramolecular vibrational energy redistribution. The last two terms describe the energy transfer between vibrational mode $i$ of the solute and the solvent, which represents external energy flux.

The approach described here can be applied to nonequilibrium MD simulations where the solute is initially electronically excited. The electronic excitation leads to a simultaneous excitation of vibrational degrees of freedom of the solute. By utilizing the instantaneous QM/MM forces acting on the solute atoms, one can monitor the energy flux between the excited solute vibrational modes and the solvent and analyze the individual atomic contributions.

# 6 Summary of Articles I-III

## 6.1 Decoherence and vibrational energy relaxation of the electronically excited PtPOP complex in solution

Article I investigates the vibrational decoherence and energy relaxation of the photoexcited PtPOP complex in solution, focusing on identifying the pathways of transfer of vibrational energy to the surrounding solvent molecules. Using QM/MM simulations, the study models the ES of the complex and analyzes the mechanisms behind its remarkably long-lived vibrational coherence, in water and acetonitrile.

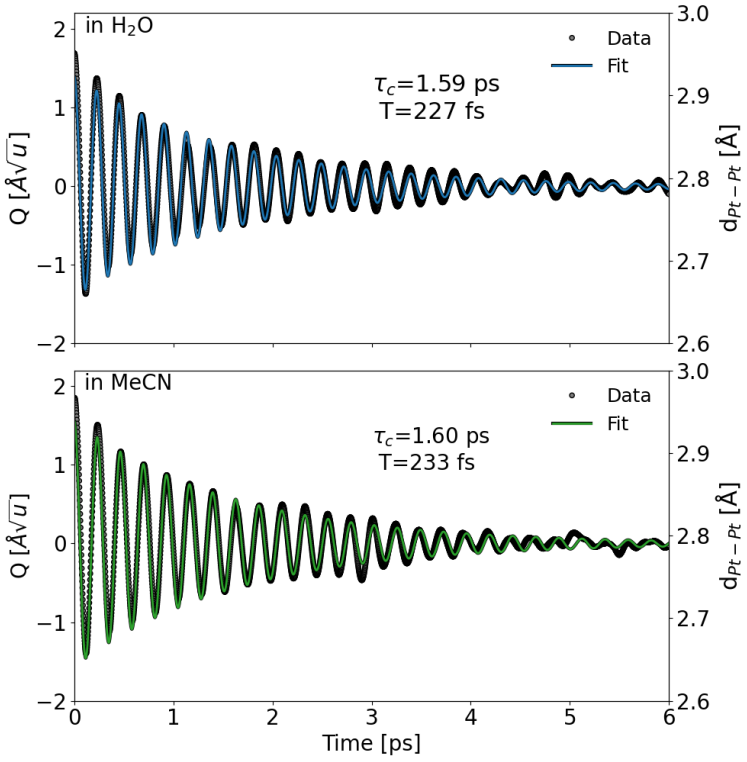


*Figure 6.1. Time evolution of the average pinching mode coordinate obtained from nonequilibrium QM/MM molecular dynamics trajectories of PtPOP excited to the lowest singlet ES in water (top) and acetonitrile (bottom). The oscillation period, $T$, and coherence decay time, $\tau_c$, are obtained from fitting a periodic function with an exponentially decaying amplitude. The decoherence time is in close agreement with the results of ultrafast transient absorption and fluorescence up-conversion experiments of PtPOP in water[70] ($\tau_c$ of 1.76±0.08 and 1.5±0.5 ps, respectively), where intersystem crossing occurs on longer time scale than vibrational relaxation[70] ($\tau_{ISC} > 13$ ps).*

The key finding is that the vibrational decoherence time for the Pt-Pt pinching mode (see Figure 5.1) is approximately 1.6 ps in both solvents, in good agreement with experimental data, see Figure 6.1. After photoexcitation, most of the excess vibrational energy is concentrated in the Pt-Pt bond contraction, but energy dissipation to the solvent directly from the Pt atoms is minimal. The study reveals that energy transfer to the solvent occurs primarily through short-range interactions between ligand atoms and solvent molecules, rather than through direct interactions with the Pt atoms.

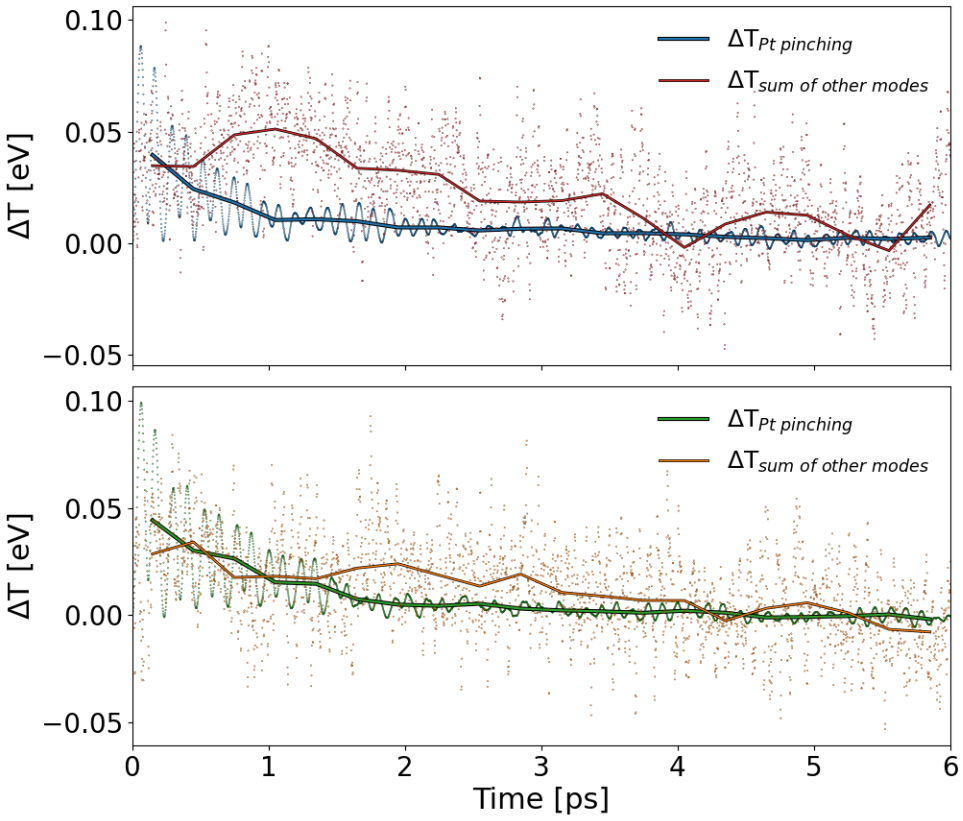


*Figure 6.2. Change in kinetic energy, $T(\tau) - T(0)$, of the pinching mode compared to all other modes after photoexcitation obtained from the generalized normal mode analysis described in section 5.1. The dotted lines represent the instantaneous change in kinetic energy, while the continuous lines represent an average of the instantaneous kinetic energy change over 300 fs time intervals.*

Specifically, the ligand-solvent interactions, involving both repulsive and attractive forces, play a critical role in transferring energy out of the PtPOP complex. In water, although solvent molecules occasionally form transient interactions with the Pt atoms, the net energy transfer from the Pt atoms is minimal. In contrast, most of the energy dissipation occurs through the ligands, as the shielding effect of the ligands around the Pt atoms limits the direct transfer of vibrational energy from the metal centers to the surrounding solvent molecules.

In both systems, short-range ligand-solvent interactions are responsible for transferring most of the vibrational energy to the solvent, with only small contributions from long-range

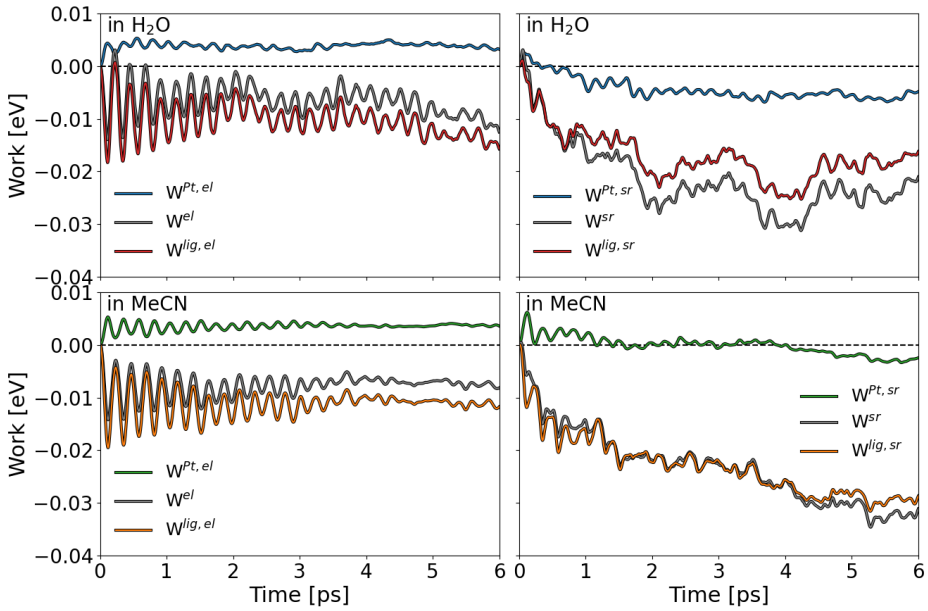


*Figure 6.3. Instantaneous average external work on the pinching mode of PtPOP due to electrostatic (left) and short-range repulsive and attractive L-J (right) interactions with the solvent, and decomposition into contributions of the Pt and ligand atoms, in water (top) and acetonitrile (bottom). In water, a significant fraction of excess vibrational energy is released to the solvent via direct short-range interactions with the Pt atoms. However, a comparable amount of energy is received by the complex through electrostatic Pt-solvent interactions, so there is no net energy transfer via the Pt atoms. In acetonitrile, there is no significant energy transfer to the solvent through direct Pt-solvent interactions.*

electrostatic forces. The lack of strong direct energy transfer from the Pt atoms to the solvent, coupled with the rigidity of the ligand structure, allows the PtPOP complex to maintain its vibrational coherence for an extended period after photoexcitation. This prolonged coherence is largely solvent-independent, with similar energy relaxation dynamics observed in both water and acetonitrile.

In conclusion, the study highlights the inefficient energy transfer directly from the Pt atoms due to their shielding by the ligands, and emphasizes the role of ligand-mediated short-range interactions in the dissipation of vibrational energy to the solvent. These findings are crucial for understanding the mechanisms that govern vibrational energy relaxation in photoexcited complexes and provide insights into the design of molecules with tailored energy dissipation properties for applications in photochemistry and solar energy harvesting.

## 6.2 Characterization of Deformational Isomerization Potential and Interconversion Dynamics with Ultrafast X-ray Solution Scattering

Article II investigates the deformational isomerization and interconversion dynamics of the IrDimen complex in solution. The study focuses on DFT and minimum energy path calculations to characterize the Ir-Ir distances and dihedral twist of the two conformational isomers of the complex, and to explain the role of long-range dispersion interactions in determining their relative stability. The results complement ultrafast X-ray Solution Scattering (XSS) and Optical Transient Absorption Spectroscopy (OTAS) measurements of the structural changes and isomer interconversion dynamics after photoexcitation.

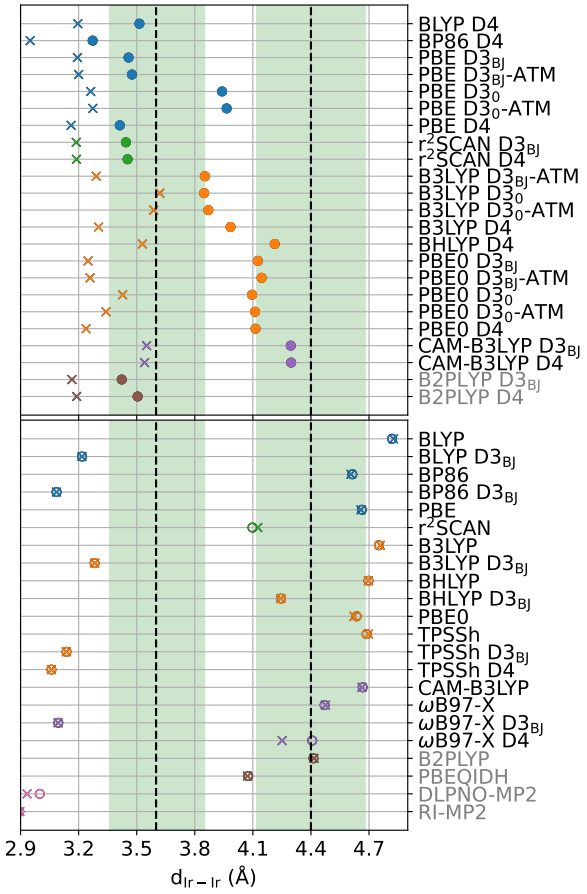


*Figure 6.4. Ir-Ir distances from geometry relaxations started from preliminary long-and-eclipsed (●) and short-and-twisted isomer (×) geometries. The coloring of the markers denotes the functional class; GGA:blue, Meta-GGA:Green, Hybrid:Orange, Range-Separated:Purple, Double-Hybrid:Brown. The black dashed lines at 3.6 Å and 4.4 Å are experimental values obtained for the short and long isomer respectively, the green shade covers the experimental uncertainty. Functionals labeled in grey were too computationally expensive for a vibrational frequency analysis. The upper panel shows results where two isomers were found and the lower panel show results where only one isomer was found.*

The calculations performed in this work assesses several DFT functionals with various types of dispersion corrections with respect to the potential energy surface of the ground state of

the complex and geometry of the long and short isomers. The study highlights the significant influence of long-range dispersion corrections to accurately predict the two distinct isomers of the complex. Different functionals and dispersion correction schemes, such as D3 and D4, are tested. Pure functionals without dispersion corrections fail to predict two isomers, giving instead a single isomer, often with an overestimated Ir-Ir distance.

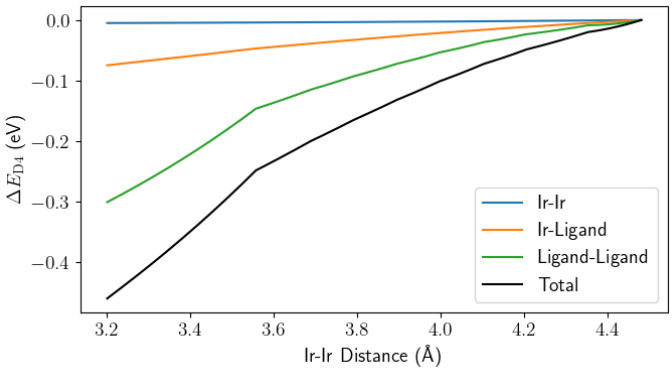


*Figure 6.5. Contributions in terms of interactions between different groups of atoms to the total dispersion interaction energy difference ($\Delta E_{D4}$) along the minimum energy path from the long/eclipsed to the short/twisted isomer of IrDimen. The dispersion interactions are modelled with the D4 correction for PBE0. The total dispersion interaction energy difference is shown in black and a breakdown of the dispersion energy contributions is as follows: Ir-Ir interactions (blue), Ir-ligand interactions (orange) and ligand-ligand interactions (green).*

Hybrid functionals combined with dispersion correction provide better agreement with experimental findings. This indicates that the inclusion of Fock exchange and dispersion interactions play a crucial role in determining the geometry and stability of the isomers. In particular, ligand-ligand interactions dominate the total dispersion energy contribution, followed by metal-ligand interactions, with metal-metal interactions playing a lesser role (see Figure 6.5).

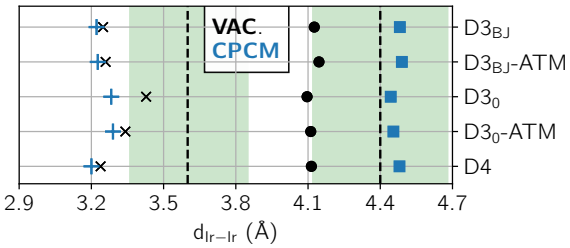


*Figure 6.6. Ir-Ir distances, $d_{Ir-Ir}$, of the optimized geometries of IrDimen obtained by minimizing the energy given by the hybrid functional PBE0 with dispersion corrections in vacuum (black markers) and in acetonitrile as modeled with a polarizable continuum model (CPCM, blue markers), starting from guess structures for the long/eclipsed (● and ■) and short/twisted (× and +) isomers. The black dashed lines and green patches indicate the values deduced from X-ray solution scattering measurements and the corresponding experimental uncertainties, respectively. Including solvent effects in the calculations improves the estimate of Ir-Ir distance for the long/eclipsed conformer.*

Furthermore, the effect of solvent screening is explored using a Conductor-like Polarizable Continuum Model (CPCM) for acetonitrile. The inclusion of solvent effects increases the

Ir-Ir distance for the long isomer, bringing it closer to the experimental values, while having less impact on the short isomer Ir-Ir distance.

Additionally, the study estimates the relative populations of the long and short isomers using harmonic vibrational frequency calculations, as shown in Figure 6.7.

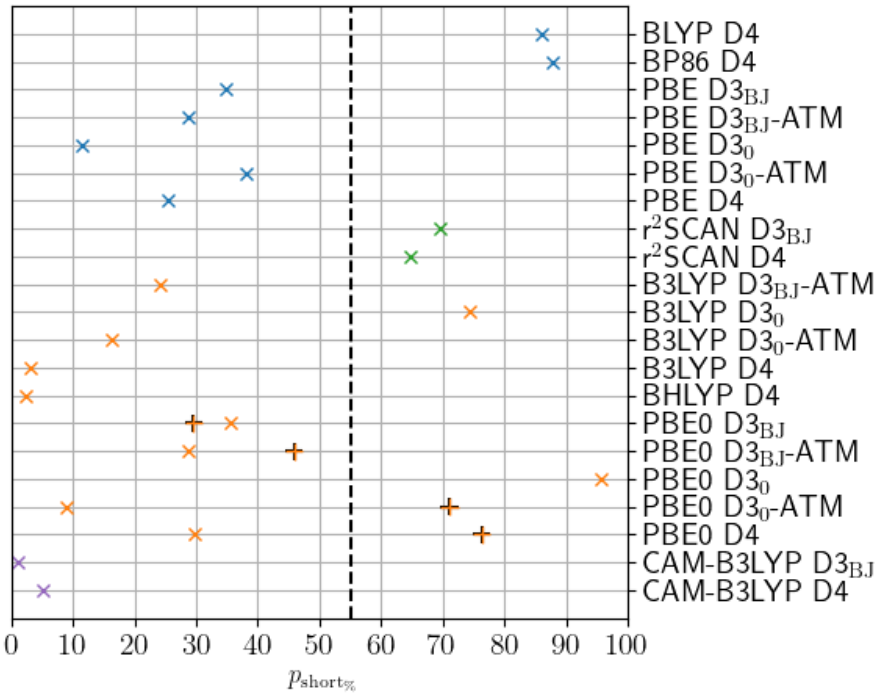


*Figure 6.7. Population analysis of the long and short isomers of IrDimen calculated with different density functional approximations and an analysis of harmonic vibrational frequencies. The "x"-markers represent results of vacuum calculations, while the "+" represent results of calculations including solvent effects described using CPCM. The black dashed line represents the experimentally obtained short conformer population.*

The NEB method is used to map the MEP between the two isomers. A linear relationship between the Ir-Ir contraction and the dihedral twist as the molecule transitions from the long to the short isomer is found. Moreover, the minimum energy path reveals a low-energy and flat barrier, highlighting the anharmonic nature of the potential energy surface. This indicates that the harmonic approximation can only give a qualitative picture of the relative populations of the two isomers, as it does not capture the anharmonic nature of the system. The findings emphasize the importance of anharmonicity in accurately describing the energy landscape of IrDimen and suggest that further refinement of the theoretical model is necessary to improve agreement with experimental observations.

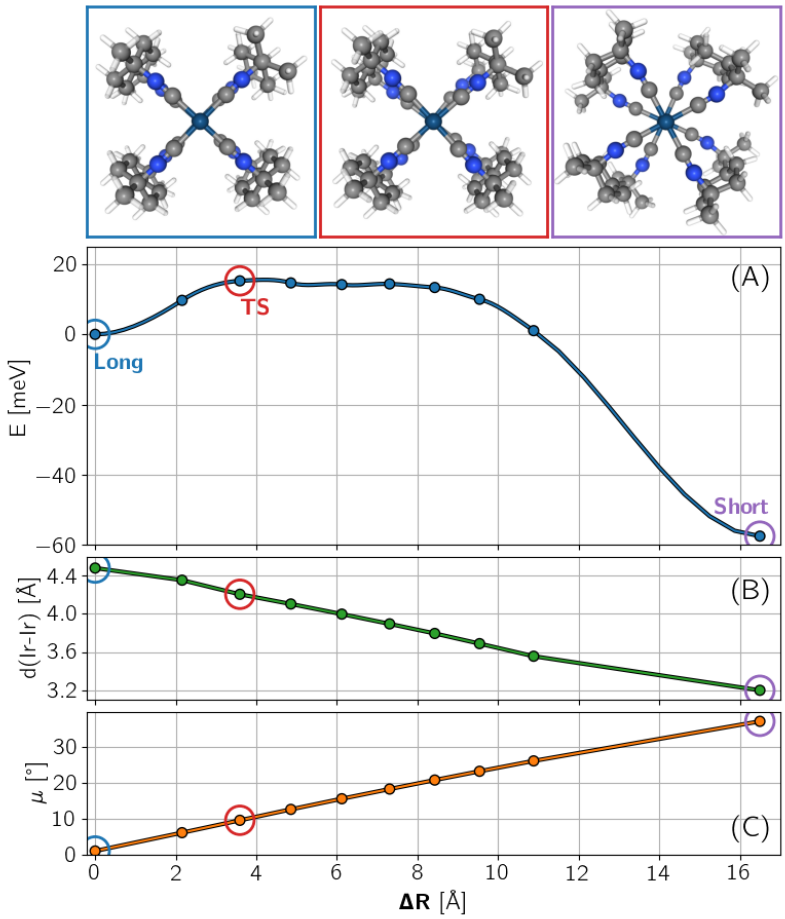


*Figure 6.8. (A) MEP of the deformational isomerism from the long isomer to the short isomer. The filled circles represent the energy change as a function of the reaction coordinate* $\Delta\mathbf{R}$*. The solid line is a piecewise cubic interpolation between images using the tangential atom force and energy. (B) Decrease in Ir-Ir distance along the MEP, correlated with the cumulative displacement of atoms. (C) Increase of the dihedral angle along the MEP, correlated with the cumulative displacement of atoms.*

## 6.3 Localized and Delocalized Charge Distribution in a Diamine Cation: A Challenging Test for Density Functionals

Article III investigates the electronic structure of the DMP cation, focusing on the challenge of accurately modeling the balance between localized and delocalized charge distribution using DFT. This work is originally motivated by measurements of the excitation to a Rydberg electronic state of DMP where it was found that a localized state is first formed where the hole is sitting on one of the N-atoms, but with time the system transforms to a more stable delocalized state where the hole is distributed over both N-atoms. This can be deduced from the binding energy of the Rydberg excited electron. Some theoretical calculations using high level wave function based methods have concluded that also the $DMP^+$ cation can exist in two distinct electronic configurations: a localized state where the positive charge is centered on one nitrogen atom and a delocalized state where the charge is evenly distributed between both nitrogen atoms. The two states then correspond to two different minima on the potential energy surface describing how the energy of the ion varies as a function of the atomic coordinates. This has, however, become quite controversial as other high-level methods have not provided an energy minimum corresponding to the localized state. The delocalized state is generally more stable and lower in energy, making it the default outcome in many computational models. Most density functionals do not predict the presence of a localized state and this can be expected as there is generally a tendency to overly favor delocalized electron distribution in Kohn-Sham DFT functionals. The original hybrid functional, BHLYP, that contains Fock exchange with a weight of 0.5, however, does predict the presence of a localized state. The question addressed here is to what extent various functionals predict the presence of a localized state and even if a minimum is not present, whether the energy surface is smooth enough in that region of configuration space so that the influence of the Rydberg electron, which is expect to be weak, can induce the observed localized state in the Rydberg excited state.

*Table 6.1. Energy difference between delocalized and localized state and the calculated barrier for the DFT functionals where the presence of both states is predicted.*

| XC-Functional | $E_{barr}$ [eV] | $\Delta$ E [eV] | L-D state |
|---|---|---|---|
| PBE0(50 % HF)[a] | 0.0225 | -0.205 | ✓ |
| BHandHLYP | 0.034 | -0.178 | ✓ |
| PBE-PZ-SIC | 0.046 | -0.229 | ✓ |
| B2GPLYP | 0.002 | -0.475 | ✓ |
| MRCI+Q | 0.054 | -0.381 | ✓ |
| Exp. | - | -0.33 | ✓ |

A variety of DFT functionals was tested, including generalized gradient approximations (GGA), hybrid functionals, meta-GGA functionals, range-separated hybrids, and machine-learned functionals. A key problem identified in most functionals is the self-interaction error inherent in Kohn-Sham functionals, which leads to an overemphasis on the delocalization. In order to correct for this, Fock exchange is included in hybrid functionals, but its weight is often adjusted so as to get the optimal performance. Here, it was found that a relatively high fraction of Fock exchange (40% or more) is needed to stabilize a localized state of the cation.

Another approach is to apply an explicit self-interaction correction as proposed by Perdew and Zunger PZ-SIC. This does stabilize the localized state, but it is known from several other studies that this self-interaction correction, which is done orbital-by-orbital and therefore is an independent electron approximation, provides an over correction. For various purposes such as the estimation of bond energy in molecules and band gap in solids, a scaling of the correction by a half gives better results. The study carried out here shows that such scaling eliminates the local minimum on the energy surface corresponding to the localized state.

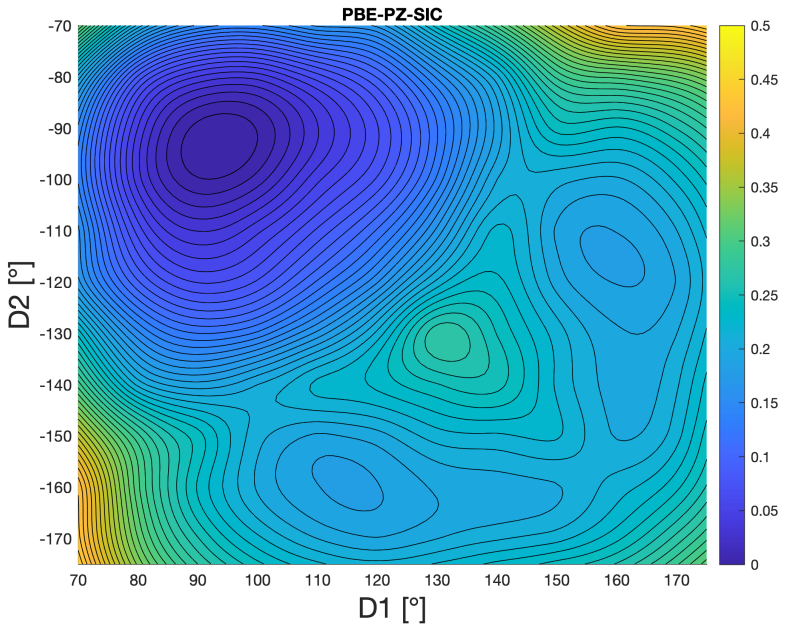


*Figure 6.9. Energy surface of $DMP^+$ with the PBE-SIC functional and the aug-cc-pVDZ basis. Two energy minima are present, a higher one corresponding to a localized state and a lower one corresponding to a delocalized state. A clear energy barrier is present in between the two states.*

The research includes calculations of the energy surface for $DMP^+$, represented by the variation of the energy of the ion as a function of the two dihedral angles of the six-membered ring. The results show that certain functionals, such as BHLYP and PBE0 with Fock exchange scaled up to 50%, predict a metastable localized state and an energy barrier separating it from the delocalized state. The calculations further reveal that the energy barrier between these two minima is relatively small, highlighting the sensitivity of the presence of the localized state to the level of theory used. The semilocal functionals that do not include Fock exchange show no sign of minima corresponding to a localized state, not even an energy valley toward the configurations characterizing the localized state. The recent neural network machine learned functionals, DM21 and DMmc, that are trained to provide piecewise linear dependence of the energy on fractional charges, an important feature for obtaining the right balance between localization and delocalization, also do not predict minima for the localized state but there are clear valleys with gentle slopes in the region of the localized charge density, possibly smooth enough for the influence of a Rydberg excited electron to induce a local minimum. The DM21 an DMmc calculations do not include structural relaxation because atomic forces have not been implemented for these machine learned functionals. Instead, the atomic coordinates are taken from the BHLYP calculations.

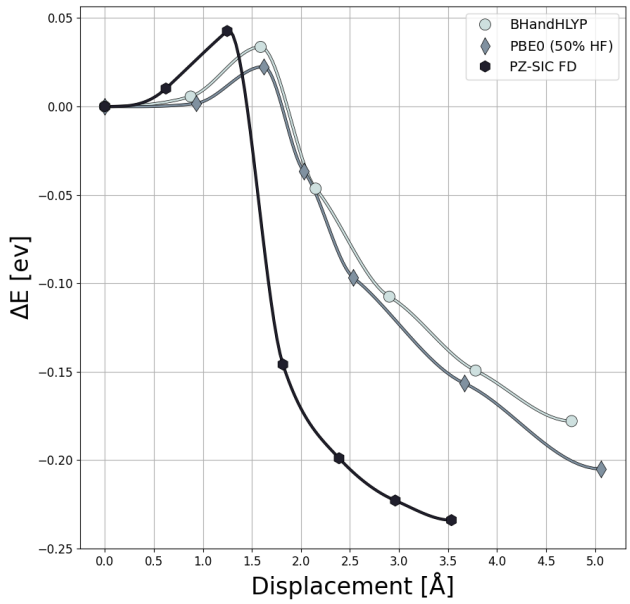


*Figure 6.10. Minimum energy paths for the transition between the localized and delocalized state obtained with three different functionals: PBE0 (with a weight of 0.5 on Fock exchange), PBE-PZ-SIC and BHLYP.*

In conclusion, the $DMP^+$ cation provides a valuable test case for evaluating the performance of density functionals in managing the delicate balance between charge localization and delocalization. Commonly used functionals of GGA and hybrid functional form do not predict a localized state while hybrid functionals with a higher fraction of Fock exchange or full, explicit self-interaction correction do. The scaling of Perdew-Zunger self-interaction correction by 1/2 gives similar results as the PBE0 functional where the weight of Fock exchange is 0.25. This is consistent with previous results showing that calculations of atomization energy of molecules and band gap of solids give better results when the self-interaction correction is scaled by 1/2. The reason for this is that the Perdew-Zunger self-interaction correction is an orbital-by-orbital correction, and therefore represents an independent electron approximation. When orbital densities overlap, the many body nature of the wave function calls for reduced correction, analogous to the scaled Fock exchange in hybrid functionals.

# References


[1] A. Becke, "A review of density functional theory," *The Journal of Chemical Physics*, vol. 140, no. 18, 18A301, 2014.

[2] W. Kohn and L. J. Sham, "Self-consistent equations including exchange and correlation effects," *Phys. Rev.*, vol. 140, A1133–A1138, 4A Nov. 1965. DOI: 10.1103/PhysRev.140.A1133. [Online]. Available: https://link.aps.org/doi/10.1103/PhysRev.140.A1133.

[3] S. Gusarov, "Advances in computational methods for modeling photocatalytic reactions: A review of recent developments," *Materials*, vol. 17, no. 9, 2024, ISSN: 1996-1944. DOI: 10.3390/ma17092119. [Online]. Available: https://www.mdpi.com/1996-1944/17/9/2119.

[4] J. Cuéllar-Zuquin, J. Carmona-García, M. Navarrete-Miguel, *et al.*, "Quantum chemistry of the excited state: advances in 2020–2021," in *Photochemistry: Volume 50*, The Royal Society of Chemistry, Dec. 2022, ISBN: 978-1-83916-567-2. DOI: 10.1039/9781839167676-00028. [Online]. Available: https://doi.org/10.1039/9781839167676-00028.

[5] D. Marx and J. Hutter, "Ab initio molecular dynamics: Theory and implementation," in *Modern Methods and Algorithms of Quantum Chemistry*, vol. 2, John von Neumann Institute for Computing, 2009, pp. 301–449. DOI: 10.3204/PUBDB-201268.

[6] S. Grimme, "Semiempirical hybrid density functional with perturbative corrections for london dispersion," *Journal of Computational Chemistry*, vol. 31, no. 4, pp. 878–893, 2010. DOI: 10.1002/jcc.21367.

[7] G. Levi, A. V. Ivanov, and H. Jónsson, "Variational density functional calculations of excited states via direct optimization," *Journal of Chemical Theory and Computation*, vol. 16, no. 11, pp. 6968–6982, Oct. 2020, ISSN: 1549-9626. DOI: 10.1021/acs.jctc.0c00597. [Online]. Available: http://dx.doi.org/10.1021/acs.jctc.0c00597.

[8] G. Levi, A. V. Ivanov, and H. Jónsson, "Variational calculations of excited states via direct optimization of the orbitals in dft," *Faraday Discuss.*, vol. 224, pp. 448–466, 0 2020. DOI: 10.1039/D0FD00064G. [Online]. Available: http://dx.doi.org/10.1039/D0FD00064G.

[9] A. V. Ivanov, G. Levi, E. Ö. Jónsson, and H. Jónsson, "Method for calculating excited electronic states using density functionals and direct orbital optimization with real space grid or plane-wave basis set," *Journal of Chemical Theory and Computation*, vol. 17, no. 8, pp. 5034–5049, Jul. 2021, ISSN: 1549-9626. DOI: 10.1021/acs.jctc.1c00157. [Online]. Available: http://dx.doi.org/10.1021/acs.jctc.1c00157.

[10] A. V. Ivanov, E. Ö. Jónsson, T. Vegge, and H. Jónsson, "Direct energy minimization based on exponential transformation in density functional calculations of finite and extended systems," *Computer Physics Communications*, vol. 267, p. 108 047, Oct. 2021,

ISSN: 0010-4655. DOI: 10.1016/j.cpc.2021.108047. [Online]. Available: http://dx.doi.org/10.1016/j.cpc.2021.108047.

[11] A. T. B. Gilbert, N. A. Besley, and P. M. W. Gill, "Self-consistent field calculations of excited states using the maximum overlap method (mom)," *The Journal of Physical Chemistry A*, vol. 112, no. 50, pp. 13 164–13 171, 2008. DOI: 10.1021/jp801738f.

[12] P. Hohenberg and W. Kohn, "Inhomogeneous electron gas," *Phys. Rev.*, vol. 136, B864–B871, 3B Nov. 1964. DOI: 10.1103/PhysRev.136.B864. [Online]. Available: https://link.aps.org/doi/10.1103/PhysRev.136.B864.

[13] J. P. Perdew, K. Burke, and M. Ernzerhof, "Generalized gradient approximation made simple," *Physical Review Letters*, vol. 77, no. 18, pp. 3865–3868, 1996. DOI: 10.1103/PhysRevLett.77.3865.

[14] W. Kohn, "Nobel lecture: Electronic structure of matter—wave functions and density functionals," *Reviews of Modern Physics*, vol. 71, no. 5, pp. 1253–1266, 1999. DOI: 10.1103/RevModPhys.71.1253.

[15] A. Tkatchenko and M. Scheffler, "Accurate molecular van der waals interactions from density functional theory," *Physical Review Letters*, vol. 102, no. 7, p. 073 005, 2009.

[16] S. Grimme, "Density functional theory with london dispersion corrections," *Wiley Interdisciplinary Reviews: Computational Molecular Science*, vol. 1, no. 2, pp. 211–228, 2011. DOI: 10.1002/wcms.30.

[17] E. Caldeweyher, S. Ehlert, A. Hansen, *et al.*, "D4 dispersion correction for density functional theory," *Journal of Chemical Physics*, vol. 150, p. 154 122, 2019.

[18] S. Grimme, J. Antony, S. Ehrlich, and H. Krieg, "A consistent and accurate ab initio parametrization of density functional dispersion correction (dft-d)," *Journal of Chemical Physics*, vol. 132, no. 15, p. 154 104, 2010. DOI: 10.1063/1.3382344.

[19] J. P. Perdew and A. Zunger, "Self-interaction correction to density-functional approximations for many-electron systems," *Physical Review B*, vol. 23, no. 10, pp. 5048–5079, 1981. DOI: 10.1103/PhysRevB.23.5048.

[20] P. Mori-Sánchez, A. J. Cohen, and W. Yang, "Many-electron self-interaction error in approximate density functionals," *The Journal of Chemical Physics*, vol. 125, no. 20, p. 201 102, Nov. 2006, ISSN: 0021-9606. DOI: 10.1063/1.2403848. eprint: https://pubs.aip.org/aip/jcp/article-pdf/doi/10.1063/1.2403848/15391294/201102_1_online.pdf. [Online]. Available: https://doi.org/10.1063/1.2403848.

[21] H. Jónsson, "Simulation of surface processes," *Proceedings of the National Academy of Sciences*, vol. 108, p. 944, 2011.

[22] Y. Zhang, P. M. Weber, and H. Jónsson, "Self-interaction corrected functional calculations of a dipole-bound molecular anion," *The Journal of Physical Chemistry Letters*, vol. 7, no. 11, pp. 2068–2073, Jun. 2016. DOI: 10.1021/acs.jpclett.6b00742. [Online]. Available: https://doi.org/10.1021/acs.jpclett.6b00742.

[23] A. E. Sigurdarson, Y. L. A. Schmerwitz, D. K. V. Tveiten, G. Levi, and H. Jónsson, "Orbital-optimized density functional calculations of molecular Rydberg excited states with real space grid representation and self-interaction correction," *The Journal of Chemical Physics*, vol. 159, no. 21, p. 214 109, Dec. 2023, ISSN: 0021-9606. DOI: 10.1063/5.0179271. eprint: https://pubs.aip.org/aip/jcp/article-pdf/doi/10.1063/5.0179271/18236027/214109_1_5.0179271.pdf. [Online]. Available: https://doi.org/10.1063/5.0179271.

[24] O. A. Vydrov, G. E. Scuseria, J. P. Perdew, A. Ruzsinszky, and G. I. Csonka, "Scaling down the Perdew-Zunger self-interaction correction in many-electron regions," *The Journal of Chemical Physics*, vol. 124, no. 9, p. 094 108, Mar. 2006, ISSN: 0021-9606. DOI: 10.1063/1.2176608. eprint: https://pubs.aip.org/aip/jcp/article-pdf/doi/10.1063/1.2176608/15379512/094108_1_online.pdf. [Online]. Available: https://doi.org/10.1063/1.2176608.

[25] S. Klüpfel, P. Klüpfel, and H. Jónsson, "The effect of the perdew-zunger self-interaction correction to density functionals on the energetics of small molecules," *J. Chem. Phys.*, vol. 137, p. 124 102, 2012.

[26] H. Lischka, D. Nachtigallová, A. J. Aquino, *et al.*, "Multireference Approaches for Excited States of Molecules," *Chemical Reviews*, vol. 118, no. 15, pp. 7293–7361, 2018, ISSN: 15206890. DOI: 10.1021/acs.chemrev.8b00244.

[27] M. E. Casida, "Time-dependent density functional response theory for molecules," *Recent Advances in Computational Chemistry*, vol. 1, pp. 155–192, 1995. DOI: 10.1142/9789812830586_0005.

[28] E. Runge and E. K. U. Gross, "Density-functional theory for time-dependent systems," *Physical Review Letters*, vol. 52, no. 12, pp. 997–1000, 1984, ISSN: 00319007. DOI: 10.1103/PhysRevLett.52.997.

[29] E. Selenius, A. E. Sigurðarson, Y. L. A. Schmerwitz, and G. Levi, "Orbital-Optimized Versus Time-Dependent Density Functional Calculations of Intramolecular Charge Transfer Excited States," *Journal of Chemical Theory and Computation*, vol. 20, pp. 3809–3822, 2024. DOI: 10.1021/acs.jctc.3c01319. arXiv: 2311.01604. [Online]. Available: https://doi.org/10.1021/acs.jctc.3c01319.

[30] A. Dreuw and M. Head-Gordon, "Failure of Time-Dependent Density Functional Theory for Long-Range Charge-Transfer Excited States: The Zincbacteriochlorin-Bacteriochlorin and Bacteriochlorophyll-Spheroidene Complexes," *Journal of the American Chemical Society*, vol. 126, no. 12, pp. 4007–4016, 2004, ISSN: 00027863. DOI: 10.1021/ja039556n. arXiv: 1101.3379.

[31] T. Stein, L. Kronik, and R. Baer, "Reliable prediction of charge transfer excitations in molecular complexes using time-dependent density functional theory," *Journal of the American Chemical Society*, vol. 131, no. 8, pp. 2818–2820, Mar. 2009, ISSN: 00027863. DOI: 10.1021/ja8087482. [Online]. Available: https://pubs.acs.org/sharingguidelines.

[32] A. Dreuw, J. L. Weisman, and M. Head-Gordon, "Long-range charge-transfer excited states in time-dependent density functional theory require non-local exchange," *Journal of Chemical Physics*, vol. 119, no. 6, pp. 2943–2946, 2003, ISSN: 00219606. DOI: 10.1063/1.1590951.

[33] P. W. Ayers, M. Levy, and A. Nagy, "Time-independent density-functional theory for excited states of Coulomb systems," *Physical Review A*, vol. 85, no. 4, p. 042 518, Apr. 2012, ISSN: 1050-2947. DOI: 10.1103/PhysRevA.85.042518. [Online]. Available: https://link.aps.org/doi/10.1103/PhysRevA.85.042518.

[34] M. Levy and Á. Nagy, "Variational density-functional theory for an individual excited state," *Physical Review Letters*, vol. 83, no. 21, pp. 4361–4364, 1999, ISSN: 10797114. DOI: 10.1103/PhysRevLett.83.4361.

[35] A. Görling, "Density-functional theory beyond the Hohenberg-Kohn theorem," *Physical Review A - Atomic, Molecular, and Optical Physics*, vol. 59, no. 5, pp. 3359–3374, 1999, ISSN: 10941622. DOI: 10.1103/PhysRevA.59.3359.

[36] D. Hait and M. Head-Gordon, "Orbital Optimized Density Functional Theory for Electronic Excited States," *Journal of Physical Chemistry Letters*, vol. 12, no. 19, pp. 4517–4529, May 2021, ISSN: 19487185. DOI: 10.1021/acs.jpclett.1c00744. arXiv: 2103.04573. [Online]. Available: https://pubs.acs.org/doi/10.1021/acs.jpclett.1c00744.

[37] A. E. Sigurdarson, Y. L. A. Schmerwitz, D. K. V. Tveiten, G. Levi, and H. Jónsson, "Orbital-optimized Density Functional Calculations of Molecular Rydberg Excited States with Real Space Grid Representation and Self-Interaction Correction," *Journal of Chemical Physics*, vol. 159, p. 214 109, 2023. DOI: 10.1063/5.0179271. arXiv: 2310.17605. [Online]. Available: https://doi.org/10.1063/5.0179271.

[38] C. L. Cheng, Q. Wu, and T. Van Voorhis, "Rydberg energies using excited state density functional theory," *Journal of Chemical Physics*, vol. 129, no. 12, p. 124 112, 2008, ISSN: 00219606. DOI: 10.1063/1.2977989.

[39] N. Bogo and C. J. Stein, "Benchmarking DFT-based excited-state methods for intermolecular charge-transfer excitations," *Physical Chemistry Chemical Physics*, 2024. arXiv: 2405.01382. [Online]. Available: http://arxiv.org/abs/2405.01382.

[40] E. Vandaele, M. Mališ, and S. Luber, "The ΔSCF method for non-adiabatic dynamics of systems in the liquid phase," *J. Chem. Phys*, vol. 156, p. 130 901, 2022. DOI: 10.1063/5.0083340. [Online]. Available: https://doi.org/10.1063/5.0083340.

[41] G. Levi, E. Biasin, A. O. Dohn, and H. Jónsson, "On the interplay of solvent and conformational effects in simulated excited-state dynamics of a copper phenanthroline photosensitizer," *Physical Chemistry Chemical Physics*, vol. 22, pp. 748–757, 2020, ISSN: 1463-9076. DOI: 10.1039/C9CP06086C. [Online]. Available: http://dx.doi.org/10.1039/C9CP06086C.

[42] G. Levi, M. Papai, N. E. Henriksen, A. O. Dohn, and K. B. Møller, "Solution structure and ultrafast vibrational relaxation of the PtPOP complex revealed by SCF-QM/MM Direct Dynamics simulations," *Journal of Physical Chemistry C*, vol. 122, pp. 7100–7119, 2018, ISSN: 1932-7447. DOI: 10.1021/acs.jpcc.8b00301. [Online]. Available: https://pubs.acs.org/doi/10.1021/acs.jpcc.8b00301.

[43] Y. L. A. Schmerwitz, G. Levi, and H. Jónsson, "Calculations of excited electronic states by converging on saddle points using generalized mode following," *Journal of Chemical Theory and Computation*, vol. 19, no. 12, pp. 3634–3651, Jun. 2023. DOI: 10.1021/acs.jctc.3c00178. [Online]. Available: https://doi.org/10.1021/acs.jctc.3c00178.

[44] D. Hait and M. Head-Gordon, "Excited state orbital optimization via minimizing the square of the gradient: General approach and application to singly and doubly excited states via density functional theory," *Journal of Chemical Theory and Computation*, vol. 16, pp. 1699–1710, 2020. DOI: 10.1021/acs.jctc.9b01127. arXiv: 1911.04709. [Online]. Available: http://arxiv.org/abs/1911.04709.

[45] G. M. J. Barca, A. T. B. Gilbert, and P. M. W. Gill, "Simple models for difficult electronic excitations," *Journal of Chemical Theory and Computation*, vol. 14, no. 3,

pp. 1501–1509, Mar. 2018. DOI: 10.1021/acs.jctc.7b00994. [Online]. Available: https://doi.org/10.1021/acs.jctc.7b00994.

[46] A. V. Ivanov, E. Jónsson, T. Vegge, and H. Jónsson, "Direct energy minimization based on exponential transformation in density functional calculations of finite and extended systems," *Computer Physics Communications*, vol. 267, p. 108 047, Oct. 2021, ISSN: 00104655. DOI: 10.1016/j.cpc.2021.108047. arXiv: 2101.12597.

[47] M. Head-Gordon and J. A. Pople, "Optimization of wave function and geometry in the finite basis Hartree-Fock method," *Journal of Physical Chemistry*, vol. 92, no. 11, pp. 3063–3069, 1988, ISSN: 00223654. DOI: 10.1021/j100322a012.

[48] J. J. Mortensen, A. H. Larsen, M. Kuisma, *et al.*, "GPAW: An open Python package for electronic structure calculations," *The Journal of Chemical Physics*, vol. 160, no. 9, p. 092 503, Mar. 2024, ISSN: 0021-9606. DOI: 10.1063/5.0182685. eprint: https://pubs.aip.org/aip/jcp/article-pdf/doi/10.1063/5.0182685/19717263/092503_1_5.0182685.pdf. [Online]. Available: https://doi.org/10.1063/5.0182685.

[49] A. Warshel and M. Levitt, "Theoretical studies of enzymic reactions: Dielectric, electrostatic and steric stabilization of the carbonium ion in the reaction of lysozyme," *Journal of Molecular Biology*, vol. 103, no. 2, pp. 227–249, 1976. DOI: 10.1016/0022-2836(76)90311-9.

[50] M. J. Field, P. A. Bash, and M. Karplus, "A combined quantum mechanical and molecular mechanical potential for molecular dynamics simulations," *Journal of Computational Chemistry*, vol. 11, no. 6, pp. 700–733, 1990. DOI: https://doi.org/10.1002/jcc.540110605. eprint: https://onlinelibrary.wiley.com/doi/pdf/10.1002/jcc.540110605. [Online]. Available: https://onlinelibrary.wiley.com/doi/abs/10.1002/jcc.540110605.

[51] J. E. Jones, "On the determination of molecular fields," *Proceedings of the Royal Society A: Mathematical, Physical and Engineering Sciences*, vol. 106, no. 738, pp. 463–477, 1924. DOI: 10.1098/rspa.1924.0081.

[52] H. M. Senn and W. Thiel, "Hybrid quantum and molecular mechanical simulations of enzyme reactions," *Angewandte Chemie International Edition*, vol. 48, no. 7, pp. 1198–1229, 2009.

[53] A. O. Dohn, "Multiscale electrostatic embedding simulations for modeling structure and dynamics of molecules in solution: A tutorial review," *International Journal of Quantum Chemistry*, vol. 120, no. 21, p. 26 343, Nov. 2020, ISSN: 0020-7608. DOI: 10.1002/qua.26343. [Online]. Available: https://onlinelibrary.wiley.com/doi/10.1002/qua.26343.

[54] A. O. Dohn, E. Ö. Jónsson, G. Levi, *et al.*, "Grid-Based Projector Augmented Wave (GPAW) Implementation of Quantum Mechanics/Molecular Mechanics (QM/MM) Electrostatic Embedding and Application to a Solvated Diplatinum Complex," *J. Chem. Theory Comput.*, vol. 13, no. 12, pp. 6010–6022, 2017. DOI: 10.1021/acs.jctc.7b00621.

[55] H. Lin and D. G. Truhlar, "Qm/mm: What have we learned, where are we, and where do we go from here?" *Theoretical Chemistry Accounts*, vol. 117, no. 2, pp. 185–199, 2007. DOI: 10.1007/s00214-006-0143-z. [Online]. Available: https://doi.org/10.1007/s00214-006-0143-z.

[56] R. A. Friesner, "Combined quantum and molecular mechanics (qm/mm)," *Drug Discovery Today: Technologies*, vol. 1, no. 3, pp. 253–260, 2004, ISSN: 1740-6749. DOI:

https://doi.org/10.1016/j.ddtec.2004.11.008. [Online]. Available: https://www.sciencedirect.com/science/article/pii/S1740674904000563.

[57] A. O. Dohn, E. Ö. Jónsson, and H. Jónsson, "Polarizable Embedding with a Transferable H2O Potential Function II: Application to (H2O)n Clusters and Liquid Water," *Journal of Chemical Theory and Computation*, vol. 15, no. 12, pp. 6578–6587, Dec. 2019, ISSN: 15499626. DOI: 10.1021/acs.jctc.9b00778. [Online]. Available: https://pubs.acs.org/sharingguidelines.

[58] E. Ö. Jónsson, A. O. Dohn, and H. Jónsson, "Polarizable Embedding with a Transferable H2O Potential Function I: Formulation and Tests on Dimer," *Journal of Chemical Theory and Computation*, vol. 15, no. 12, pp. 6562–6577, Dec. 2019, ISSN: 15499626. DOI: 10.1021/acs.jctc.9b00777. [Online]. Available: https://pubs.acs.org/sharingguidelines.

[59] P. Langevin, "On the theory of brownian motion," *Comptes Rendus*, vol. 146, pp. 530–533, 1908.

[60] H. J. C. Berendsen, J. P. M. Postma, W. F. van Gunsteren, A. DiNola, and J. R. Haak, "Molecular dynamics with coupling to an external bath," *The Journal of Chemical Physics*, vol. 81, no. 8, pp. 3684–3690, Oct. 1984, ISSN: 0021-9606. DOI: 10.1063/1.448118. eprint: https://pubs.aip.org/aip/jcp/article-pdf/81/8/3684/18950084/3684_1_online.pdf. [Online]. Available: https://doi.org/10.1063/1.448118.

[61] G. Henkelman and H. Jónsson, "Improved tangent estimate in the nudged elastic band method for finding minimum energy paths and saddle points," *Journal of Chemical Physics*, vol. 113, no. 22, pp. 9978–9985, 2000.

[62] H. Jónsson, G. Mills, and K. W. Jacobsen, "The nudged elastic band method: Theory and applications," *Classical and Quantum Dynamics in Condensed Phase Simulations*, pp. 385–404, 1998.

[63] V. Ásgeirsson, B. O. Birgisson, R. Bjornsson, *et al.*, "Nudged elastic band method for molecular reactions using energy-weighted springs combined with eigenvector following," *Journal of Chemical Theory and Computation*, vol. 17, no. 8, pp. 4929–4945, Aug. 2021. DOI: 10.1021/acs.jctc.1c00462. [Online]. Available: https://doi.org/10.1021/acs.jctc.1c00462.

[64] G. Henkelman, B. P. Uberuaga, and H. Jónsson, "A climbing image nudged elastic band method for finding saddle points and minimum energy paths," *Journal of Chemical Physics*, vol. 113, no. 22, pp. 9901–9904, 2000.

[65] H. Eyring, "The Activated Complex in Chemical Reactions," *The Journal of Chemical Physics*, vol. 3, no. 2, pp. 107–115, Feb. 1935, ISSN: 0021-9606. DOI: 10.1063/1.1749604. eprint: https://pubs.aip.org/aip/jcp/article-pdf/3/2/107/18788362/107_1_online.pdf. [Online]. Available: https://doi.org/10.1063/1.1749604.

[66] D. G. Truhlar, B. C. Garrett, and S. J. Klippenstein, "Current status of transition-state theory," *Journal of Physical Chemistry*, vol. 100, no. 31, pp. 12 771–12 800, 1996.

[67] J. L. Bao and D. G. Truhlar, "Variational transition state theory: Theoretical framework and recent developments," *Chem. Soc. Rev.*, vol. 46, pp. 7548–7596, 24 2017. DOI: 10.1039/C7CS00602K. [Online]. Available: http://dx.doi.org/10.1039/C7CS00602K.

[68] A. Strachan, "Normal modes and frequencies from covariances in molecular dynamics or monte carlo simulations," *Journal of Chemical Physics*, vol. 120, no. 1, pp. 1–4, 2004, ISSN: 00219606. DOI: 10.1063/1.1635364.

[69] N. Rega, "Vibrational analysis beyond the harmonic regime from Ab-initio molecular dynamics," *Theoretical Chemistry Accounts*, vol. 116, pp. 347–354, 2006, ISSN: 1432881X. DOI: 10.1007/s00214-006-0076-6.

[70] R. M. Van Der Veen, A. Cannizzo, F. V. Mourik, A. Vlček, and M. Chergui, "Vibrational Relaxation and Intersystem Crossing of Binuclear Metal Complexes in Solution," *J. Am. Chem. Soc.*, vol. 133, no. 12, pp. 305–315, 2011.

# Appendix A: Publications included in this thesis

# Paper I

**Decoherence and vibrational energy relaxation of the electronically excited PtPOP complex in solution**

Benedikt O. Birgisson, Asmus Ougaard Dohn, Hannes Jónsson, and Gianluca Levi

*Accepted for publication in Journal of Chemical Physics*

# Decoherence and vibrational energy relaxation of the electronically excited PtPOP complex in solution

Benedikt O. Birgisson,[1] Asmus Ougaard Dohn,[2] Hannes Jónsson,[1,3] and Gianluca Levi[1]

[1)] *Science Institute and Faculty of Physical Sciences, University of Iceland, Reykjavík, Iceland*

[2)] *Department of Physics, Technical University of Denmark, 2800 Lyngby, Denmark*

[3)] *Deptartment of Chemistry, Brown University, Providence, Rhode Island 02912, USA*

(*Electronic mail: giale@hi.is)

Understanding the ultrafast vibrational relaxation following photoexcitation of molecules in a condensed phase is essential to predict the outcome and improve the efficiency of photoinduced molecular processes. Here, the vibrational decoherence and energy relaxation of a binuclear complex, $[Pt_2(P_2O_5H_2)_4]^{4-}$ (PtPOP), upon electronic excitation in liquid water and acetonitrile are investigated through direct adiabatic dynamics simulations. A quantum mechanics/molecular mechanics (QM/MM) scheme is used where the excited state of the complex is modelled with orbital-optimized density functional calculations while solvent molecules are described using potential energy functions. The decoherence time of the Pt-Pt vibration dominating the photoinduced dynamics is found to be $\sim$1.6 ps in both solvents. This is in excellent agreement with experimental measurements in water, where intersystem crossing is slow ($>$ 10 ps). Pathways for the flow of excess energy are identified by monitoring the power of the solvent on vibrational modes. The latter are obtained as generalized normal modes from the velocity covariances, and the power is computed using QM/MM embedding forces. Excess vibrational energy is found to be predominantly released through short-range repulsive and attractive interactions between the ligand atoms and surrounding solvent molecules, whereas solute-solvent interactions involving the Pt atoms are less important. Since photoexcitation deposits most of the excess energy into Pt-Pt vibrations, energy dissipation to the solvent is inefficient. This study reveals the mechanism behind the exceptionally long vibrational coherence of the photoexcited PtPOP complex in solution and underscores the importance of short-range interactions for accurate simulations of vibrational energy relaxation of solvated molecules.

# I. INTRODUCTION

The world's growing demand for economically viable and sustainable energy solutions has led to an increased interest in exploiting photoactive molecules for solar harvesting applications. When a molecule absorbs light, its vibrational degrees of freedom can be excited as a result of changes in the molecular potential energy surface upon electronic excitation. For a short pulse of light, a coherent superposition of vibrational states can be formed and coherent vibrations of the atoms can be observed following photoexcitation[1]. In a condensed phase, such as a solution, the coherent oscillations are suppressed by elastic and inelastic collisions with the environment, resulting in energy relaxation and randomization of the phase along the initially excited vibrational degrees of freedom. This process typically occurs on a time scale ranging from a few femtoseconds to a few picoseconds. Such transient photoinduced coherent vibrations in molecules are increasingly being detected in ultrafast pump-probe experiments, providing insights into the underlying potential energy surfaces of excited electronic states and the interactions with the environment[2]. The role of coherent vibrations in energy conversion processes is also becoming more evident. For example, recent studies suggest that vibrational and electronic-vibrational (vibronic) coherences may enhance charge and energy transfer in photosynthetic systems[3–6]. Despite their importance and ubiquity in time-resolved studies, the mechanisms of decoherence and vibrational energy relaxation often remain unknown. Indeed, it is typically challenging, if possible at all, to disentangle pure dephasing effects and the pathways of intramolecular energy redistribution and dissipation to the environment from the observables of ultrafast experiments.

Bimetallic $d^8$-$d^8$ complexes, particularly Pt(II)-Pt(II) complexes, represent a class of photoactive molecules where electronic excitation induces long-lasting coherent atomic vibrations[7–9]. In Pt(II)-Pt(II) compounds, the lowest lying triplet and singlet excited states involve excitation from a metal-metal $d\sigma^*$ antibonding HOMO to a metal-metal $p\sigma$ bonding or ligand-centered LUMO, depending on the ligands. Depopulation of a metal-metal antibonding orbital upon photoexcitation leads to a shortening of the Pt-Pt bond, thereby launching coherent vibrations along the Pt-Pt coordinate[10–16]. The decay of these coherent oscillations and the timescale of intersystem crossing from the lowest singlet to the lowest triplet excited state in solution depend on the ligands. Larger and more flexible ligands typically promote dephasing, thereby shortening the coherence time[12].

$[Pt_2(P_2O_5H_2)_4]^{4-}$ (PtPOP) is the quintessential prototype of Pt(II)-Pt(II) compound, having been extensively studied both experimentally[14–26] and theoretically[27–34]. Below 320 nm, the optical absorption spectrum of PtPOP in solution exhibits a single intense band around 370 nm due to an electric dipole-allowed transition to the lowest singlet excited state[9,18,29]. Between 200 and 320 nm, only weakly-allowed UV transitions are observed[9,18,29]. Thus, ultrafast experiments on PtPOP typically involve direct excitation to the lowest singlet excited state. Such excitation corresponds to a $p\sigma \leftarrow d\sigma^*$ transition, resulting in a 0.24–0.31 Å shortening of the Pt-Pt bond in solution[14,17,19,20]. This bond contraction is accompanied by remarkably long-lived coherent Pt-Pt oscillations, as observed in both the ground and excited states through ultrafast optical spectroscopy[15,16,18] and X-ray scattering experiments[14]. The decoherence time is found to be in the range of 1.5-2.5 ps[14–16], for a wide range of solvents. In contrast, intersystem crossing to the lowest triplet excited state is significantly affected by the solvent, being as fast as 700-900 fs[15] in acetonitrile and as slow as 14-15 ps in water and 26-29 ps in ethanol[16]. The faster transition to the lowest triplet state in acetonitrile has been shown to be driven by spin-vibronic coupling between the singlet excited state and an intermediate triplet state with charge transfer character, which is stabilized by this polar solvent[15,27]. Significantly, since decoherence is slower than intersystem crossing in acetonitrile, the vibrational coherence is preserved during the electronic transition, leading to the observation of coherent vibrations in the lowest triplet excited state[15,27].

Previous quantum mechanics/molecular mechanics (QM/MM) molecular dynamics simulations with explicit description of the solvent have provided some insights into the remarkably long photoinduced vibrational coherence of PtPOP in solution[28]. The structure of the complex, consisting of square planar $PtP_4$ units linked by rigid P-O-P bridging ligands, provides a highly harmonic force constant for the Pt-Pt vibrations and shields the metal atoms from collisions with solvent molecules. Therefore, pure dephasing is inefficient and decoherence is essentially driven by relaxation of the excess vibrational energy along the Pt-Pt coordinate. Despite these advancements in the understanding of the mechanism of vibrational decoherence of the electronically excited PtPOP complex in solution, several questions remain unanswered: What are the pathways of vibrational energy transfer to the solvent? Is the energy transferred directly from the Pt atoms? Does energy dissipation occur via collisions or are solute-solvent long-range electrostatic interactions also playing a role? Ultimately, what is the mechanism of vibrational energy relaxation that accounts for

the exceptionally slow decoherence of the photoexcited PtPOP complex in solution?

Nonequilibrium molecular dynamics simulations can be used to analyze the pathways of energy flow from a vibrationally excited solute to a solvent based on the instantaneous atomic forces arising from the solute-solvent interactions[35–43]. This approach is commonly referred to as energy flux, or power-work analysis, since the portion of excess excitation energy transferred to accepting degrees of freedom over a given time interval is obtained as the time integral of the power computed from the atomic forces acting on the excited or accepting degrees of freedom. The approach has been used to investigate the pathways of energy relaxation of vibrationally excited molecules in gas and condensed phase, including a water molecule excited along the bending mode in liquid water[36,37], azulene in carbon dioxide[40,41], nitromethane in argon and water[35], and methyl chloride in water[42]. In these previous studies, the interactions between the atoms in the solute-solvent system were modelled using potential energy functions, and the vibrational modes were obtained as normal modes of vibration from the mass-weighted force constant matrix of either the vacuum equilibrium solute geometry or its instantaneous structures in solution[35,40,41].

In the present work, an approach is presented to analyze the flow of excess vibrational energy of a solvated molecule using instantaneous atomic forces obtained from nonequilibrium QM/MM molecular dynamics simulations, where the electronic degrees of freedom of the solute are described explicitly through electronic structure calculations and the solvent is described using potential energy functions. This makes it possible to account for the polarization of the electron density of the excited solute by the solvent. Moreover, in the approach introduced here, the vibrational modes of the excited molecule are obtained through a generalized normal mode analysis using the covariance matrix of instantaneous mass-weighted velocities[44]. This method avoids the need to compute the Hessian matrix for several atomic configurations and inherently includes finite-temperature and anharmonic effects. By projecting the atomic forces along the generalized normal modes, it is possible to decompose the vibrational energy flux into contributions by individual atoms, thus providing insights into the specific interatomic interactions that drive the transfer of energy from the excited solute to the solvent.

The energy flux analysis is applied here to nonequilibrium QM/MM adiabatic molecular dynamics simulations of PtPOP excited to the lowest singlet excited electronic state in liquid water and acetonitrile. In these simulations, the photoexcited complex is described using

orbital-optimized density functional calculations[45–48], while the solvent is modelled using potential energy functions, with the two parts of the system coupled through an embedding scheme. For both solvents, it is found that the flow of excess energy from the initially excited pinching mode to the solvent is governed by interactions between the atoms of the ligands and the surrounding solvent molecules, mainly short-range repulsive and attractive interactions represented by a Lennard-Jones potential. In water, where solvent molecules are found to transiently coordinate the Pt atoms of the complex, a significant portion of energy is transferred directly from the Pt atoms to the solvent via short-range interactions. However, a similar amount of energy is simultaneously transferred from the solvent to the Pt atoms through longer range electrostatic interactions, resulting in no net loss of energy from the Pt atoms. Since the contribution of ligand motion to the pinching mode is relatively small, the vibrational energy dissipation is inefficient. This explains the exceptionally long-lived ($\sim$1.6 ps) and solvent-independent coherent Pt-Pt oscillations of the electronically excited PtPOP complex in solution.

## II. METHODOLOGY

### A. QM/MM embedding scheme

The molecular dynamics simulations make use of an additive QM/MM embedding scheme[49–51], typically referred to as electrostatic embedding, where the total Hamiltonian of the system is given by three terms:

$$\hat{\mathbf{H}} = \hat{\mathbf{H}}_{\mathrm{QM}} + \hat{\mathbf{H}}_{\mathrm{QM/MM}} + \hat{\mathbf{H}}_{\mathrm{MM}} \tag{1}$$

The first term, $\hat{\mathbf{H}}_{\mathrm{QM}}$, is the Hamiltonian of interaction between quantum mechanically described electrons and nuclei described as classical particles. The electrons in the QM part are described using the Kohn-Sham (KS)[52,53] density functional approach.

$\hat{\mathbf{H}}_{\mathrm{MM}}$ describes interparticle interactions within the MM part, as modelled using potential energy functions. In the present case, the MM particles are represented by a fixed-value point charge force field depending only on the position of the MM particles, and the short-range interactions are described using a Lennard-Jones (LJ) potential. Thus, $\hat{\mathbf{H}}_{\mathrm{MM}}$ is constant for given coordinates of atoms in the MM part and corresponds to the energy of interaction between them, $\hat{\mathbf{H}}_{\mathrm{MM}} = E_{\mathrm{MM}}$.

The QM/MM interaction Hamiltonian, $\hat{\mathbf{H}}_{\mathrm{QM/MM}}$, describes electrostatic interactions (el) as well as short-range repulsion and attraction (sr) between the QM and MM particles:

$$\hat{\mathbf{H}}_{\mathrm{QM/MM}} = \hat{\mathbf{H}}_{\mathrm{el}} + \hat{\mathbf{H}}_{\mathrm{sr}} = -\sum_{m\in\mathrm{MM}} \frac{q_m}{|\mathbf{r}-\mathbf{R}_m|} + \sum_{\substack{m\in\mathrm{MM}\\ \alpha\in\mathrm{QM}}} \frac{q_m \mathcal{Z}_\alpha}{|\mathbf{R}_\alpha - \mathbf{R}_m|} + \hat{\mathbf{H}}_{\mathrm{sr}} \tag{2}$$

where $\mathbf{r}$, $\mathbf{R}_\alpha$ and $\mathbf{R}_m$ are the position vectors of the electrons and nuclei in the QM part and the MM sites, respectively, and $q_m$ and $\mathcal{Z}_\alpha$ are the charges of the MM sites and QM nuclei, respectively. Here, the short-range repulsive and attractive interactions between the QM and MM atoms (or sites) are described using a Lennard-Jones potential:

$$\hat{\mathbf{H}}_{\mathrm{sr}} = E_{\mathrm{sr}} = \sum_{\substack{m\in\mathrm{MM}\\ \alpha\in\mathrm{QM}}} 4\epsilon_{m\alpha}\left[\left(\frac{\sigma_{m\alpha}}{|\mathbf{R}_\alpha - \mathbf{R}_m|}\right)^{12} - \left(\frac{\sigma_{m\alpha}}{|\mathbf{R}_\alpha - \mathbf{R}_m|}\right)^{6}\right] \tag{3}$$

where $\epsilon_{m\alpha}$ is the depth of the potential energy well and $\sigma_{m\alpha}$ is the distance at which $E_{\mathrm{sr}}$ is zero. The electronic positions appear only in the first term of the interaction Hamiltonian, $\hat{\mathbf{H}}_{\mathrm{QM/MM}}$, on the right-hand side of eq 2, representing the electrostatic potential of the MM particles. Therefore, the self-consistent field wave function optimization in the KS calculation is modified only by the inclusion of this additional external potential energy term, accounting for the polarization of the QM electron density by the MM charges.

The total energy of the system consists of the sum of the three terms:

$$E = E_{\mathrm{QM}} + E_{\mathrm{QM/MM}} + E_{\mathrm{MM}} \tag{4}$$

where the interaction energy, $E_{\mathrm{QM/MM}}$, includes the energy of electrostatic interactions, $E_{\mathrm{el}}$, and short-range repulsive exchange as well as attractive interactions, $E_{\mathrm{sr}}$, between the QM and MM particles:

$$E_{\mathrm{QM/MM}} = E_{\mathrm{el}} + E_{\mathrm{sr}} = -\sum_{m\in\mathrm{MM}} \int \frac{q_m n(\mathbf{r})}{|\mathbf{r}-\mathbf{R}_m|}\mathrm{d}\mathbf{r} + \sum_{\substack{m\in\mathrm{MM}\\ \alpha\in\mathrm{QM}}} \frac{q_m \mathcal{Z}_\alpha}{|\mathbf{R}_\alpha - \mathbf{R}_m|} + E_{\mathrm{sr}} \tag{5}$$

with $n(\mathbf{r})$ being the electron density of the QM part. In the present simulations, the QM part always includes only the PtPOP complex as the solute, while the MM part includes all the solvent molecules.

## B. Generalized normal modes

A generalized normal mode analysis[54] as presented by Strachan[44] is adopted here. According to this approach, generalized normal modes of a system of $N$ atoms at finite temperature

are defined as the $3N$ modes with velocities $\dot{Q}_i$ that satisfy the relation:

$$\left\langle \dot{Q}_i(t)\dot{Q}_j(t) \right\rangle \propto \delta_{ij} \qquad i,j = 1,2,\ldots,3N \tag{6}$$

where $\langle \ldots \rangle$ indicates time averaging and $\delta_{ij}$ is the Kronecker delta. These modes can be found by diagonalizing the following covariance matrix of mass-weighted velocities:

$$\mathbf{K} = \frac{1}{2} \left\langle \dot{\mathbf{q}}'(t)\dot{\mathbf{q}}'^{\dagger}(t) \right\rangle \tag{7}$$

where $\dot{\mathbf{q}}'$ is a column vector of the mass-weighted velocities $\dot{q}'_k = \sqrt{m_k}\dot{q}_k$, $k = 1,2,\ldots,3N$, defined in the frame of reference that translates and rotates with the molecule (body-fixed-frame velocities) as determined from the molecular dynamics simulations. Instantaneous generalized normal mode velocities are given by:

$$\dot{\mathbf{Q}}(t) = \mathbf{L}^{\dagger}\dot{\mathbf{q}}'(t) \tag{8}$$

where $\mathbf{L}$ is the unitary matrix that diagonalizes $\mathbf{K}$. The generalized normal mode velocities $\dot{Q}_i$ satisfy the condition in eq 6, since $\left\langle \dot{\mathbf{Q}}(t)\dot{\mathbf{Q}}^{\dagger}(t) \right\rangle = 2\mathbf{T}$, where $\mathbf{T}$ is a diagonal matrix with the average kinetic energy of the generalized normal modes along the diagonal. The instantaneous kinetic energy can be expressed as a sum over the generalized normal modes:

$$T(t) = \frac{1}{2}\dot{\mathbf{Q}}^{\dagger}(t)\dot{\mathbf{Q}}(t) = \frac{1}{2}\sum_{i}^{3N} \dot{Q}_i^2(t) = \sum_{i}^{3N} T_i(t) \tag{9}$$

### C. Solute-solvent energy flux

The time variation of the kinetic energy of a generalized normal mode $i$ (power, $P_i$) is given by:

$$P_i(t) = \frac{\mathrm{d}T_i(t)}{\mathrm{d}t} = \dot{Q}_i(t)\mathbf{L}_i^{\dagger} \cdot \frac{\mathrm{d}\dot{\mathbf{q}}'(t)}{\mathrm{d}t} = \dot{Q}_i(t)\mathbf{L}_i^{\dagger} \cdot \mathbf{F}'(t) \tag{10}$$

where $\mathbf{L}_i$ is a column vector of the transformation matrix $\mathbf{L}$ (see eqs 7 and 8), representing the mode $i$, and $\mathbf{F}'(t)$ is a vector of mass-weighted atomic force components $F'_k(t) = F_k(t)/\sqrt{m_k}$, $k = 1,2,\ldots,3N$, as available from the molecular dynamics simulations. A change of kinetic energy of a generalized normal mode $i$ (work, $W_i$) over a time interval $\tau$ can be computed as:

$$W_i(\tau) \equiv \Delta T_i(\tau) = \int_0^{\tau} P_i(t)\mathrm{d}t = \int_0^{\tau} \dot{Q}_i(t)\mathbf{L}_i^{\dagger} \cdot \mathbf{F}'(t)\mathrm{d}t \tag{11}$$

For the molecular dynamics simulations using the QM/MM scheme presented in section II A, the instantaneous power of a generalized normal mode of the solute can be partitioned into contributions from each solute atom according to:

$$P_i(t) = \sum_{\alpha \in \mathrm{QM}} P_i^{\alpha}(t) = \sum_{\alpha \in \mathrm{QM}} \dot{Q}_i(t) \mathbf{L}_i^{\alpha\dagger} \cdot \mathbf{F}'_{\alpha}(t) \tag{12}$$

where $\mathbf{L}_i^{\alpha\dagger}$ includes only the coefficients of the generalized normal mode transformation corresponding to solute atom $\alpha$ and $\mathbf{F}'_{\alpha}(t)$ is the vector of the mass-weighted instantaneous force acting on solute atom $\alpha$. Accordingly, the kinetic energy change for mode $i$ can be partitioned into contributions from the work of each solute atom:

$$W_i(\tau) = \sum_{\alpha \in \mathrm{QM}} W_i^{\alpha}(\tau) = \sum_{\alpha \in \mathrm{QM}} \int_0^{\tau} \dot{Q}_i(t) \mathbf{L}_i^{\alpha\dagger} \cdot \mathbf{F}'_{\alpha}(t) \mathrm{d}t \tag{13}$$

In the QM/MM coupling of the solute-solvent system adopted here, the force on a QM atom includes terms due to the QM interactions, $\mathbf{F}_{\alpha}^{\mathrm{QM}} = -\partial E_{\mathrm{QM}}/\partial \mathbf{R}_{\alpha}$, the electrostatic interaction between solute and solvent, $\mathbf{F}_{\alpha}^{\mathrm{el}} = -\partial E_{\mathrm{el}}/\partial \mathbf{R}_{\alpha}$, and other, short-range interactions between solute and solvent, $\mathbf{F}_{\alpha}^{\mathrm{sr}} = -\partial E_{\mathrm{sr}}/\partial \mathbf{R}_{\alpha}$, respectively, where $\mathbf{R}_{\alpha}$ is the position vector of QM atom $\alpha$:

$$\mathbf{F}_{\alpha}(t) = \mathbf{F}_{\alpha}^{\mathrm{QM}}(t) + \mathbf{F}_{\alpha}^{\mathrm{el}}(t) + \mathbf{F}_{\alpha}^{\mathrm{sr}}(t) \tag{14}$$

Therefore, the kinetic energy change of a vibrational mode of the solute can be partitioned into contributions from the work of QM forces and the work due to the forces exerted by the solvent on the solute atoms via electrostatic and shorter range repulsive and attractive interactions:

$$W_i(\tau) = \sum_{\alpha \in \mathrm{QM}} \left[ W_i^{\alpha,\mathrm{QM}}(\tau) + W_i^{\alpha,\mathrm{el}}(\tau) + W_i^{\alpha,\mathrm{sr}}(\tau) \right] = W_i^{\mathrm{QM}}(\tau) + W_i^{\mathrm{el}}(\tau) + W_i^{\mathrm{sr}}(\tau) \tag{15}$$

where:

$$\begin{aligned} W_i^{\mathrm{QM}} &= \sum_{\alpha \in \mathrm{QM}} W_i^{\alpha,\mathrm{QM}} \\ W_i^{\mathrm{el}} &= \sum_{\alpha \in \mathrm{QM}} W_i^{\alpha,\mathrm{el}} \\ W_i^{\mathrm{sr}} &= \sum_{\alpha \in \mathrm{QM}} W_i^{\alpha,\mathrm{sr}} \end{aligned} \tag{16}$$

Neglecting the polarization of the solute by the electrostatic potential of the solvent, the

first term of the right-hand side of eq 15 includes intramolecular vibrational redistribution (see Appendix A), while the last two terms account for the transfer of energy between the vibrational mode $i$ of the solute and the solvent, i.e. the external energy flux. Although the external energy flux terms, $W_i^{\mathrm{el}}(\tau)$ and $W_i^{\mathrm{sr}}(\tau)$, have been derived here using only the normal mode kinetic energy, they correspond to the fraction of total energy of a mode transferred to the solvent, as shown in Appendix A using a normal mode decomposition of the intramolecular potential energy.

Overall, by using the instantaneous QM/MM forces acting on the solute atoms, it is possible to monitor the flux of energy between vibrational modes of the solute to the solvent, and analyze it in terms of contributions from individual atoms of the solute. In the present work, this solute-solvent energy flux approach is applied to identify pathways of vibrational energy relaxation of the PtPOP complex electronically excited in solution using nonequilibrium QM/MM molecular dynamics simulations.

### D. Model parameters

Two sets of QM/MM direct molecular dynamics simulations of the PtPOP complex in solution are performed, one with water and the other with acetonitrile as the solvent. For the simulations in water, the system includes the PtPOP complex and 2710 solvent molecules in a cubic simulation box 43.5 Å wide. The simulations in acetonitrile include the PtPOP complex and 2728 solvent molecules in a cubic box 62.2 Å wide.

In all simulations, the QM/MM partition is fixed. The QM part includes only the PtPOP complex described using KS density functional calculations, employing the BLYP functional[55] and the D3 approximation of dispersion interactions[56] together with the Becke-Johnson damping function[57]. The BLYP functional has been found in a previous study[28] to provide a PtPOP equilibrium solution structure as well as excited state structural changes and Pt-Pt oscillation period in close agreement with experimental values, when used in QM/MM simulations. The use of a computationally efficient generalized gradient approximation functional without introducing Hartree-Fock exchange makes it possible to collect a statistically significant amount of molecular dynamics data. The calculations use a projector augmented wave (PAW) approach[58,59], where the core electrons are frozen based on the results of reference scalar relativistic calculations of the isolated atoms, while the smooth

pseudo wave functions of the valence electrons are represented with tzp and a dzp basis sets of numerical atomic orbitals[60] centered on the Pt atom and on all other atoms, respectively. The KS calculations are performed on a uniform grid within a QM box with 0.18 Å spacing between the grid points. The size of the QM box ensures at least 5.0 Å of vacuum between any atom and the box edges. The excited state calculations use a time-independent approach where the orbitals are variationally optimized in a state-specific manner[45–48]. The lowest open-shell singlet excited state is represented within the spin-restricted formalism by targeting a nonaufbau KS solution corresponding to excitation of one electron from the ground state HOMO to the LUMO[28,61,62]. As shown earlier[9,28] and confirmed here by inspection of the molecular orbitals, the HOMO has prevalent d$\sigma^*$ antibonding character resulting from the interaction of Pt $d_{z^2}$ orbitals, while the LUMO has prevalent p$\sigma$ bonding character resulting from the interaction of Pt $p_z$ orbitals. The excited state calculations are performed using a direct orbital optimization method, which employs the exponential transformation and a limited-memory symmetric rank-one quasi-Newton algorithm[48,63]. The initial maximum overlap method[64] is employed to reduce the risk of variational collapse to the ground state.

For the MM part, water molecules are described with the TIP4P force field[65], while acetonitrile molecules are described with the interaction potential of Guàrdia et al.[66] based on a rigid linear three-site molecular geometry. Since the total charge of the PtPOP complex is equal to -4, four $K^+$ counterions are included in the MM part to charge neutralize the simulation box. The coupling between the QM and MM parts makes use of the QM/MM scheme illustrated in section II A. The parameters of the LJ potential function representing the short-range QM/MM interaction (eq 3) are obtained by fitting values of the binding energy calculated using the BLYP functional supplemented with the D3 approximation of dispersion interactions for a range of solute-solvent clusters as described in the Supplementary Material.

In the dynamics simulations, the geometry of solvent molecules and the distances between any of the hydrogen atoms and the two nearest oxygen atoms in the complex are kept rigid. These constrains are enforced using the RATTLE algorithm[67], except for the acetonitrile molecules, where holonomic constraints for linear triatomic configurations are used[68]. Energy transfer from the solute to the internal vibrational modes of the solvent during the solute vibrational relaxation is typically found to be negligible[69,70], so the use of

a rigid geometry for the solvent molecules should not significantly affect the results of the excited state simulations. The four $K^+$ counterions are kept more than 16 Å away from the geometric center of the PtPOP complex by applying a repulsive harmonic potential[28].

The system is first equilibrated in the ground electronic state in the canonical ensemble at 300 K using a Langevin thermostat and a time step of 2.0 fs. In total, 100000 equilibrated ground state configurations are collected for each type of solvent, corresponding to trajectories spanning 200 ps with the thermostat applied only to the solvent molecules. For each type of solvent, 50 nonequilibrium molecular dynamics trajectories are calculated within the Born-Oppenheimer approximation, each started by exciting the complex to the lowest singlet excited state using atom coordinates and momenta obtained from configurations of the equilibrated ground state trajectories separated by at least 4 ps. Optical experiments show that the ground state is repopulated on much longer timescales, on the order of a few $\mu s$[9,25]. Moreover, previous QM/MM simulations using time-dependent DFT have shown that higher singlet excited states remain energetically well-separated from the lowest one during the dynamics[15]. Therefore, no internal conversion occurs within 4 ps after excitation, and the adiabatic propagation on a single excited state is justified. The first excited state calculation for each trajectory is initialized using the orbitals of the ground state with occupation numbers reflecting promotion of an electron from the HOMO to the LUMO, i.e. the HOMO and LUMO open-shell orbitals are assigned an occupation number of 1, while the other, closed-shell orbitals are assigned an occupation number of 2. Excited state calculations at subsequent steps in the trajectory propagation use the occupied optimized orbitals of the previous molecular dynamics step as initial guess. For the nonequilibrium molecular dynamics simulations, a time step of 2.0 fs is used, and the Langevin thermostat is applied only to solvent molecules far from the solute, while the PtPOP complex and the closest solvent molecules are not coupled to the heat bath. The thermostat is switched on gradually, increasing the friction coefficient linearly from 0 to 1 $ps^{-1}$ within a 2 Å buffer region extending radially in the simulation cell starting from a radius of 12 Å from the geometric center of the solute. Each nonequilibrium excited state trajectory spans 6 ps. Time-dependent radial distribution functions (RDFs) of the distance between solute atoms of a given element or a site, such as the center of mass, and solvent atoms of a given element are calculated by averaging over the nonequilibrium excited state trajectories. The time-dependent cumulative coordination number is then obtained by integrating the RDFs,

$g(d,t)$:

$$CN(d',t) = 4\pi\frac{N}{V}\int_0^{d'} g(d,t)d^2\,\mathrm{d}d \tag{17}$$

where $N$ is the number of solvent atoms and $V$ is the volume of the simulation box.

The QM/MM direct molecular dynamics simulations are performed using the atomic simulation environment (ASE)[71] and the grid-based projector augmented wave (GPAW) software[72], where the QM/MM embedding scheme employed here is implemented[49,50].

For the calculations of the generalized vibrational normal modes of PtPOP from the nonequilibrium excited state QM/MM trajectories for a given solvent, the body-fixed-frame velocities are first obtained by removing the contribution of overall rotation and translation of the complex from the Cartesian velocities, as described in ref[28]. Then, the covariance matrix of velocities as defined in eq 7 is calculated, with the average carried out over all 50 excited state trajectories and all time steps. Finally, the velocity covariance matrix is diagonalized to obtain the normal mode eigenvectors used in eqs 10-16 to analyze the flux of vibrational energy from the photoexcited complex to the solvent. In the present work, the energy flux associated with the pinching mode of PtPOP is analyzed, which mostly involves a change in the distance between the Pt atoms. As shown below, this mode accepts most of the excess energy due to the photoexcitation. Since the vibrational temperature of this mode is smaller than $T = 300$ K ($h\nu/k_\mathrm{B} \approx 170$ K, where $\nu$ is the vibrational frequency in the ground state), the equilibrium ground state distributions of mode coordinate and kinetic energy generated through classical sampling according to the equilibration procedure described above closely approximate quantum mechanical distributions[73]. Therefore, quantum effects on the initial conditions for the nonequilibrium dynamics of the pinching mode are expected to be small.

## III. RESULTS

### A. Coherent vibrational dynamics

As expected based on previous studies[28], most of the excess vibrational energy gained by the complex by photoexcitation, ∼60 % in both solvents (see the Supplementary Material), is initially concentrated in a vibrational mode corresponding to change in the distance between the two Pt atoms (hereafter referred to as pinching normal mode). In the following we focus on the coherent dynamics and energy relaxation along this vibrational mode.

Figure 1 shows the normal mode displacement vectors obtained for both water and acetonitrile solvents. The pinching mode is dominated by oscillations in the distance between the two Pt atoms, but also involves a small contribution from the bending of the ligands: As the distance between the Pt atoms decreases (or increases) during the normal mode oscillations, the bridging O atoms are projected outwards (inwards), while the other ligand atoms are projected slightly inwards (outwards), corresponding to a decrease (increase) of the magnitude of the ∠P-O-P angles. This ligand bending contribution is more pronounced

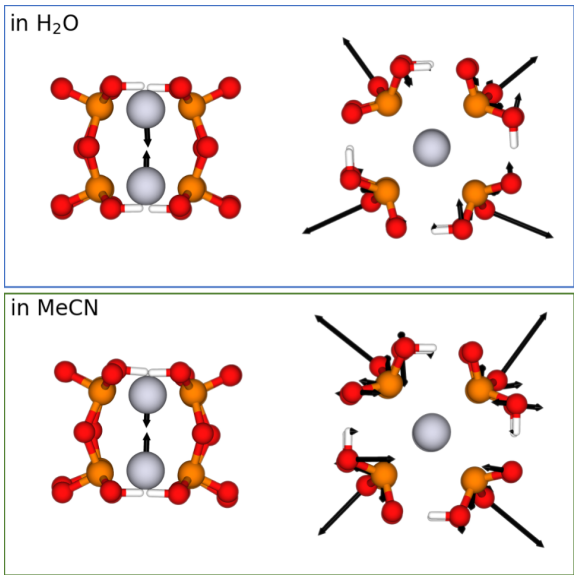


FIG. 1. Visualization of the PtPOP molecule with the displacement vectors of the pinching mode obtained from a generalized normal mode analysis of nonequilibrium excited state QM/MM molecular dynamics trajectories in water (top) and acetonitrile (bottom). Left: displacement vectors of the Pt atoms. Right: displacement vectors of the ligand atoms magnified by a factor of 12 for better visualization. Pt, P, O, and H atoms are grey, orange, red, and white, respectively. The pinching mode involves mostly a change in the distance between the two Pt atoms and also a small contribution of ligand bending, the latter being more pronounced in acetonitrile than in water.

in acetonitrile than in water, pointing to greater structural rigidity in the latter solvent, likely as a result of hydrogen bonds between the water molecules in the first solvation shell and the O ligand atoms of PtPOP (see also Figure 5).

Figure 2 shows the time evolution of the pinching mode averaged over the nonequilibrium excited state trajectories for both water and acetonitrile. Initially, the nonequilibrium

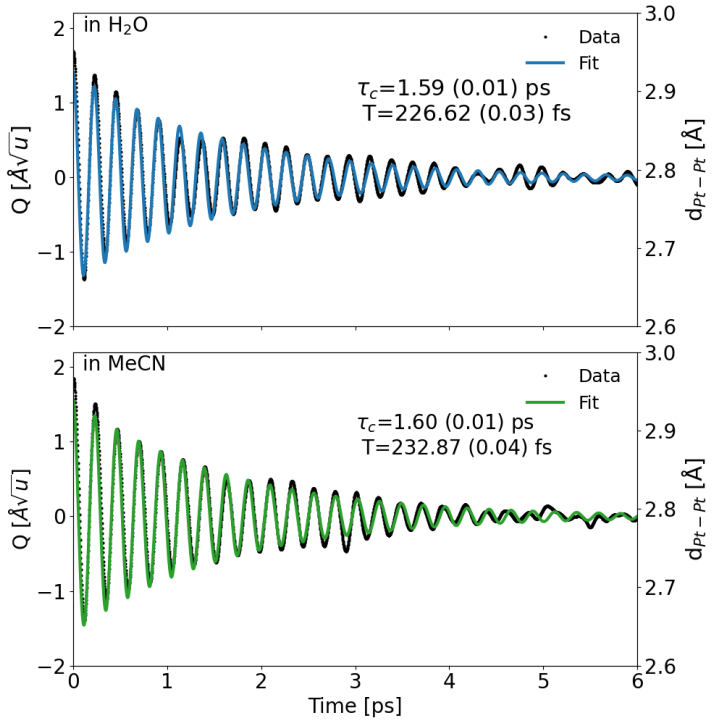


FIG. 2. Time evolution of the average pinching mode obtained from nonequilibrium QM/MM molecular dynamics trajectories of PtPOP excited to the lowest singlet excited state in water (top) and acetonitrile (bottom). The standard error of the time-dependent average Pt-Pt distance is always below 0.02 Å. The oscillation period, $T$, and coherence decay time, $\tau_c$, are obtained from fitting a periodic function with an exponentially decaying amplitude. The values in parentheses are the standard errors of the fits. The decoherence time is in close agreement with the results of ultrafast transient absorption and fluorescence up-conversion experiments of PtPOP in water[16] ($\tau_c$ of 1.76±0.08 and 1.5±0.5 ps, respectively), where intersystem crossing occurs on longer time scale than vibrational relaxation[16] ($\tau_{ISC} > 13$ ps).

ensemble of PtPOP molecules has an average Pt-Pt bond length of ∼2.93 Å, corresponding to the equilibrium bond length in the ground state. Excitation to the lowest singlet excited state induces coherent oscillations of the Pt-Pt distances in the ensemble over nearly 6 ps, after which the average Pt-Pt distance equilibrates to around 2.80 Å. The instantaneous average normal mode coordinate is fitted with a periodic function with an exponentially decaying amplitude:

$$f_c(t) = Ae^{-t/\tau_c} \cos\left(\frac{2\pi}{T}t\right) + B \tag{18}$$

where $T$ is the period of the coherent oscillations and $\tau_c$ is the decoherence decay time. The fits give very similar oscillation periods and decoherence time for the two solvents: $T = 226.62$ fs and $\tau_c = 1.59$ ps in water, and $T = 232.87$ fs and $\tau_c = 1.60$ ps in acetonitrile. The calculated periods agree very well with the value of $\sim$224 fs obtained from previous transient absorption experiments in water[16] and acetonitrile[15]. For water, where intersystem crossing to the lowest triplet state occurs after vibrational relaxation in the singlet excited state ($\tau_{ISC} > 13$ ps as determined experimentally[16]), the calculated coherence decay time is very close to the values of 1.76$\pm$0.08 and 1.5$\pm$0.5 ps obtained from transient absorption and fluorescence up-conversion measurements[16], respectively. For acetonitrile, the simulations yield a slower decoherence compared to transient absorption experiments: The experimental coherence decay time for photoinduced vibrations in the lowest singlet excited state in this case is 1.1$\pm$0.1 ps[15]. However, for this solvent, intersystem crossing is observed to occur simultaneously to vibrational relaxation ($\tau_{ISC} = 0.7 - 0.9$ ps[15]). Therefore, the experimental value of decoherence time in acetonitrile is affected by intersystem crossing, but the present simulations do not account for this effect.

Figure 3 shows the time evolution of the kinetic energy of the pinching mode averaged over the nonequilibrium excited state trajectories for both water and acetonitrile. The instantaneous pinching normal mode kinetic energy is fitted with the following periodic function with an exponentially decaying amplitude:

$$f_e(t) = Ce^{-t/\tau_e} \cos^2\left(\frac{2\pi}{T}t + \frac{\pi}{2}\right) + D \tag{19}$$

where $\tau_e$ is the vibrational energy relaxation time, or vibrational cooling time. The values of the vibrational cooling time obtained from the fits are 0.75 and 0.89 ps in water and acetonitrile, respectively. Decoherence can result from both energy relaxation and pure dephasing, i.e. changes in the frequency and phase of the individual oscillators in the ensemble caused by stochastic collisions with the solvent and anharmonic effects. A decoherence time almost twice as long as the vibrational energy relaxation time indicates that the vibrational phase is to a large extent preserved during the energy relaxation and that pure dephasing effects are minimal in both solvents. As has been noted elsewhere[16,28], this is likely due to the high degree of harmonicity of the Pt-Pt interaction and a cage-like ligand structure protecting the Pt-Pt oscillations from stochastic collisions with solvent molecules.

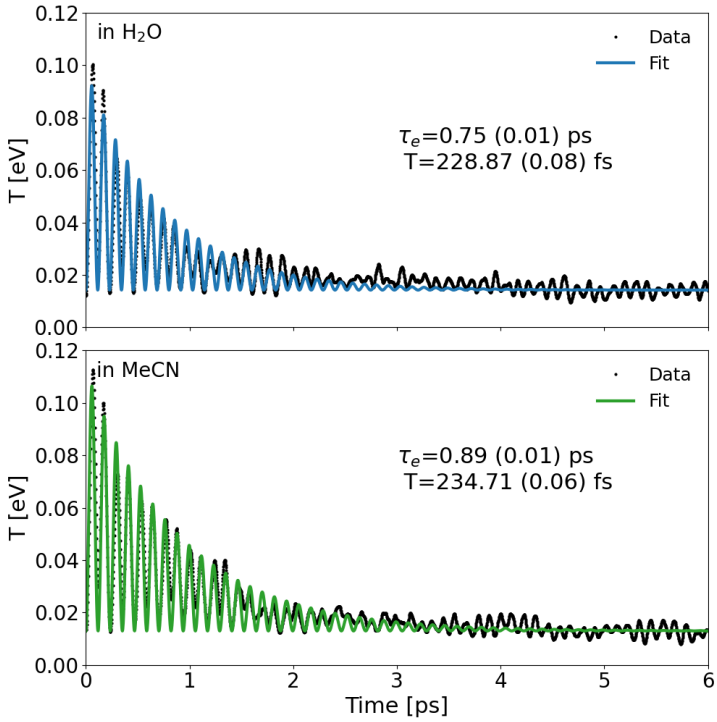


FIG. 3. Time evolution of the average kinetic energy in the pinching normal mode obtained from nonequilibrium QM/MM molecular dynamics trajectories of PtPOP excited to the lowest singlet excited state in water (top) and acetonitrile (bottom). The standard error of the time-dependent average kinetic energy is always below 0.012 eV. The vibrational decay time, $\tau_e$, is obtained from fitting a periodic function with an exponentially decaying amplitude. The values in parentheses are the standard errors of the fits. The calculated $\tau_e$ is almost half the coherence decay time, $\tau_c$, which shows that for both water and acetonitrile vibrational coherence is lost as a result of vibrational cooling and not pure dephasing.

## B. Solvation shell structure and dynamics

Figure 4 shows the RDFs of the distance between the center of mass of PtPOP and the H and methyl sites of water and acetonitrile, respectively, sampled from the thermally equilibrated ground state trajectories as well as the nonequilibrium excited state trajectories. In the ground state of PtPOP in water, the small peak at short distance ($d < 4$ Å) represents the solvation shell closest to the Pt atoms of the complex. This peak includes water molecules that transiently coordinate to the Pt atoms, with an O−H$\cdots$Pt preferential orientation and

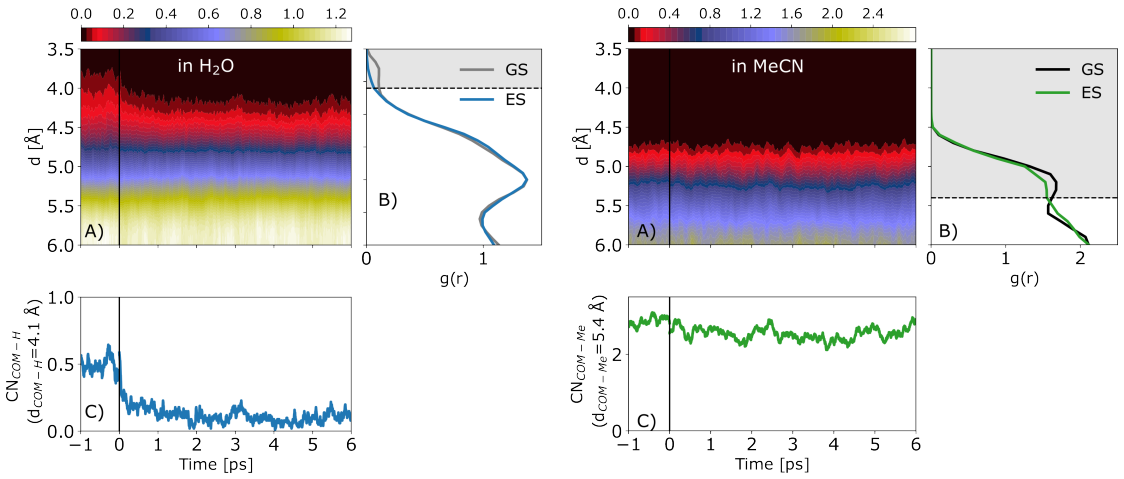


FIG. 4. A) Instantaneous radial distribution functions (RDFs) of the distance between the center of mass of PtPOP and the H and methyl sites of water (left) and acetonitrile (right). The vertical black line indicates the time where the complex is excited to the lowest singlet excited state. B) Equilibrium ground (GS) and excited (ES) state RDFs, the latter obtained as an average over the last 2.0 ps of the nonequilibrium propagation. C) Instantaneous cumulative coordination number (CN) of the distance between the center of mass of PtPOP and the H and methyl sites of water and acetonitrile calculated for the distances included in the shaded regions in panels B). The solvation shell of the ground state of PtPOP in water involves a transient coordination of water molecules to the Pt atoms, which is lost after photoexcitation. The solvation shell in acetonitrile is less structured and no significant rearrangement occurs upon excitation.

a Pt−H distance of around 2.5 Å, as visualized in Figure 5 (see also the Pt−H and Pt−O solute-solvent RDFs shown in the Supplementary Material).

As shown by the instantaneous RDFs and cumulative coordination number in Figure 4, excitation to the lowest singlet excited state and contraction of the Pt-Pt distance leads to desolvation of the closely coordinating water molecules, resulting in the loss of the first coordination shell within ∼1 ps, corresponding to around four full periods of the Pt-Pt coherent oscillations. This behavior is similar to what has previously been observed in the excited state dynamics of the $[Ir_2(dimen)_4]^{2+}$ (dimen = diisocyano-para-menthane) complex in acetonitrile[73,74], although in the latter case the initial loss of coordination of the solvent methyl groups to the Ir atoms is followed by coordination by the strongly electron donating nitrogen atoms of the solvent. The ground state solute-solvent RDFs of PtPOP in acetoni-

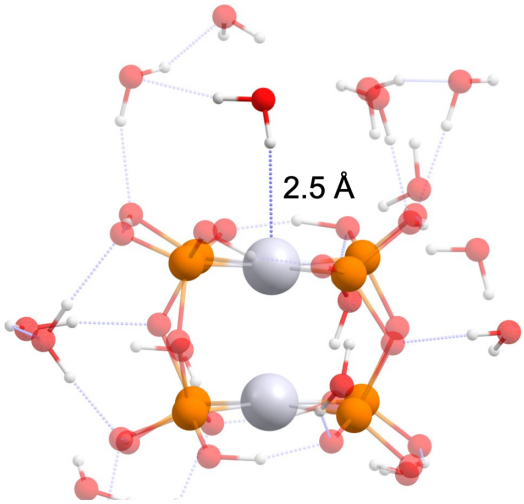


FIG. 5. Visualization of a frame from an equilibrium QM/MM molecular dynamics trajectory of PtPOP in the ground state dissolved in water, highlighting the close coordination of a water molecule to a Pt atom and the hydrogen bonds involving the ligand atoms of the complex.

trile appear broader, indicating a lower degree of ordering in the solvation shell compared to water. No peak is observed in the Pt−solvent RDFs below 3 Å (see the Supplementary Material), suggesting that there is no strong coordination between the acetonitrile molecules and the Pt atoms. Finally, for this solvent, the solute-solvent RDFs show no significant changes upon photoexcitation.

### C. Analysis of solute-solvent energy flux

Figure 6 shows the instantaneous total work on the pinching mode computed as an average over the nonequilibrium excited state trajectories in water and acetonitrile, corresponding to the change $T(\tau) - T(0)$ of the instantaneous kinetic energy (see also Figure 3). Figure 6 also shows how the total work is partitioned into internal work due to QM forces, $W^{\mathrm{QM}}$, and external work due to electrostatic as well as short-range repulsive and attractive forces exerted by the solvent, $W^{\mathrm{el}}$ and $W^{\mathrm{sr}}$, respectively, as obtained according to eqs 13−16. The work due to the QM forces remains positive at all times after excitation for both solvents. In contrast, the work due to solute-solvent electrostatic and short-range forces is negative and corresponds to the energy transferred from the normal mode to the solvent during the vibrational relaxation following electronic excitation. The work done by the short-range

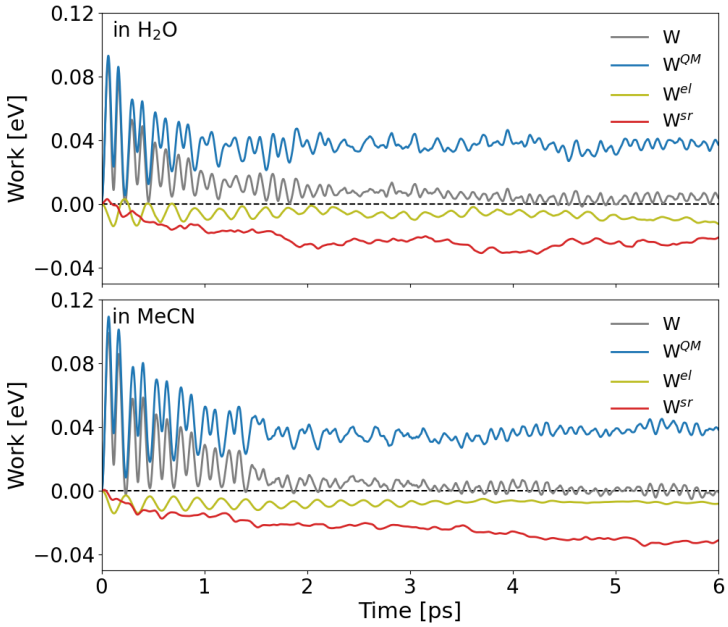


FIG. 6. Time evolution of the average total work associated with the pinching mode obtained from nonequilibrium QM/MM molecular dynamics trajectories of the PtPOP complex excited to the lowest singlet excited state in water (top) and acetonitrile (bottom). The contributions of the internal work due to QM forces ($W^{\mathrm{QM}}$), as well as the external work due to electrostatic as well as short-range repulsive and attractive Lennard-Jones (LJ) forces exerted by the solvent ($W^{\mathrm{el}}$ and $W^{\mathrm{sr}}$) are also shown. The work of electrostatic forces oscillates around a constant negative value with the same period as the oscillations of the normal mode, while the work of the short-range forces decreases monotonically. At the end of the nonequilibrium dynamics, most of the excess vibrational energy of the complex has been transferred to the solvent via the short-range LJ interactions.

interactions described using the LJ potential of eq 3, decreases monotonically. Meanwhile, the work done by the solute-solvent electrostatic forces reaches a minimum after the first contraction of the Pt-Pt distances in the ensemble, and then exhibits coherent oscillations with the same period as the normal mode vibrations. Minima in the oscillations of the work of electrostatic forces correspond to minima in the oscillations of the normal mode, which are shown in Figure 2. This means that the electrostatic forces exerted by the solvent act

to increase the distance between the $PtP_4$ groups in PtPOP, suggesting that solvation is more effective when the complex is elongated along the Pt-Pt distance. At the end of the nonequilibrium dynamics, most of the excess vibrational energy acquired in the pinching mode in the excitation, ∼63 % for water and ∼79 % for acetonitrile, is transferred to the solvent via the short-range LJ interactions.

The contribution of the Pt and ligand atoms of the complex to the flux of energy from the pinching mode to the solvent is analyzed in Figures 7 and 8. Figure 7 shows that the

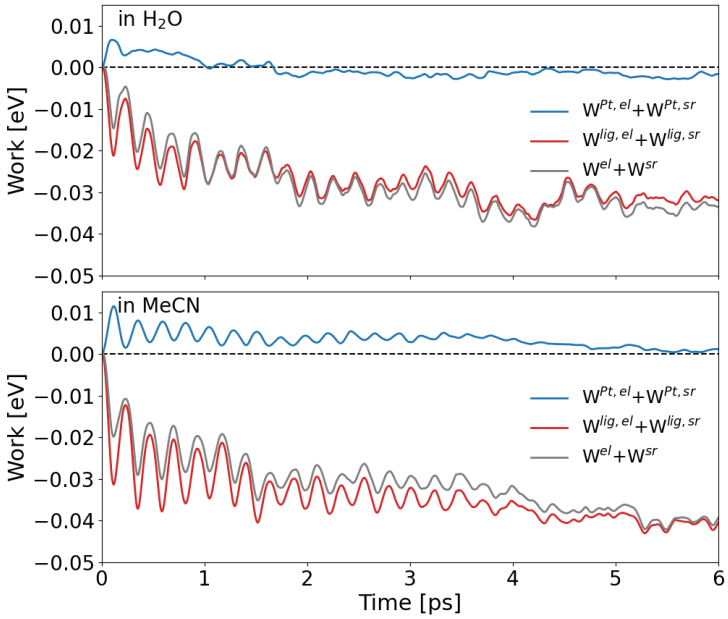


FIG. 7. Total instantaneous average external work on the pinching mode of PtPOP due to electrostatic as well as short-range repulsive and attractive interactions with the solvent (the latter described by a Lennard-Jones potential), and decomposition into contributions of the Pt and ligand atoms, in water (top) and acetonitrile (bottom). Since the external work on the Pt atoms approaches zero by the end of the nonequilibrium dynamics, there is no net direct energy transfer from the Pt atoms to the solvent. Instead, the external work on ligand atoms accounts for nearly all the energy released to the solvent from the pinching mode.

total external work on the Pt atoms arising from interactions with the solvent is initially positive. It then decreases and approaches zero. Thus, there is no net direct energy transfer

from the Pt atoms to the solvent, neither for water nor for acetonitrile. Instead, nearly all the energy transferred to the solvent is accounted for by the total external work of forces on the ligand atoms.

Figure 8 shows the time evolution of the average external work on the Pt and ligand atoms due to electrostatic interactions on the one hand and the short-range repulsive and attractive LJ interactions on the other hand. In water, the work of short-range LJ forces on the Pt

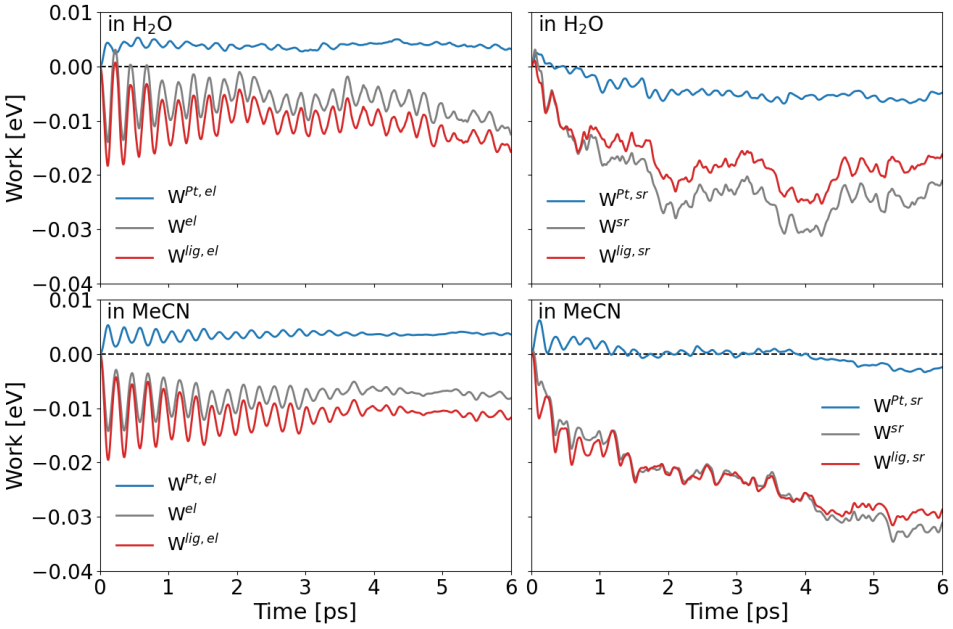


FIG. 8. Instantaneous average external work on the pinching mode of PtPOP due to electrostatic (left) and short-range repulsive and attractive LJ (right) interactions with the solvent, and decomposition into contributions of the Pt and ligand atoms, in water (top) and acetonitrile (bottom). In water, a significant fraction of excess vibrational energy is released to the solvent via direct short-range interactions with the Pt atoms. However, a comparable amount of energy is received by the complex through electrostatic Pt-solvent interactions, so there is no net energy transfer via the Pt atoms (see also Figure 7). In acetonitrile, there is no significant energy transfer to the solvent through direct Pt-solvent interactions.

atoms accounts for a relatively large portion (approximately 23% by the end of the dynamics) of the total excess vibrational energy transferred from the excited complex to the solvent

through short-range interactions. However, since the work done by the electrostatic forces on the Pt atoms is positive and of similar magnitude, these two contributions effectively cancel each other, and there is no net energy transfer directly from the Pt atoms to the solvent. This is consistent with the total instantaneous external work on the Pt atoms being close to zero, as shown in Figure 7. Meanwhile, in acetonitrile, direct short-range LJ interactions between the Pt atoms and the solvent molecules contribute significantly less to the transfer of excess vibrational energy. Overall, both in water and acetonitrile, during the dynamics the work of short-range LJ forces on the ligands accounts for most of the total net energy released to the solvent. Electrostatic interactions with the ligands account for the rest of the energy transfer, with a bigger contribution in water compared to acetonitrile.

The presence of an energy dissipation channel involving direct short-range interactions between the Pt atoms and the solvent in water but not in acetonitrile can be explained by the ability of water molecules to coordinate to the metal atoms which is not the case for acetonitrile (see section III B). The nonequilibrium ensemble created by photoexcitation initially includes configurations where water molecules strongly coordinate to the Pt atoms, exhibiting Pt−H distances below 3 Å, which reflects the ground state equilibrium solvation structure. As shown in section III B, this close coordination is lost after photoexcitation. Therefore, the dissipation of excess vibrational energy from the pinching mode through direct Pt-water interactions is expected to be more efficient during the early stages of photorelaxation. This is supported by Figure 9, which shows that the time scale of the desolvation of water molecules in the first solvation shell is similar to the time scale of the direct energy transfer through short-range LJ Pt-water interactions.

## IV. DISCUSSION

The energy flux approach presented above can be used to identify the pathways of energy relaxation of excited molecules in solution. The method uses the instantaneous atomic forces from nonequilibrium QM/MM molecular dynamics simulations and generalized normal modes obtained from the velocity covariances. Unlike previous methods within this category[35–43], where the entire system has been described using potential energy functions, the simulations presented here involve a description of the electronic structure of the solute using density functional calculations, thereby accounting for the polarization of the electron

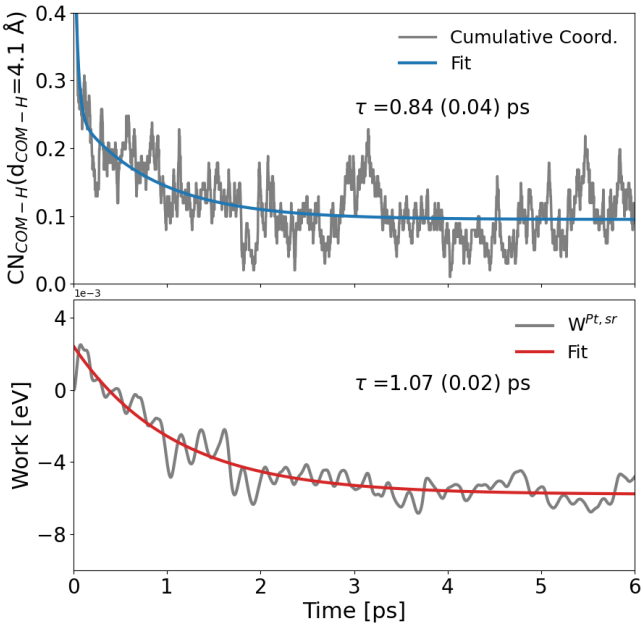


FIG. 9. Instantaneous cumulative coordination number (CN) calculated for distances between the center of mass of PtPOP and the H atoms of water below 4.1 Å (top) and time dependence of the component of the work on the pinching mode of PtPOP due to short-range LJ interactions between the Pt atoms and the solvent. The cumulative coordination number and the work of short-range Pt-water forces are fitted with double and single exponential functions, respectively. The values in parentheses are the standard errors of the fits. The time scales of desolvation and energy transfer via Pt-water interactions are similar, indicating that direct energy transfer from the Pt atoms to the solvent is enabled by a close coordination within the first solvation shell at the beginning of the excited state dynamics.

density of the solute by the environment. While the method has been applied here to analyze the flow of excess vibrational energy from the photoexcited PtPOP complex to a solvent, it can be used to analyze energy fluxes in other energy relaxation processes as well, such as the solvation relaxation following electronic excitation of a solute[69]. Moreover, while the present work has focused on the contributions of the solute atoms to the energy flow, it is straightforward to extend the analysis to the identification of solvent molecules and solvent dynamical modes that accept the excess energy from the solute.

In water, intersystem crossing from the initially excited singlet state to the lowest triplet excited state occurs more slowly than the decay time of photoinduced coherent Pt-Pt oscillations and the decoherence time obtained from the simulations (1.59 ps) agrees very well with experimental values (1.76±0.08 and 1.5±0.5 ps from transient absorption and fluorescence up-conversion measurements[16], respectively). In acetonitrile, however, intersystem crossing has been observed to occur more rapidly than vibrational decoherence, leading to the transfer of coherence from the singlet to the triplet excited state[15]. The coherence decay time in acetonitrile calculated here from nonequilibrium adiabatic molecular dynamics simulations (1.60 ps), which neglect intersystem crossing, is longer than the experimentally deduced singlet state decoherence time (1.1±0.1 ps), but shorter than the decoherence time observed for the lowest triplet state (2.5±0.4 ps)[15]. Thus, intersystem crossing appears to prevent delocalization of vibrational energy. This is further supported by the recent finding that the spin-vibronic couplings driving intersystem crossing are strongest along the pinching mode[27]. The remarkable role of intersystem crossing in prolonging or even generating vibrational coherence by channelling energy along a few specific vibrational modes has been recently proposed for other Pt(II)-Pt(II) complexes as well[10].

The present simulations yield a decay time for the coherent Pt-Pt oscillations in the lowest singlet excited state in water that is in better agreement with experimental values compared to previous QM/MM simulations where decoherence was found to be three times faster than in the experiments[28]. The overestimation of the speed of decoherence in the previous simulations is likely a result of a combination of factors. Firstly, while the old simulations used the same functional (BLYP) as used here, they did not include dispersion interactions. An analysis of the potential of mean force along the Pt-Pt coordinate indicates that BLYP provides a less harmonic potential than BLYP supplemented with D3 dispersion approximation. Secondly, the previous simulations used LJ parameters from the universal force field (UFF)[75] for the short-range repulsive and attractive QM/MM interactions instead of parameters obtained from fitting results of electronic structure calculations, as done in the present work. The solvation shell structure obtained using the UFF parameters involves a stronger transient coordination of water molecules to the Pt atoms of the complex, which is not eliminated upon excitation[28]. As shown here, excess Pt-Pt vibrational energy can be dissipated through the short-range interactions between the Pt atoms and surrounding water molecules. Therefore, a stronger Pt-solvent coordination can lead to a faster vibrational

energy relaxation. Thirdly, the previous simulations included smearing of the occupation numbers to aid convergence of the excited state KS calculations. Such smearing has been shown to cause discontinuities along the potential energy surface when electronic states approach each other in energy[48], as can transiently occur during dynamics in solution, thereby accelerating dephasing. The present simulations use a more robust, direct optimization approach to converge the excited state orbital optimization[48], which does not necessitate of smearing of the occupation numbers, and is therefore not affected by such potential issue. Lastly, in the previous simulations, all solvent molecules in the system, including those closest to the PtPOP molecule, were coupled to the heat bath through a Langevin thermostat, which might have also contributed to accelerating the dephasing of coherent vibrations.

The analysis of the pathways of the flow of excess energy deposited by photoexcitation the pinching mode to the solvent reveals a rather complex interplay between electrostatic and short-range LJ forces. In water, where solvent molecules can transiently coordinate the Pt atoms, energy can be transferred directly from the metal atoms through short-range interactions. However, the electrostatic forces exerted by the solvent act to compress the Pt-Pt distance by performing positive work on the Pt atoms. Thus, the two types of forces have opposing effects of similar magnitude, resulting in no net transfer of energy to the solvent directly from the Pt atoms. Instead, the excess vibrational energy is predominantely dissipated to the solvent through the ligand atoms. This energy transfer occurs primarily through short-range interactions. This is unlike what has been found for the dipolar methyl chloride molecule in water from molecular dynamics simulations with potential energy functions.[42] There, excess vibrational energy was found to be transferred to the solvent mainly through electrostatic interactions.

## V. CONCLUSIONS

Nonequilibrium adiabatic molecular dynamics simulations have been performed to investigate the vibrational decoherence and energy relaxation pathways of the bimetallic PtPOP complex following electronic excitation in liquid water on the one hand and in acetonitrile on the other hand. The simulations use a QM/MM approach and time-independent, orbital-optimized density functional calculations to describe the lowest singlet excited state of the complex. It is found that photoinduced oscillations along the Pt-Pt pinching mode have

a decoherence time of approximately 1.6 ps in both solvents. In water, where intersystem crossing is slower than decoherence, this result is in excellent agreement with experimental values of coherence decay time. In acetonitrile, where intersystem crossing is faster than decoherence, the calculated decoherence time is longer than the experimental value for the lowest singlet excited state (∼1.1 ps), but shorter than that for the lowest triplet excited state (∼2.5 ps). This points to a remarkable role of intersystem crossing in prolonging vibrational coherence by localizing excess vibrational energy. Future work will be aimed at confirming this hypothesis through nonadiabatic QM/MM molecular dynamics simulations including singlet-triplet transitions. These simulations can be performed using well-established trajectory surface hopping methods in conjunction with various electronic structure methods[76], including time-independent, orbital-optimized density functional calculations of excited states[61,77,78], as used here within adiabatic molecular dynamics simulations.

Key pathways of the flow of excess vibrational energy from the solute to the solvent have been identified through a power-work analysis using the QM/MM embedding atomic forces and generalized normal modes obtained from the velocity covariances. The findings show that the energy deposited by photoexcitation in the pinching mode is dissipated to the solvent through the atoms of the ligands, while there is no net energy transfer directly from the Pt atoms. Short-range repulsive and attractive solute-solvent interactions described by a Lennard-Jones potential play a bigger role than electrostatic interactions. Overall, it appears that two key factors drive the exceptionally long-lived and largely solvent-independent vibrational coherence of the PtPOP complex: (1) weak interactions between the Pt atoms and the solvent, facilitated by shielding of the metal atoms by the ligands, and (2) a rigid ligand structure, which makes dissipation of energy through the ligands inefficient.

Future efforts will focus on identifying the solvent molecules and motions that accept the excess energy from the photoexcited PtPOP molecule. It would also be valuable to assess the impact of the solvent polarizability on the vibrational decoherence and energy relaxation pathways. This can be done by using novel QM/MM polarizable embedding models[79–83], which have recently been applied within molecular dynamics simulations in combination with time-independent, orbital-optimized density functional calculations of excited states.[84]

## SUPPLEMENTARY MATERIAL

The Supplementary Material contains a detailed description of the procedure used to thermally equilibrate the ground state trajectories, details on the QM/MM Lennard-Jones parameter optimization, plots of solute-solvent radial distribution functions, and plots of the change in kinetic energy of the pinching mode compared to the change in kinetic energy along other modes.


## ACKNOWLEDGMENTS

This work was funded by the Icelandic Research Fund (grants nos. 217734 and 207014). The authors thank Sergei Egorov and Elvar Ö. Jónsson for stimulating discussions. The calculations were carried out at the Icelandic Research E-Infrastructure (IREI) facility.


## DATA AVAILABILITY STATEMENT

The data that support the findings of this study are available from the corresponding author upon reasonable request.

### Appendix A: Power from total normal mode energy

Here, for simplicity the time dependence is omitted from all equations. Following Ref. 39, the energy of the solute is expressed using the generalized normal modes as a sum of harmonic potentials and a coupling term, $E_{\mathrm{c}}$, arising from anharmonicities and nonlinear couplings between the modes:

$$E_{\mathrm{QM}} = \frac{1}{2}\sum_{i}^{3N} \omega_i^2 Q_i^2 + E_{\mathrm{c}} \tag{A1}$$

where $\omega_i$ is the vibrational frequency of mode $i$. Accordingly, the force along a generalized normal mode is partitioned as follows:

$$\tilde{F}_i = \mathbf{L}_i^{\dagger} \cdot \left(\mathbf{F}'_{\mathrm{QM}} + \mathbf{F}'_{\mathrm{el}} + \mathbf{F}'_{\mathrm{es}}\right) = -\omega_i^2 Q_i + \tilde{F}_i^{\mathrm{c}} + \mathbf{L}_i^{\dagger} \cdot \left(\mathbf{F}'_{\mathrm{el}} + \mathbf{F}'_{\mathrm{es}}\right) \tag{A2}$$

where $\mathbf{F}'$ are vectors of mass-weighted atomic force components, $\mathbf{L}_i$ is a column vector of the transformation matrix defined in eqs 7 and 8, and $\tilde{F}_i^{\mathrm{c}} = \mathbf{L}_i^{\dagger} \cdot \mathbf{F}'_{\mathrm{QM}} + \omega_i^2 Q_i$ accounts for

couplings between the modes. The time derivative of the total harmonic energy for each mode, $T_i + E_i = (\dot{Q}_i^2 + \omega_i^2 Q_i^2)/2$, is then:

$$\begin{aligned}\frac{\mathrm{d}}{\mathrm{d}t}\left(T_i + E_i\right) &= \dot{Q}_i\left[-\omega_i^2 Q_i + \tilde{F}_i^{\mathrm{c}} + \mathbf{L}_i^{\dagger}\cdot\left(\mathbf{F}'_{\mathrm{el}} + \mathbf{F}'_{\mathrm{es}}\right) + \omega_i^2 Q_i\right] \\ &= \dot{Q}_i\tilde{F}_i^{\mathrm{c}} + \dot{Q}_i\mathbf{L}_i^{\dagger}\cdot\left(\mathbf{F}'_{\mathrm{el}} + \mathbf{F}'_{\mathrm{es}}\right) \\ &= P_i^{\mathrm{c}} + P_i^{\mathrm{el}} + P_i^{\mathrm{sr}}\end{aligned} \tag{A3}$$

The last two terms in eq A3, $P_i^{\mathrm{el}}$ and $P_i^{\mathrm{sr}}$, represent the power of external electrostatic and short-range forces on a normal mode, respectively. Time integration of these terms gives the work done by the solvent on the vibrational coordinate via electrostatic and short-rage forces, $W_i^{\mathrm{el}}$ and $W_i^{\mathrm{sr}}$, which correspond to the terms in eq 16 derived from considering the time evolution of the kinetic energy only. $P_i^{\mathrm{c}}$ represents the power associated with intermode couplings. An analysis of this term would provide information on the energy flux between vibrational modes, i.e. the intramolecular vibrational redistribution. However, a separation into pairwise contributions involving energy exchange between pairs of modes is not straightforward[39].

## REFERENCES


[1]A. H. Zewail, "Femtochemistry: Atomic-Scale Dynamics of the Chemical Bond," The Journal of Physical Chemistry A **104**, 5660–5694 (2000).

[2]T. I. Sølling and K. B. Møller, "Perspective: Preservation of coherence in photophysical processes," Structural Dynamics **5**, 060901 (2018).

[3]E. Romero, V. I. Novoderezhkin, and R. Van Grondelle, "Quantum design of photosynthesis for bio-inspired solar-energy conversion," Nature **543**, 355–365 (2017).

[4]D. Abramavicius and L. Valkunas, "Role of coherent vibrations in energy transfer and conversion in photosynthetic pigment-protein complexes," Photosynthesis Research **127**, 33–47 (2016).

[5]A. Chenu and G. D. Scholes, "Coherence in energy transfer and photosynthesis," Annual Review of Physical Chemistry **66**, 69–96 (2015).

[6]F. D. Fuller, J. Pan, A. Gelzinis, V. Butkus, S. S. Senlik, D. E. Wilcox, C. F. Yocum, L. Valkunas, D. Abramavicius, and J. P. Ogilvie, "Vibronic coherence in oxygenic photosynthesis," Nature Chemistry **6**, 706–711 (2014).

[7]T. Yan and Q. Wan, "Vibrational Coherence in the Metal–Metal-Bonded Excited State of Pt(II) Complexes," Inorganics **11**, 441 (2023).

[8]M. Chaaban, C. Zhou, H. Lin, B. Chyi, and B. Ma, "Platinum(II) binuclear complexes: molecular structures, photophysical properties, and applications," Journal of Materials Chemistry C **7**, 5910–5924 (2019).

[9]H. Gray, S. Záliš, and A. Vlček, "Electronic structures and photophysics of d8-d8 complexes," Coordination Chemistry Reviews **345** (2017).

[10]S. Rafiq, N. Weingartz, S. Kromer, F. N. Castellano, and L. X. Chen, "Spin-Vibronic Coherence Drives Singlet-Triplet Conversion," Nature **620**, 776–781 (2023).

[11]"Revealing Excited State Trajectories on Potential Energy Surfaces with Atomic Resolution in Real Time," Angewandte Chemie **62**, e202304615 (2023).

[12]T. W. Kim, P. Kim, A. W. Mills, A. Chakraborty, S. Kromer, A. J. Valentine, F. N. Castellano, X. Li, and L. X. Chen, "Ligand-Structure-Dependent Coherent Vibrational Wavepacket Dynamics in Pyrazolate-Bridged Pt(II) Dimers," Journal of Physical Chemistry C **126**, 11487–11497 (2022).

[13]P. Kim, A. J. Valentine, S. Roy, A. W. Mills, A. Chakraborty, F. N. Castellano, X. Li, and L. X. Chen, "Ultrafast Excited-State Dynamics of Photoluminescent Pt(II) Dimers Probed by a Coherent Vibrational Wavepacket," Journal of Physical Chemistry Letters **12**, 6794–6803 (2021).

[14]K. Haldrup, G. Levi, E. Biasin, P. Vester, M. G. Laursen, F. Beyer, K. S. Kjær, T. Brandt Van Driel, T. Harlang, A. O. Dohn, R. J. Hartsock, S. Nelson, J. M. Glownia, H. T. Lemke, M. Christensen, K. J. Gaffney, N. E. Henriksen, K. B. Møller, and M. M. Nielsen, "Ultrafast X-Ray Scattering Measurements of Coherent Structural Dynamics on the Ground-State Potential Energy Surface of a Diplatinum Molecule," Physical Review Letters **122**, 63001 (2019).

[15]R. Monni, G. Capano, G. Auböck, H. B. Gray, A. Vlček, I. Tavernelli, and M. Chergui, "Vibrational coherence transfer in the ultrafast intersystem crossing of a diplatinum complex in solution," Proceedings of the National Academy of Sciences **115**, E6396–E6403 (2018).

[16]R. M. Van Der Veen, A. Cannizzo, F. V. Mourik, A. Vlček, and M. Chergui, "Vibrational Relaxation and Intersystem Crossing of Binuclear Metal Complexes in Solution," J. Am. Chem. Soc. **133**, 305–315 (2011).

[17]E. Biasin, T. B. van Driel, G. Levi, M. G. Laursen, A. O. Dohn, A. Moltke, P. Vester, F. B. K. Hansen, K. S. Kjaer, T. Harlang, R. Hartsock, M. Christensen, K. J. Gaffney, N. E. Henriksen, K. B. Møller, K. Haldrup, and M. M. Nielsen, "Anisotropy enhanced X-ray scattering from solvated transition metal complexes research papers," Journal of Synchrotron Radiation **25**, 306–315 (2018).

[18]R. Monni, G. Auböck, D. Kinschel, K. M. Aziz-Lange, H. B. Gray, A. Vlček, and M. Chergui, "Conservation of vibrational coherence in ultrafast electronic relaxation: The case of diplatinum complexes in solution," Chemical Physics Letters **683**, 112–120 (2017), Ahmed Zewail (1946-2016) Commemoration Issue of Chemical Physics Letters.

[19]R. M. Van Der Veen, C. J. Milne, A. E. Nahhas, F. A. Lima, V. T. Pham, J. Best, J. A. Weinstein, C. N. Borca, R. Abela, C. Bressler, and M. Chergui, "Structural determination of a photochemically active diplatinum molecule by time-resolved EXAFS spectroscopy," Angewandte Chemie - International Edition **48**, 2711–2714 (2009).

[20]M. Christensen, K. Haldrup, K. Bechgaard, R. Feidenhans, Q. Kong, M. Cammarata, M. L. Russo, M. Wulff, N. Harrit, M. M. Nielsen, Q. Kong, M. Cammarata, M. L. Russo, and M. Wulff, "Time-Resolved X-ray Scattering of an Electronically Excited State in Solution . Structure of the A State of Tetrakis-µ-pyrophosphitodiplatinate (II)," J. Am. Chem. Soc **131**, 502–508 (2008).

[21]C. D. Kim, S. Pillet, G. Wu, W. K. Fullagar, and P. Coppens, "Excited-state structure by time-resolved X-ray diffraction," Acta Crystallographica Section A: Foundations of Crystallography **58**, 133–137 (2002).

[22]D. J. Thiel, P. Livins, E. A. Stern, and A. Lewis, "Microsecond-resolved XAFS of the triplet excited state of Pt2(P2O5H2)4 4-," Nature **362**, 40–43 (1993).

[23]T. Ikeyama, S. Yamamoto, and T. Azumi, "Vibrational analysis of sublevel phosphorescence spectra of potassium tetrakis($\mu$-diphosphonato)diplatinate(II): mechanism of radiative transition for the electronically forbidden A1u spectrum," The Journal of Physical Chemistry **92**, 6899 (1988).

[24]S. F. Rice and H. B. Gray, "Electronic Absorption and Emission Spectra of Binuclear Platinum(II) Complexes. Characterization of the Lowest Singlet and Triplet Excited States of $Pt2(H_2P_2O_5)_4{}^{4-}$," J. Am. Chem. Soc **105**, 4571–4575 (1983).

[25]W. A. Fordyce, J. G. Brummer, and G. A. Crosby, "Electronic Spectroscopy of a Diplatinum(II) Octaphosphite Complex," J. Am. Chem. Soc. **103**, 7061–7064 (1981).

[26]J. Sadler and M. R. Sanderson, "A Novel Di-platinum(r1) Octaphosphite Complex showing Metal-Metal Bonding and Intense Luminescence; a Potential Probe for Basic Proteins. X-Ray Crystal and Molecular Structure," Journal of the Chemical Society, Chemical Communications , 13–15 (1980).

[27]P. Karak, K. Ruud, and S. Chakrabarti, "Demystifying the Origin of Vibrational Coherence Transfer between the S1 and T1 States of the Pt-pop Complex," Journal of Physical Chemistry Letters **12**, 9768–9773 (2021).

[28]G. Levi, M. Pápai, N. E. Henriksen, A. O. Dohn, and K. B. Møller, "Solution structure and ultrafast vibrational relaxation of the ptpop complex revealed by ΔSCF-QM/MM direct dynamics simulations," The Journal of Physical Chemistry C **122**, 7100–7119 (2018).

[29]S. Záliš, Y.-C. Lam, H. B. Gray, and A. Vlček, "Spin–Orbit TDDFT Electronic Structure of Diplatinum(II,II) Complexes," Inorganic Chemistry **54**, 3491–3500 (2015).

[30]Q. Kong, K. S. Kjaer, K. Haldrup, S. P. a. Sauer, T. B. Van Driel, M. Christensen, M. M. Nielsen, and M. Wulff, "Theoretical study of the triplet excited state of PtPOP and the exciplexes M-PtPOP (M = Tl, Ag) in solution and comparison with ultrafast X-ray scattering results," Chemical Physics **393**, 117–122 (2012).

[31]T. J. Penfold, B. F. E. Curchod, I. Tavernelli, R. Abela, U. Rothlisberger, and M. Chergui, "Simulations of X-ray absorption spectra: the effect of the solvent," Physical Chemistry Chemical Physics **14**, 9444 (2012).

[32]S. R. Stoyanov, J. M. Villegas, and D. P. Rillema, "Spectroscopic properties of [Pt 2($\mu$-P 2O 5H 2) 4]: 4- a time-dependent density functional theory and conductor-like polarizable continuum model investigation," Journal of Physical Chemistry B **108**, 12175–12180 (2004).

[33]I. V. Novozhilova, A. V. Volkov, and P. Coppens, "Theoretical analysis of the triplet excited state of the [Pt2(H2P2O5)4]4- ion and comparison with time-resolved X-ray and spectroscopic results." Journal of the American Chemical Society **125**, 1079–1087 (2003).

[34]G. I. Gellene and D. M. Roundhill, "Computational Studies on the Isomeric Structures in the Pyrophosphito Bridged Diplatinum (II) Complex , Platinum Pop," Journal of Physical Chemistry A **106**, 7617–7620 (2002).

[35]A. Jurado Romero, C. Calero, E. L. Sibert, and R. Rey, "High energy vibrational excitations of nitromethane in liquid water," Journal of Chemical Physics **158** (2023).

[36]R. Rey and J. T. Hynes, "Tracking energy transfer from excited to accepting modes: application to water bend vibrational relaxation," Physical Chemistry Chemical Physics **14**, 6332–42 (2012).

[37]R. Rey, F. Ingrosso, T. Elsaesser, and J. T. Hynes, "Pathways for $H_2O$ bend vibrational relaxation in liquid water," Journal of Physical Chemistry A **113**, 8949 (2009).

[38]A. Kandratsenka, J. Schroeder, D. Schwarzer, and V. S. Vikhrenko, "Nonequilibrium molecular dynamics simulations of vibrational energy relaxation of HOD in D2O," Journal of Chemical Physics **130** (2009).

[39]V. S. Vikhrenko, C. Heidelbach, D. Schwarzer, V. B. Nemtsov, and J. Schroeder, "Molecular dynamics simulation of vibrational energy relaxation of highly excited molecules in fluids. I. General considerations," Journal of Chemical Physics **110**, 5273–5285 (1999).

[40]C. Heidelbach, V. S. Vikhrenko, D. Schwarzer, and J. Schroeder, "Molecular dynamics simulation of vibrational relaxation of highly excited molecules in fluids. II. Nonequilibrium simulation of azulene in CO2 and Xe," Journal of Chemical Physics **110**, 5286–5299 (1999).

[41]C. Heidelbach, J. Schroeder, D. Schwarzer, and V. S. Vikhrenko, "Mode specificity of vibrational energy relaxation of azulene in CO2 at low and high density," Chemical Physics Letters **291**, 333–340 (1998).

[42]R. M. Whitnell, K. R. Wilson, and J. T. Hynes, "Vibrational relaxation of a dipolar molecule in water," The Journal of Chemical Physics **96**, 5354–5369 (1992).

[43]I. Ohmine, "Energy dissipation mechanism of the optically excited molecules in solvents: A trajectory study for a photoisomerization process of the $\pi$-conjugated molecule in Ar and water," The Journal of Chemical Physics **85**, 3342–3358 (1986).

[44]A. Strachan, "Normal modes and frequencies from covariances in molecular dynamics or monte carlo simulations," Journal of Chemical Physics **120**, 1–4 (2004).

[45]E. Selenius, A. E. Sigurdarson, Y. L. A. Schmerwitz, and G. Levi, "Orbital-Optimized Versus Time-Dependent Density Functional Calculations of Intramolecular Charge Transfer Excited States," Journal of Chemical Theory and Computation **20**, 3809–3822 (2024), 2311.01604.

[46]Y. L. A. Schmerwitz, G. Levi, and H. Jónsson, "Calculations of Excited Electronic States by Converging on Saddle Points Using Generalized Mode Following," Journal of Chemical Theory and Computation **19**, 3634–3651 (2023), 2302.05912.

[47]D. Hait and M. Head-Gordon, "Orbital Optimized Density Functional Theory for Electronic Excited States," Journal of Physical Chemistry Letters **12**, 4517–4529 (2021), arXiv:2103.04573.

[48]G. Levi, A. V. Ivanov, and H. Jónsson, "Variational Density Functional Calculations of Excited States via Direct Optimization," Journal of Chemical Theory and Computation **16**, 6968–6982 (2020), 2006.15922.

[49]A. O. Dohn, "Multiscale electrostatic embedding simulations for modeling structure and dynamics of molecules in solution: A tutorial review," International Journal of Quantum Chemistry **120**, 26343 (2020).

[50]A. O. Dohn, E. Ö. Jónsson, G. Levi, J. J. Mortensen, O. Lopez-Acevedo, K. S. Thygesen, K. W. Jacobsen, J. Ulstrup, N. E. Henriksen, K. B. Møller, and H. Jónsson, "Grid-Based Projector Augmented Wave (GPAW) Implementation of Quantum Mechanics/Molecular Mechanics (QM/MM) Electrostatic Embedding and Application to a Solvated Diplatinum Complex," J. Chem. Theory Comput. **13**, 6010–6022 (2017).

[51]M. J. Field, P. A. Bash, and M. Karplus, "A combined quantum mechanical and molecular mechanical potential for molecular dynamics simulations," Journal of Computational Chemistry **11**, 700–733 (1990).

[52]W. Kohn and L. J. Sham, "Self-consistent equations including exchange and correlation effects," Phys. Rev. **140**, 1133–1138 (1965).

[53]P. Hohenberg and W. Kohn, "Inhomogeneous electron gas," Phys. Rev. **136**, B864 (1964).

[54]N. Rega, "Vibrational analysis beyond the harmonic regime from Ab-initio molecular dynamics," Theoretical Chemistry Accounts **116**, 347–354 (2006).

[55]C. Lee, W. Yang, and R. G. Parr, "Development of the colle-salvetti correlation-energy formula into a functional of the electron density," Phys. Rev. B **37**, 785–789 (1988).

[56]S. Grimme, J. Antony, S. Ehrlich, and H. Krieg, "A consistent and accurate ab initio parametrization of density functional dispersion correction (DFT-D) for the 94 elements H-Pu," Journal of Chemical Physics **132**, 154104 (2010).

[57]S. Grimme, S. Ehrlich, and L. Goerigk, "Effect of the damping function in dispersion corrected density functional theory," Journal of Computational Chemistry **32**, 1456–1465 (2011).

[58]P. E. Blöchl, "Projector augmented-wave method," Physical Review B **50**, 17953–17979 (1994).

[59]P. E. Blöchl, C. J. Först, and J. Schimpl, "Projector augmented wave method:ab initio molecular dynamics with full wave functions," Bulletin of Materials Science **26**, 33–41 (2003).

[60]A. H. Larsen, M. Vanin, J. J. Mortensen, K. S. Thygesen, and K. W. Jacobsen, "Localized atomic basis set in the projector augmented wave method," Physical Review B - Condensed Matter and Materials Physics **80**, 1–10 (2009).

[61]M. Mališ and S. Luber, "Trajectory Surface Hopping Nonadiabatic Molecular Dynamics with Kohn-Sham ΔSCF for Condensed-Phase Systems," J. Chem. Theory Comput **16**, 4071–4086 (2020).

[62]B. Himmetoglu, A. Marchenko, I. Dabo, and M. Cococcioni, "Role of electronic localization in the phosphorescence of iridium sensitizing dyes," Journal of Chemical Physics **137**, 154309 (2012).

[63]G. Levi, A. V. Ivanov, and H. Jónsson, "Variational calculations of excited states via direct optimization of the orbitals in dft," Faraday Discuss. **224**, 448–466 (2020).

[64]G. M. Barca, A. T. Gilbert, and P. M. Gill, "Simple Models for Difficult Electronic Excitations," Journal of Chemical Theory and Computation **14**, 1501–1509 (2018).

[65]W. L. Jorgensen, J. Chandrasekhar, J. D. Madura, R. W. Impey, and M. L. Klein, "Comparison of simple potential functions for simulating liquid water," The Journal of Chemical Physics **79**, 926–935 (1983).

[66]E. Guàrdia, R. Pinzón, J. Casulleras, M. Orozco, and F. J. Luque, "Comparison of Different Three-site Interaction Potentials for Liquid Acetonitrile," Molecular Simulation **26**, 287–306 (2001).

[67]H. C. Andersen, "Rattle: A "velocity" version of the shake algorithm for molecular dynamics calculations," Journal of Computational Physics **52**, 24–34 (1983).

[68]G. Ciccotti, M. Ferrario, and J.-P. Ryckaert, "Molecular dynamics of rigid systems in cartesian coordinates A general formulation," Molecular Physics **47**, 1253–1264 (1982).

[69]R. Rey and J. T. Hynes, "Solvation Dynamics in Liquid Water. 1. Ultrafast Energy Fluxes," The Journal of Physical Chemistry B **119**, 7558–7570 (2015).

[70]B. J. Gertner, R. M. Whitnell, K. R. Wilson, and J. T. Hynes, "Activation to the Transition State: Reactant and Solvent Energy Flow for a Model SN2 Reaction in Water," Journal of the American Chemical Society **113**, 74–87 (1991).

[71]A. H. Larsen, J. J. Mortensen, J. Blomqvist, I. E. Castelli, R. Christensen, M. Dułak, J. Friis, M. N. Groves, B. Hammer, C. Hargus, E. D. Hermes, P. C. Jennings, P. B. Jensen, J. Kermode, J. R. Kitchin, E. L. Kolsbjerg, J. Kubal, K. Kaasbjerg, S. Lysgaard, J. B. Maronsson, T. Maxson, T. Olsen, L. Pastewka, A. Peterson, C. Rostgaard, J. Schiøtz, O. Schütt, M. Strange, K. S. Thygesen, T. Vegge, L. Vilhelmsen, M. Walter, Z. Zeng, and K. W. Jacobsen, "The atomic simulation environment—a python library for working with atoms," Journal of Physics: Condensed Matter **29**, 273002 (2017).

[72]J. J. Mortensen, A. H. Larsen, M. Kuisma, A. V. Ivanov, A. Taghizadeh, A. Peterson, A. Haldar, A. O. Dohn, C. Schäfer, E. Ö. Jónsson, E. D. Hermes, F. A. Nilsson, G. Kastlunger, G. Levi, H. Jónsson, H. Häkkinen, J. Fojt, J. Kangsabanik, J. Sødequist, J. Lehtomäki, J. Heske, J. Enkovaara, K. T. Winther, M. Dulak, M. M. Melander, M. Ovesen, M. Louhivuori, M. Walter, M. Gjerding, O. Lopez-Acevedo, P. Erhart, R. Warmbier, R. Würdemann, S. Kaappa, S. Latini, T. M. Boland, T. Bligaard, T. Skovhus, T. Susi, T. Maxson, T. Rossi, X. Chen, Y. L. A. Schmerwitz, J. Schiøtz, T. Olsen, K. W. Jacobsen, and K. S. Thygesen, "GPAW: open Python package for electronic-structure calculations," Journal of Chemical Physics **160**, 092503 (2024).

[73]T. B. Van Driel, K. S. Kjaer, R. W. Hartsock, A. O. Dohn, T. Harlang, M. Chollet, M. Christensen, W. Gawelda, N. E. Henriksen, J. G. Kim, K. Haldrup, K. H. Kim, H. Ihee, J. Kim, H. Lemke, Z. Sun, V. Sundstroöm, W. Zhang, D. Zhu, K. B. MØller, M. M. Nielsen, and K. J. Gaffney, "Atomistic characterization of the active-site solvation dynamics of a model photocatalyst," Nature Communications **7**, 13678 (2016).

[74]A. O. Dohn, E. Ö. Jónsson, K. S. Kjær, T. B. Van Driel, M. M. Nielsen, K. W. Jacobsen, N. E. Henriksen, and K. B. Møller, "Direct dynamics studies of a binuclear metal complex in solution: The interplay between vibrational relaxation, coherence, and solvent effects," Journal of Physical Chemistry Letters **5**, 2414–2418 (2014).

[75]A. K. Rappe, C. J. Casewit, K. S. Colwell, W. A. I. Goddard, and W. M. Skiff, "UFF, a full periodic table force field for molecular mechanics and molecular dynamics simulations," Journal of the American Chemical Society **114**, 10024–10035 (1992).

[76]S. Mai, P. Marquetand, and L. González, "Nonadiabatic dynamics: The sharc approach," WIREs Comput. Mol. Sci. **8**, e1370 (2018).

[77]E. Vandaele, M. Mališ, and S. Luber, "The ΔSCF method for non-adiabatic dynamics of systems in the liquid phase," J. Chem. Phys **156**, 130901 (2022).

[78]M. Mališ, E. Vandaele, and S. Luber, "Spin-Orbit Couplings for Nonadiabatic Molecular Dynamics at the ΔSCF Level," Journal of Chemical Theory and Computation **18**, 4082–4094 (2022).

[79]M. Nottoli, L. Cupellini, F. Lipparini, G. Granucci, and B. Mennucci, "Multiscale Models for Light-Driven Processes," Annual Review of Physical Chemistry **72**, 489–513 (2021).

[80]M. Bondanza, M. Nottoli, L. Cupellini, F. Lipparini, and B. Mennucci, "Polarizable embedding QM/MM: The future gold standard for complex (bio)systems?" Physical Chemistry Chemical Physics **22**, 14433–14448 (2020).

[81]E. Ö. Jónsson, A. O. Dohn, and H. Jónsson, "Polarizable Embedding with a Transferable H2O Potential Function I: Formulation and Tests on Dimer," Journal of Chemical Theory and Computation **15**, 6562–6577 (2019).

[82]A. O. Dohn, E. Ö. Jónsson, and H. Jónsson, "Polarizable Embedding with a Transferable H2O Potential Function II: Application to (H2O)n Clusters and Liquid Water," Journal of Chemical Theory and Computation **15**, 6578–6587 (2019).

[83]J. W. Ponder, C. Wu, P. Ren, V. S. Pande, J. D. Chodera, M. J. Schnieders, I. Haque, D. L. Mobley, D. S. Lambrecht, R. A. J. DiStasio, M. Head-Gordon, G. N. I. Clark, M. E. Johnson, and T. Head-Gordon, "Current status of the amoeba polarizable force field," The Journal of Physical Chemistry B **114**, 2549–2564 (2010).

[84]P. Mazzeo, S. Hashem, F. Lipparini, L. Cupellini, and B. Mennucci, "Fast Method for Excited-State Dynamics in Complex Systems and Its Application to the Photoactivation of a Blue Light Using Flavin Photoreceptor," Journal of Physical Chemistry Letters **14**, 1222–1229 (2023).

# Paper II

## Characterization of Deformational Isomerization Potential and Interconversion Dynamics with Ultrafast X-ray Solution Scattering

Natalia E. Powers-Riggs, Benedikt O. Birgisson, Sumana L. Raj, Elisa Biasin, Philipp Lenzen, Diana Bregenholt Zederkof, Morten Haubro, Dagrún K. V. Tveiten, Robert W. Hartsock, Tim B. van Driel, Kristjan Kunnus, Matthieu Chollet, Joseph S. Robinson, Silke Nelson, Ruaridh Forbes, Kristoffer Haldrup, Kasper S. Pedersen, Gianluca Levi, Asmus Ougaard Dohn, Hannes Jónsson, Klaus Braagaard Moller, Adi Natan,* Martin Meedom Nielsen,* and Kelly J. Gaffney*

*J. Am. Chem. Soc. 2024, 146, 20, 13962–13973*

JACS
JOURNAL OF THE AMERICAN CHEMICAL SOCIETY
pubs.acs.org/JACS
Article

# Characterization of Deformational Isomerization Potential and Interconversion Dynamics with Ultrafast X-ray Solution Scattering

Natalia E. Powers-Riggs, Benedikt O. Birgisson, Sumana L. Raj, Elisa Biasin, Philipp Lenzen, Diana Bregenholt Zederkof, Morten Haubro, Dagrún K. V. Tveiten, Robert W. Hartsock, Tim B. van Driel, Kristjan Kunnus, Matthieu Chollet, Joseph S. Robinson, Silke Nelson, Ruaridh Forbes, Kristoffer Haldrup, Kasper S. Pedersen, Gianluca Levi, Asmus Ougaard Dohn, Hannes Jónsson, Klaus Braagaard Møller, Adi Natan,* Martin Meedom Nielsen,* and Kelly J. Gaffney*

Cite This: J. Am. Chem. Soc. 2024, 146, 13962−13973



**ABSTRACT:** Dimeric complexes composed of $d^8$ square planar metal centers and rigid bridging ligands provide model systems to understand the interplay between attractive dispersion forces and steric strain in order to assist the development of reliable methods to model metal dimer complexes more broadly. $[Ir_2\ (dimen)_4]^{2+}$ (dimen = *para*-diisocyanomenthane) presents a unique case study for such phenomena, as distortions of the optimal structure of a ligand with limited conformational flexibility counteract the attractive dispersive forces from the metal and ligand to yield a complex with two ground state deformational isomers. Here, we use ultrafast X-ray solution scattering (XSS) and optical transient absorption spectroscopy (OTAS) to reveal the nature of the equilibrium distribution and the exchange rate between the deformational isomers. The two ground state isomers have spectrally distinct electronic excitations that enable the selective excitation of one isomer or the other using a femtosecond duration pulse of visible light. We then track the dynamics of the nonequilibrium depletion of the electronic ground state population—often termed the ground state hole—with ultrafast XSS and OTAS, revealing a restoration of the ground state equilibrium in 2.3 ps. This combined experimental and theoretical study provides a critical test of various density functional approximations in the description of bridged $d^8$−$d^8$ metal complexes. The results show that density functional theory calculations can reproduce the primary experimental observations if dispersion interactions are added, and a hybrid functional, which includes exact exchange, is used.

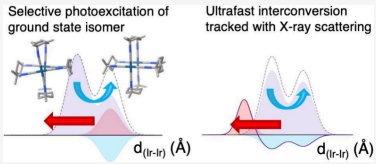




## INTRODUCTION

The close interplay between metal−metal distance and optical and reactive properties[1] of $d^8$−$d^8$ metal complexes yield a configurable class of molecules with potential applications in sensing, light-emitting devices,[2] and catalysis.[3] According to the molecular orbital configuration shown schematically in Figure 1, these square planar $d^8$ subunits are metal−metal nonbonding: the HOMO $d_{z^2}$ orbitals in the monomer are doubly occupied, leading to fully occupied $d_{z^2}\sigma$ and $d_{z^2}\sigma^*$ orbitals in a dimeric complex.[1] Nonetheless, many $d^8$ monomers self-assemble into oligomers[4,5] and polymers, raising the question of what controls the monomer−monomer interactions. For oligomers with aromatic ligands, quantum chemical calculations indicate the polarizability of the ligands can be critical to the chemical driving force for dimer formation.[6] However, the formation of oligomers in complexes with nonaromatic ligands[4] demonstrates the importance of additional noncovalent bonding interactions, such as the dispersion forces between the metal atoms, or between the metal atoms and surrounding ligands. This poses a challenge when modeling the structure of such complexes.

Dimeric complexes of the type $[M_2\ (dimen)_4]^{2+}$ (MDimen, where dimen = *para*-diisocyano-menthane, and M = Rh or Ir, see Figure 1) present a particularly interesting model to study these nonbonding interactions. Each dimen bridging ligand lacks the polarizability—and by extension attractive dispersion forces and tendency to aggregate—of an aromatic linker, and the rigid cyclohexane unit of the ligand also presents a steric constraint that limits the conformational flexibility. This constraint, in conjunction to the square planar geometry typical of M−isocyano bonding, leads to a spacing of 4−5 Å between metals, compared to the ∼3.3 Å metal−metal distance ($d_{M\text{-}M}$) displayed in complexes with nonrigid alkyl ligands possessing the same number of spacer carbon atoms.[7] Early analysis of the crystal structure of dimeric rhodium and iridium

Received: February 6, 2024
Revised: April 30, 2024
Accepted: May 2, 2024
Published: May 10, 2024





https://doi.org/10.1021/jacs.4c00817
J. Am. Chem. Soc. 2024, 146, 13962−13973

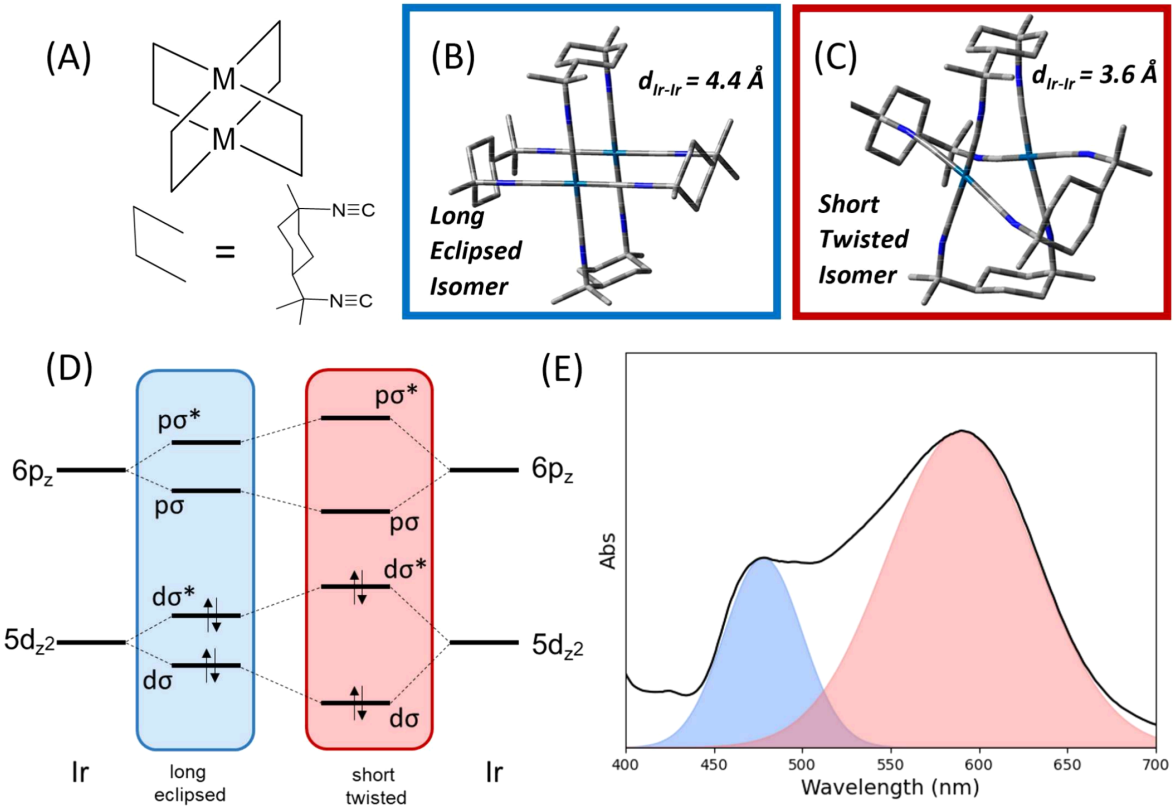


**Figure 1.** (A) Schematic molecular structure of a MDimen complex, with detailed depiction of the dimen ligand. Visualization of the two deformational isomers of IrDimen, the long and eclipsed isomer (B), and the short and twisted isomer (C). (D) Molecular orbitals involved in the lowest energy electronic transitions in the IrDimen complex. (E) UV−vis absorption spectra of IrDimen, with shaded regions depicting the bands associated with transitions arising from the populations of different isomers.

complexes indicates that the type of metal center also has an influence on the equilibrium geometry, since across several isocyanide bridged ligands, the equilibrium Ir−Ir distance (3.6−4.4 Å) is consistently shorter than the equilibrium Rh−Rh distance (3.9−4.5 Å).[8]

These modifications in metal−metal distance generate significant changes in the UV−visible absorption spectrum. In $d^8$−$d^8$ metal complexes, the lowest energy electronic transition results from excitation of the HOMO antibonding $d_{z^2}\sigma^*$ orbital to the LUMO bonding $p_z\sigma$ orbital (see molecular orbital diagram shown in Figure 1d). This transition significantly red-shifts as the metal−metal distance shortens, as antibonding (HOMO) and bonding (LUMO) orbitals become destabilized and stabilized, respectively.[1] This correlation between the structure and absorption properties provides a means for gaining preliminary information on the equilibrium structure in solution. Both rhodium and iridium dimen complexes can display a range of M−M distances in the solid state upon variation of the counterions, but their distinct solution-phase spectra indicate different equilibrium geometries. In solution, the UV−visible absorption spectrum of RhDimen shows a single broad, asymmetric band centered at 423 nm,[9,10] similar to the absorption spectrum of the RhDimen complex with a 4.5 Å Rh−Rh distance. This single, broad peak corresponding to a structure with a long M−M distance indicates the presence of a broad distribution of conformations around a single equilibrium isomer in solution and that the steric hindrance from the dimen ligands dominates over attractive forces such as dispersion interactions. IrDimen exhibits two peaks in the solution phase UV−visible absorption spectrum, at 480 and 585 nm, suggesting the presence of populations of distinct deformational isomers (Figure 1E). Correlation between the crystal structures and the UV−visible spectrum identifies the peak at 480 nm as arising from an isomer with a long Ir−Ir distance and an eclipsed ligand structure, hereafter the "long/eclipsed isomer" (Figure 1B), while the peak at 585 nm is assigned to a shorter Ir−Ir distance and a twisted ligand structure, or "short/twisted isomer" (Figure 1C).[8] Variable temperature absorption revealed the two peaks are in equilibrium, and can undergo temperature dependent interconversion, though the lack of an isosbestic point in the temperature dependent spectra indicates thermally populated Franck−Condon active vibrations influence the absorption spectrum.[11]

Understanding the forces at play is key to developing design principles for $d^8$−$d^8$ dimer complexes with specific electronic properties. The distinct equilibrium isomers of IrDimen create an opportunity to further understand the interplay among different kinds of intramolecular interactions. Investigating the dynamics of interconversion provides further insight into the relative free energy levels and barrier heights between equilibrium isomers. However, determination of the equili-


https://doi.org/10.1021/jacs.4c00817
J. Am. Chem. Soc. 2024, 146, 13962−13973

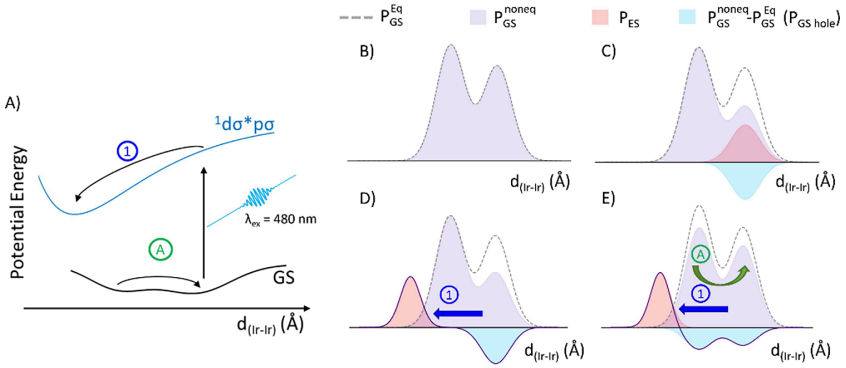


**Figure 2.** Schematic depictions of the hole burning process and the following nonequilibrium dynamics. (A) Ground state and excited state potential energy surfaces of IrDimen. Following excitation, the excited state nonequilibrium population of structures undergoes relaxation to the energetic minimum of the respective potential energy surface (process (1)). The ground state concurrently undergoes process (A), where the equilibrium between the population of the two isomers is reestablished. The population dynamics are represented in (B)-(E), as a function of Ir−Ir distance. The ground state population at equilibrium is represented by the gray dashed line, and the nonequilibrium ground state population ($P_{GS}^{noneq}$) is represented by the shaded purple curve. (B) IrDimen ground state population at equilibrium. (C) The populations immediately upon photoexcitation where the long/eclipsed isomer is selectively excited, creating a nonequilibrium excited state population ($P_{ES}$) (red) and a ground state hole ($P_{GS}^{noneq}$−$P_{GS}^{eq}$) (blue) (D) depicts cases without ground state reorganization, where only process (1) occurs, shown by the excited state population reaching shorter Ir−Ir distances. (E) shows the result of both (A) and (1), where, in addition to excited state reorganization, the ground state has restored equilibrium.

brium structures of the isomers of IrDimen through computational approaches has thus far proven to be challenging.

Previous theoretical studies on IrDimen used density functional theory (DFT) with various density functional approximations[1,10,12,13] and classical harmonic force field approximations for the Ir−Ir interaction potential[11] to determine the balance of forces that dictate the structure and dynamics of IrDimen. These prior DFT studies provide an essential context for our computational findings. Calculations with the generalized gradient approximation (GGA) exchange-correlation functional PBE as well as the hybrid functionals PBE0 and B3LYP, which include a fraction of exact exchange, find only one minimum energy geometry, corresponding to a long/eclipsed isomer, and overestimate the Ir−Ir distance by 0.2−0.3 Å. Adding a long-range dispersion interaction correction, such as D3, to the PBE0 functional improves the estimate of the Ir−Ir distance of the long/eclipsed isomer[1,10,12] and leads to a second minimum energy geometry, corresponding to a short/twisted isomer. The improved structure upon inclusion of the dispersion contribution indicates that long-range dispersion effects could be central in shaping the electronic potential energy surface of the ground state of IrDimen.

Dispersion corrections in DFT are typically functional dependent, raising the question of which combination of density functional approximation and dispersion correction can best describe the ground state structure of (molecules like) the IrDimen complex. While several benchmarks of the performance of density functional approximations in terms of their ability to describe complexes containing a single transition metal atom exist,[14−16] fewer benchmarks address $d^8$−$d^8$ bimetallic complexes.[6,17] Moreover, previous computational studies on IrDimen did not address the extent to which density functional approximations can describe the potential energy landscape of the complex, including the barrier between the two minima.

In the absence of reliable theoretical estimates, accurate experimental characterization is imperative. Extracting quantitative information about equilibrium populations from the UV−visible spectrum, as discussed prior, proves to be inconclusive. Specifically, quantitative analysis of the temperature dependent UV−visible spectra is impeded by (1) the different oscillator strengths associated with the two isomers likely due to non-Condon effects and (2) the large Franck−Condon factors for the low frequency Ir−Ir stretching vibration, making the shape of peaks within the absorption spectrum strongly temperature dependent.[18]

Given the complexity of interpreting IrDimen isomer populations through optical spectroscopy, we have found time-resolved X-ray solution scattering (XSS) to be a particularly effective probe to study the IrDimen isomerization, as it directly measures nuclear geometry and is thus unaffected by changes in oscillator strengths. Time-resolved XSS, with an optical pump pulse exciting the sample, directly measures optically induced changes in the structure of the complex, and can be used to map the electronic ground state potential energy surface.[19,20] Time-resolved XSS has been successfully used to elucidate the photoinduced structural dynamics of IrDimen.[21,22] However, due to experimental limitations, previous time-resolved XSS studies were unable to draw clear conclusions regarding the rate of interconversion between the IrDimen ground state isomers.

Haldrup and co-workers report that the IrDimen XSS signal acquired 100 ps after photoexcitation could be best fit when the model included two equilibrium ground state structures with Ir−Ir distances of 3.6 and 4.3 Å, consistent with crystal structure analysis.[22] In this study, the high energy X-ray probe at the European Synchrotron Radiation Facility (ESRF) provided the necessary spatial resolution to confidently determine the ground state structure, but the limited time resolution did not enable investigation of ground state isomerization dynamics. van Driel and co-workers[21] later performed time-resolved XSS measurements of IrDimen at the Linac Coherent Light Source (LCLS) with subpicosecond time resolution, but with longer wavelength X-ray pulses. Through these experiments, van Driel and co-workers were


https://doi.org/10.1021/jacs.4c00817
J. Am. Chem. Soc. 2024, 146, 13962−13973

able to identify excited state population dynamics, specifically a contraction of the Ir−Ir distance within 300 fs, but were unable to isolate in the scattering signal the contributions from ground state isomerization dynamics. This reflects the challenges of differentiating the many contributions to an ultrafast XSS signal with measured momentum transfer of $Q < 4.5$ Å$^{-1}$.

To address these challenges, we employ here ultrafast XSS at high photon energy and momentum transfer up to 8 Å$^{-1}$, which makes it possible to accurately track the relative populations of the deformational isomers as they evolve in time. In the presented experiments, we preferentially photoexcite the equilibrium population of the long/eclipsed isomer and observe changes to the overall ground state population with a delayed X-ray probe pulse. This preferential depopulation of the long isomer creates a nonequilibrium distribution on the electronic ground state potential energy surface that re-establishes equilibrium according to a thermal reaction rate dictated by the energy barrier between the two minima on the potential energy surface corresponding to the two isomers. Please find a schematic of the population dynamics in Figure 2.

Figure 2A depicts the excitation process. Photoexcitation with a 480 nm pump pulse creates an electronically excited population with a nonequilibrium structural distribution on the excited state potential energy surface, here $^1(d\sigma^*\ p\sigma)$. It then undergoes structural reorganization to form the excited state equilibrium geometry, depicted with process (1). Following geometry equilibration on the singlet excited state potential, the excited molecule undergoes intersystem crossing to the structurally similar $^3$d$\sigma^*$p$\sigma$ state with a 72 ps time constant and decays to the ground state with a 300 ns lifetime. These electronic excited state structural dynamics have been investigated previously with molecular dynamics simulations, OTAS, and ultrafast XSS.[10,22,23]

In a concomitant process, the electronic ground state, having a nonequilibrium distribution of the two structural isomers, undergoes structural reorganization, (A), which we describe below. Figure 2B shows the ground state population ($P_{GS}^{eq}$) (shaded purple) as a function of the Ir−Ir distance ($d_{Ir-Ir}$) when in equilibrium. Figure 2C depicts the system immediately upon photoexcitation, where the ground state has been selectively depopulated, forming electronic excited state ($P_{ES}$) (shaded red) and depleted electronic ground state ($P_{GS}^{noneq}$) (shaded blue) populations. The gray dashed line shows the original ground state equilibrium population. Figure 2D depicts ground and excited state populations some time after photoexcitation, in the case where only process (1) occurs, or reorganization of the excited state, with no changes to the ground state. The nonequilibrium difference population ($P_{ES} + P_{GS}^{noneq} - P_{GS}^{eq}$) where the electronic excited state has nearly reached its equilibrium, but the ground state distribution of the deformational isomers has not changed, is also shown. Lastly, Figure 2E shows the population distribution for a system where both the (1) and (A) processes have occurred and both electronic excited state and ground state hole populations have reached their structural equilibrium.

This approach of selectively exciting a narrow spectral range of a broad inhomogeneous band is a technique known as hole burning and has been shown to be a powerful tool to elucidate nonequilibrium dynamics in the ground state.[24] While hole burning dynamics have largely been probed with optical spectroscopy,[25] they can also be probed with time-resolved XSS to characterize the ground state potential energy surface, as recently demonstrated for the $[Pt_2\ (pyrophosphite)_4]^{4-}$.[26] In the presented experiment, the high-energy XSS probe is used to robustly determine the equilibrium rate constant for interconversion between the long/eclipsed and short/twisted isomers as well as the equilibrium ratio between the conformations. This enables us to estimate the magnitude of the relative free energy barrier that controls the isomer interconversion and also provides a means for assessing the ability of electronic structure methods to describe the potential energy surface of a metal−metal complex such as IrDimen, which has been a long-standing challenge for theory.[27] We evaluate the performance of a large range of density functional approximations and dispersion corrections against the experimental results and further compute the minimum energy path and energy barrier between the different minimum energy geometries. This test provides insights into the reaction coordinates for interconversion between the long/eclipsed and short/twisted isomers, complementing the experimental observations.

## METHODS

**X-ray Experimental Methods.** We conducted X-ray scattering measurements at the XCS endstation at the Linac Coherent Light Source (LCLS) at SLAC National Accelerator Laboratory, under conditions similar to those previously reported.[28] We delivered the 10 mM solution of IrDimen in acetonitrile to the interaction region through a closed-loop pump, generating a 50 $\mu$m cylindrical jet and full sample refresh for each probe event at 120 Hz. The sample reservoir was kept under a He atmosphere, and periodic addition of acetonitrile maintained the reservoir volume of 40 mL. The nozzle and catcher for the jet were contained in a He-filled sample chamber with a kapton-covered window allowing the scattered 18 keV ($\lambda = 0.7$ Å) X-ray photons to exit the chamber. We collect the scattered X-rays on the Epix 10k 2 M detector,[29,30] at scattering angles $2\theta$ between 3° and 55° corresponding to a $Q$-range of 0.7 to 8 Å$^{-1}$, $Q = (4\pi \sin(2\theta/2))/\lambda$.

The sample was photoexcited with 480 nm vertically polarized laser pulses generated by optical parametric amplification of the 800 nm fundamental of a titanium:sapphire laser, with pulse durations of 50 fs duration at full width at half-maximum, 4 $\mu$J of energy per pulse, and a spot size of 75 × 75 $\mu$m$^2$. These excitation conditions lead to single photon absorption and avoid nonlinear absorption, as shown in Figure S1 of the Supporting Information. The X-ray pulses were used to probe the sample after pumping with an optical laser. The time delay, $\Delta t$, between the optical laser excitation and the X-ray probe was varied in order to monitor the change in the scattering signal as a function of $\Delta t$. Additionally, we measured the shot-to-shot fluctuations in the relative time of arrival between the X-ray and the optical pulses for each pump/probe event using a timing diagnostic that measures the arrival time of the X-ray probe relative to the optical pump by measuring the increased optical absorption in $Si_3N_4$ resulting from X-ray generated carriers.[29]

We corrected the shot-to-shot fluctuations in X-ray wavelength using the measured shot-to-shot variation in electron beam energy[31] and the shot-to-shot fluctuations in X-ray pulse intensity with the integrated intensity on the detector. We also corrected detector images for the X-ray polarization, the geometry dependence of each pixel's solid angle coverage, and the geometric dependence of the X-ray absorption through the liquid jet.[31] We prepared a difference signal by first scaling data at all $Q$ values by the average intensity between 4.5 and 6 Å$^{-1}$, and then subtracting each optical laser-on shot by the average of 25 optical laser-off shots. We generated the $\Delta t$ dependent difference scattering signal by sorting the $\Delta S$ images by the timing tool measured $\Delta t$ into bins 20 fs wide. Lastly, we fit the two-dimensional $\Delta t$ dependent images into isotropic and anisotropic $Q$-dependent difference signals, as described in detail by Biasin et al.[32]


https://doi.org/10.1021/jacs.4c00817
J. Am. Chem. Soc. 2024, 146, 13962−13973

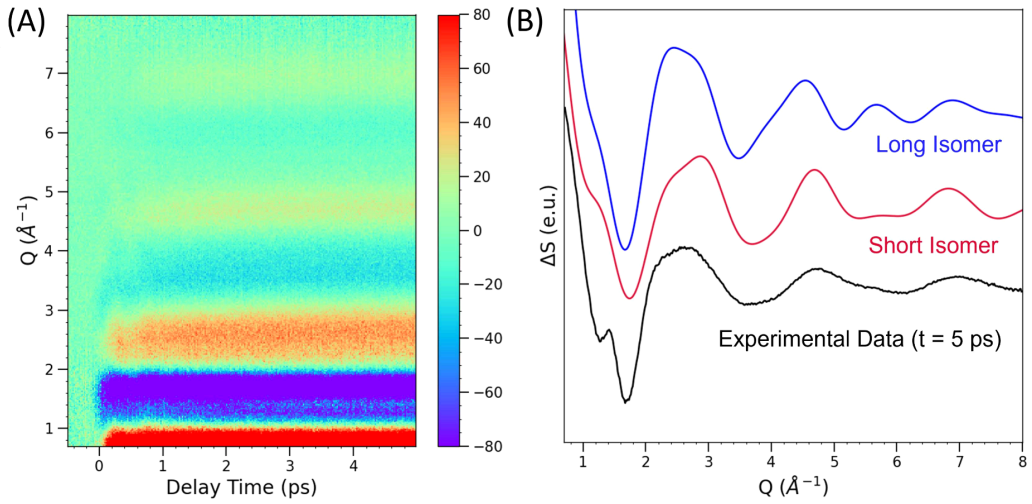


**Figure 3.** (A) Difference X-ray solution scattering for IrDimen in aceotnitrile. (B) Experimental difference XSS signal at delay time 5 ps (black) and simulated curves with an excited state Ir−Ir distance of 2.9 Å and ground state distances of 4.5 Å (blue) and 3.5 Å (red).

Our present study focuses on the isotropic difference signal, referred to as $\Delta S(Q, \Delta t)$ throughout the manuscript.

**Computational Methods.** We performed geometry optimizations of IrDimen using DFT calculations with several different functionals and corrections to include dispersion interactions. The functionals used include GGA, meta-GGA, hybrid, and long-range corrected exchange-correlation functionals. The dispersion corrections employed were D4,[33] D3[34] with the Becke−Johnson damping function (BJ),[35−37] and D3BJ[38] with three body interactions (D3BJ-ATM).[39] In all calculations, the orbitals were represented with the def2-TZVP basis set.[40] For each combination of functional and dispersion corrections, we performed two geometry optimizations: one starting from an initial guess for a long/eclipsed structure and the other starting from the short/twisted isomer structure. We performed all calculations without solvent unless otherwise stated. To identify the structure of the transition state for interconversion between the two deformational isomers, we performed minimum energy path calculations using the Nudged Elastic Band (NEB)[41,42] method with the climbing image algorithm[43] and energy-weighted spring constants.[44] An extended description of the simulation methods used can be found in the Supporting Information.

## RESULTS AND DISCUSSION

**Ultrafast X-ray Solution Scattering.** From the two-dimensional detector scattering signal for each shot, the isotropic component of the signal was extracted[32] and displayed with respect to $Q$ and delay time $t$, as shown in Figure 3a. The positive signal at low $Q$ corresponds to a decrease of atomic-pair distances,[45] which follows with the expected contraction of the Ir−Ir distance upon photoexcitation.[21,23,45] The increasing scattering signal intensity within the first 2 ps corresponds to the nuclear rearrangement of the system following instantaneous electronic rearrangement. Additionally, we observe oscillatory features within the first 500 fs, which correspond to the oscillations of the Ir−Ir contraction, as previously reported.[21]

The measured difference in the scattering signal is a combination of the changes to the solute, solvent, and solute−solvent interactions. Prior studies have demonstrated that solvent and solvent−solute signals are primarily localized at $Q < 3$ Å$^{-1}$,[21] so data at higher $Q$ can be confidently assigned to changes in the solute structure. This assumption is further supported by a comparison of IrDimen solutions in dimethylformamide (DMF) and acetonitrile (MeCN), where any differences between these two measurements due to solvation dynamics occur for $Q$-values below 3 Å$^{-1}$. (Figure S2)

The contribution of the solute to the total difference signal can be determined by simulating the scattering signal for the representative molecular structures. Simulated isotropic scattering as a function of $Q$ can be calculated by assuming the independent atom model approximation and using the Debye equation,

$$S(Q) = \sum_{i,j}^{N} \left[ f_i(Q) f_j(Q) \frac{\sin(Qr_{ij})}{(Qr_{ij})} \right] \quad (1)$$

where $i$ and $j$ represent all atoms in the molecule. The first term corresponds to the atomic scattering factors $f_i(Q)$ and $f_j(Q)$ for atoms $i$ and $j$, and $r_{ij}$ is the interatomic distance between atoms $i$ and $j$, making the second term correspond to the interference function between all pairs of atoms $i$ and $j$. Subtracting the scattering curves of a proposed ground state structure from scattering associated with a proposed excited state structure presents a simulation of the solute contribution of the scattering signal, $\Delta S_{\text{Solute}}(Q) = S_{\text{Excited State}}(Q) - S_{\text{Ground State}}(Q)$.

The high time resolution afforded by the short pulses at LCLS, in conjunction with the high spatial resolution of the scattering signal from the high photon energy, presents a new opportunity to observe the ground-state dynamics of IrDimen immediately following photoexcitation. The value of this experimental set up can be underscored by qualitatively comparing experimental data at 5 ps to simulated difference signals (Figure 3b). The two simulated signals have the same excited state geometry: one is derived from a ground state matching the long/eclipsed isomer geometry, and the other, from the short/twisted isomer. This comparison reveals several key insights. The difference between the simulated structures is more pronounced at high $Q$, and the experimental data appear to have contributions from multiple ground state structures, consistent with the observations made by Haldrup et al.[22] Both


https://doi.org/10.1021/jacs.4c00817
J. Am. Chem. Soc. 2024, 146, 13962−13973

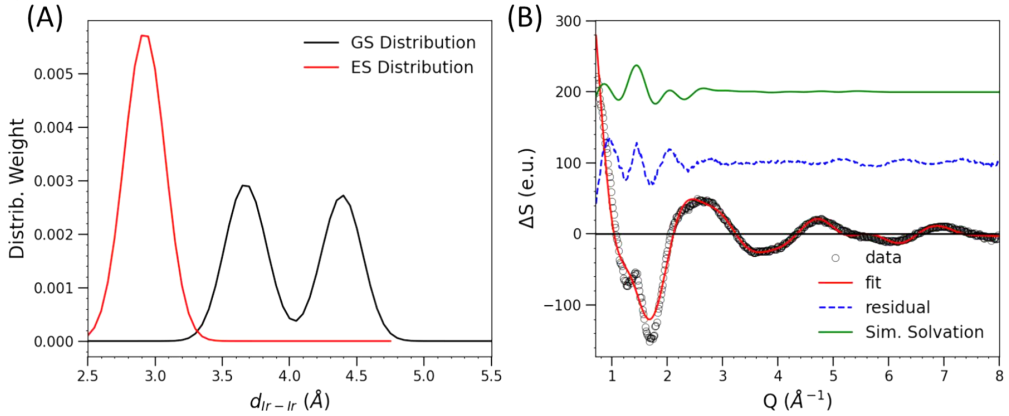


**Figure 4.** (A) Weighting terms $w$ for each Ir−Ir distance for fit of data at 5 ps. (B) Overlaid data (black), fit (red), and resulting residual (blue) for averaged 4.5−5 ps time delay. Simulated scattering signal due to changes in solvation as calculated previously[21] is shown in green.

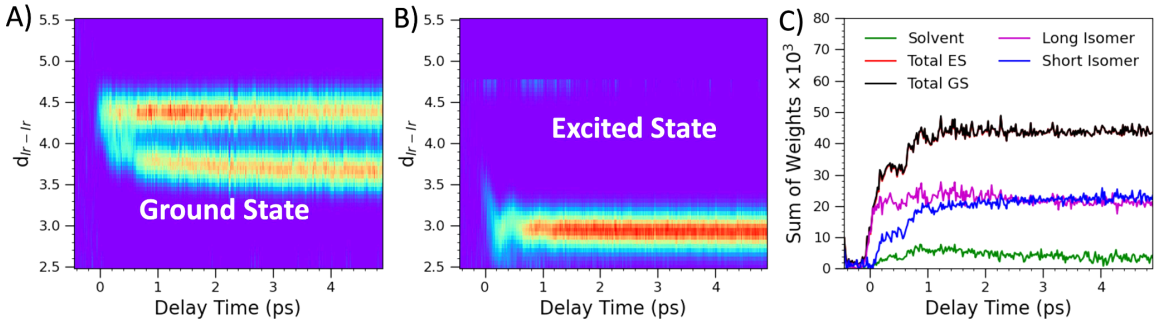


**Figure 5.** 2D contour map of weighting at each time delay and Ir−Ir distance for the ground state (a) and the excited state (b). Note that the fluctuations at 4.5 Å can be attributed to failures for the fit to capture the data in a reasonable manner at early times. (c) Sums of all weighting values at each delay time.

of these observations underscore the need for a larger $Q$-range. Lastly, despite exciting at a wavelength that would preferentially depopulate the long/eclipsed isomer, the experimental data show better agreement with the simulated signal from the short/twisted isomer, indicating any re-equilibration occurs within 5 ps, demonstrating the importance of high time resolution.

*Distribution Fitting.* To accurately capture the distributed nature of the IrDimen ground state, we use a distribution-based fitting method. By fixing the Ir−Ir pair distance at a set value and performing geometry optimization on all other atoms, we create a library of IrDimen structures in both the excited and ground states. For each structure, we simulate the scattering signal, resulting in a library of scattering signals for each Ir−Ir distance ranging from 2.5 to 5.0 Å in increments of 0.05 Å. These scattering patterns, along with the scattering contribution from bulk solvent heating, were weighted by the distribution term $w$, which we determined by minimizing the residual of the sum of all structures with the experimental data through a convex optimization method.[46] This approach allows for the possibility of a distribution of structures contributing to the final scattering signal rather than enforcing two specific ground state structures with specific geometries. A detailed discussion of the fitting procedures can be found in the Supporting Information.

The resultant fit shows good agreement with the data at 5 ps for $Q > 3$ Å$^{-1}$ (Figure 4). The most significant deviation from the predicted structure occurs at low-$Q$. This low-$Q$ residual shows strong similarity to the calculated signal from solute−solvent interactions, as outlined in previous work.[21] The fit describes a distribution of ground state Ir−Ir bond lengths with an excited state narrowly localized around one M−M distance. Critically, the ground state requires two distinct M/M distances to effectively fit the experimental findings. It is notable that a majority of the ground state contribution comes from the short/twisted conformation, demonstrating the electronic ground state bond isomerization is largely complete within the 5 ps measurement window.[22]

This time-resolved fit was obtained by independently fitting the XSS at each delay time by using the distribution method described above (Figure 5). Note that the early time dynamics ($t < 1.5$ ps) are not well captured by this fitting method. This discrepancy reflects the emphasis on sparse, nonoverlapping Ir−Ir bond distributions for the ground and excited state. This suppresses population dynamics where the ground and excited state distributions overlap, a property that dominates for short time delays. This artifact of our analysis method does not affect the results from time delays beyond 1.5 ps. We draw this conclusion from the fact that the total excited state population reaches a steady state value for time delays beyond 1.5 ps, as shown in Figure 5C.



https://doi.org/10.1021/jacs.4c00817
J. Am. Chem. Soc. 2024, 146, 13962−13973

This representation of the Ir−Ir distances with respect to time highlights key findings. As depicted in 5B, the excited state population converges onto a single structure with an Ir−Ir distance of 2.9 Å, consistent with prior analysis.[21,22]

The ground state hole dynamics are comparatively more complicated. As depicted in Figure 5C, at time delays less than 1.5 ps, the majority of the ground state scattering is due to depletion of the long/eclipsed GS conformation, following preferential excitation of the long/eclipsed conformation at 480 nm. However, by a time delay of 5 ps, the ratio of the ground state populations reverses, with the majority of the ground state coming from the short/twisted isomer. This provides clear, qualitative evidence that the ground state bond isomerization occurs on the few picosecond time scale.

Employing a hole-burning technique of selectively depleting one isomer from the ground state allows for indirect probing of the ground state potential surface. The fast time resolution afforded by LCLS provides the ability to extract not only the final equilibrium constants but also the rate at which re-equilibration occurs.

The relative populations of the long and short isomers can be calculated by summing the weighting values across distances above and below 4.0 Å, respectively. For a delay time of 5 ps, the ratio of short:long isomers is 53:47, with an uncertainty of 1.4. This value is in good agreement with the ratio of 55:45 ± 3.8, extracted from data collected at considerably longer delay times of 100 ps, which is also in line with prior reports,[22] confirming that equilibrium has largely been restored within the 5 ps experiment window.

Plotting the relative populations as a percentage of the total ground state population with respect to delay time provides a straightforward approach to understanding the kinetic behavior of the system, as seen in Figure 6. We can fit both curves with

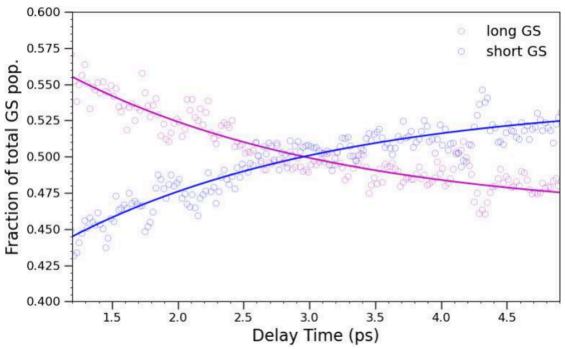


**Figure 6.** Fraction of the hole population in the long and short ground state isomers as a function of the delay time. Weight of long (purple) and short (blue) ground states calculated from distribution fitting shown with open circles, the resulting monoexponential fit depicted with a solid line.

an $A \rightarrow B$ model, where A represents the nonequilibrium population after excitation and B represents the molecules at equilibrium. Fixing the value of B at 55 and 45 for the short and long isomers respectively, based on the 100 ps delay time value, the re-equilibration fits well to a monoexponential time constant of 2.3 ps. The corresponding fits are depicted with a solid line in Figure 6, against the open circles from the distrubtion fit. This process was also observed in an optical transient absorption spectroscopy (OTAS) experiment, where following excitation at 480 nm, an interconversion of the ground state bleach signal appeared, which could be fit to a similar lifetime of 2.9 ps. See Supporting Information for a complete discussion of the OTAS data.

Using this observed overall rate, we can estimate relative rates for the forward and reverse deformational isomerization process as well as estimate the relative barrier heights along the isomerization coordinate. Treating the forward reaction as a conversion from the long/eclipsed ground state to the short/twisted conformation, and the backward reaction as the reverse, we see that at equilibrium, the reaction rates should meet the following equality, $k_{L\rightarrow S}\, n_{long} = k_{S\rightarrow L}\, n_{short}$. Given the extracted overall rate constant is a sum of the forward and backward rates, and the equilibrium ratio of 55:45 short:long isomer, forward and back rates have been calculated and summarized in Table 1.

**Table 1. Rates of Interconversion from Experimental Methods**

| Method | $1/k_{total}$ (ps) | $1/k_{L\rightarrow S}$ (ps) | $1/k_{S\rightarrow L}$ (ps) |
|---|---|---|---|
| Scattering | 2.3 | 5.1 | 4.2 |
| OTAS | 2.9 | 6.4 | 5.3 |

The difference in activation energy of the isomerization pathways ($\Delta G_{S-L}$), corresponding to the energy difference between the two isomers, can be approximated using the Arrhenius equation in the assumption that the pre-exponential factor $A$ for the forward and backward reactions is the same:

$$\ln k_{L\rightarrow S} = \ln A - \frac{E_{a,L\rightarrow S}}{k_b T}$$

$$\ln k_{S\rightarrow L} = \ln A - \frac{E_{a,S\rightarrow L}}{k_b T}$$

$$\ln\left(\frac{k_{L\rightarrow S}}{k_{S\rightarrow L}}\right) = \frac{E_{a,S\rightarrow L} - E_{a,L\rightarrow S}}{k_b T} = \frac{\Delta G_{S-L}}{k_b T} \quad (2)$$

where $E_{a,S\rightarrow L}$ and $E_{a,L\rightarrow S}$ are the activation energy of the isomerization pathways. The value of $\Delta G_{S-L}$ obtained in this way is equal to 5.15 meV, using the 55:45 short:long isomer ratio, as well as the rate constants shown in Table 1. The small activation energies and resultant ultrafast rate of isomerization stress the useful limits of transition state theory which relies on the rate of intrawell isomer equilibration to exceed the rate of interwell isomer interconversion, but do not invalidate the determination that a small free energy barrier separates the two deformational isomers of IrDimen.[47,48] The qualitative similarity between the measured rates for the deformational isomerization using two fundamentally distinct probes of the isomerization provides confidence that we have a robust experimental framework for assessing the molecular properties that control this chemical transformation.

**Computational Modeling.** With the experimental determination of the ground state Ir−Ir distances and population ratios, we have now acquired the necessary benchmarks to critically test how well a range of often used density functionals and long-range dispersion corrections reproduce the experimental findings.

*Geometry Optimizations.* Figure 7 shows the Ir−Ir distances for geometry optimized structures of IrDimen using different combinations of exchange-correlation functionals and



https://doi.org/10.1021/jacs.4c00817
J. Am. Chem. Soc. 2024, 146, 13962−13973

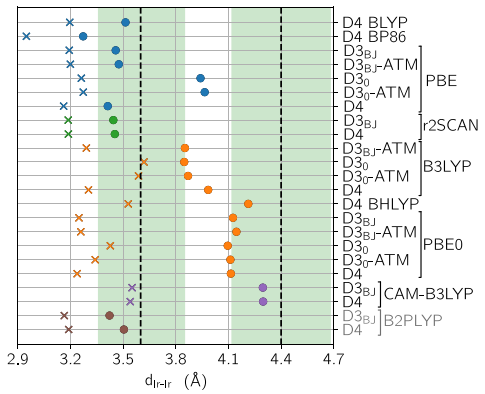


**Figure 7.** Ir−Ir distances, $d_{Ir-Ir}$, of the optimized geometries of IrDimen obtained by energy minimization in a vacuum using DFT with dispersion corrections, starting from guess structures for the long/eclipsed (●) and short/twisted (×) isomers. The marker colors denote the type of exchange-correlation functional used in the calculation; GGA:blue, Meta-GGA:Green, Hybrid:Orange, Range-Separated:Purple, Double-Hybrid:Brown. The black dashed lines represent the experimentally determined short/twisted and long/eclipsed isomer Ir−Ir distances. The green patches span the experimental uncertainties. The gray labels indicate that no frequency calculations have been performed. Good agreement with the experimental results is obtained only if the calculations use a hybrid functional, which includes exact exchange, together with a dispersion correction.

dispersion corrections as compared with the experimental values for the Ir−Ir distances of the two deformational isomers. Only the results of calculations that were able to converge on two distinct deformational isomers with Ir−Ir distances differing by more than 0.2 Å are included in this figure. The results for all the DFT approaches used are depicted in Figure S11 in the Supporting Information. We draw three primary conclusions from the comparison of different density functional based calculations to the experimentally extracted structures.

First, we observe the importance of dispersion interactions in correctly simulating isomer structures. Without a dispersion correction, all pure functionals only find a stable long/eclipsed isomer, regardless of the initial guess geometry in the structural relaxation (see Figure S11 in the Supporting Information). Moreover, the Ir−Ir distance of this isomer is overestimated on average by ∼0.2 Å compared to experiment when no dispersion correction is applied to the pure functionals. This is the case for all functionals, apart from r$^2$SCAN, which underestimates it by ∼0.3 Å.

Second, the choice of functional significantly influences the optimal geometries for the two isomers. For instance, including dispersion corrections in the calculations with GGA and meta-GGA functionals generates local minimum energy eclipsed and twisted isomers, but the calculated Ir−Ir distances underestimate the experimentally observed distances on average by ∼1.0 and ∼0.4 Å for the long/eclipsed and short/twisted isomers. Much better results are obtained when hybrid functionals are used together with a dispersion correction, with long/eclipsed- and short/twisted-isomer structures that underestimate the experimental Ir−Ir distance by ∼0.5 Å (∼10%), on average. The best results are obtained when using the BHLYP, PBE0 and CAM-B3LYP functionals with D4 or D3BJ corrections. Overall, these results indicate that only a hybrid functional, which includes a fraction of exact exchange, and dispersion corrections can correctly describe the balance between attractive interactions and ligand strain in the IrDimen complex, leading to an accurate structural prediction. The importance of dispersion interactions is in line with previous studies on molecules containing only a single metal atom.[49]

Third, the inclusion of solute−solvent interactions with a polarizable continuum solvent model (PCSM) improves the accuracy of the calculated isomer structures when compared to experiment, shown in Figure 8. For PBE0, the already

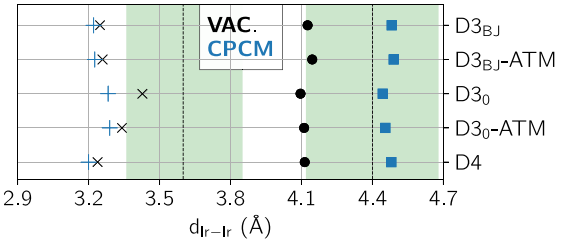


**Figure 8.** Ir−Ir distances, $d_{Ir-Ir}$, of the optimized geometries of IrDimen obtained by minimizing the energy given by the hybrid functional PBE0 with dispersion corrections in vacuum (black markers) and in acetonitrile as modeled with a polarizable continuum model (CPCM, blue markers), starting from guess structures for the long/eclipsed (● and ■) and short/twisted (× and +) isomers. The black dashed lines and green patches indicate the values deduced from X-ray solution scattering measurements and experimental uncertainties, respectively. Including solvent effects in the calculations improves the estimate of the Ir−Ir distance for the long/eclipsed isomers.

reasonable match with the experimental values is improved using a PCSM for acetonitrile. Inclusion of solvent effects leads to an increase in the Ir−Ir distance of the long/eclipsed isomers, giving an error of less than ∼0.1 Å (less than ∼3%) with respect to the experimental value for this isomer. However, it does not lead to significant changes in the Ir−Ir distance of the short/twisted isomer. This indicates that solvent screening of the Ir−Ir interactions plays a larger role for the long isomer, where the Ir atoms are more exposed to the solvent.

*Energy Difference and Minimum Energy Path.* For most of the combinations of exchange-correlation functional and dispersion correction that correctly identified two distinct isomers, the energy of the long/eclipsed isomer is higher than that of the short/twisted isomer (see Figure S13 in the Supporting Information), with the short/twisted isomer having an average energy 39 meV lower than the long/eclipsed isomer. Inclusion of the entropy difference (obtained via the frequency calculations) in the Gibbs free energy at 298 K between the two isomers makes the long/eclipsed isomer more stable by 26 meV because this isomer has lower frequency vibrational modes with correspondingly higher entropy. For the PBE0 hybrid functional with dispersion corrections, which displayed one of the best structural agreements with the experiments among all approaches, the Gibbs free energy of the long/eclipsed isomer is lower than that of the short/twisted isomer by ∼50 meV. The small free energy difference between the two isomers (the value of $k_bT$ at room temperature is ∼25 meV) and the greater stability of the


https://doi.org/10.1021/jacs.4c00817
J. Am. Chem. Soc. 2024, 146, 13962−13973

short/twisted isomer at low temperature are qualitatively consistent with the XSS measurement and previous temperature-dependent optical absorption measurements,[11] which reveal a preference for the short/twisted isomer at lower temperature. However, we note that for some of the investigated approaches intermediate energy minima could be found, indicating a rather shallow and rugged potential energy surface, which precludes a direct comparison with the experimentally determined population ratio.

Figure 9 shows the minimum energy path between the two deformational isomers obtained with the PBE0 hybrid functional, D4 dispersion correction, and CPCM solvation. The images are started out evenly spaced along $\Delta\mathbf{R}_n = \Sigma_i^n \sqrt{\Sigma_j^{3N}(q_j^i - q_j^{i-1})^2}$, but during the run, the energy-weighted spring algorithm causes images at the highest energies to experience stronger spring constants and images at the end points to experience lower spring constants. This leads to the congregation of images at the barrier top, which increases our information in the vicinity of the saddle point, giving a better estimate of the tangents around it.

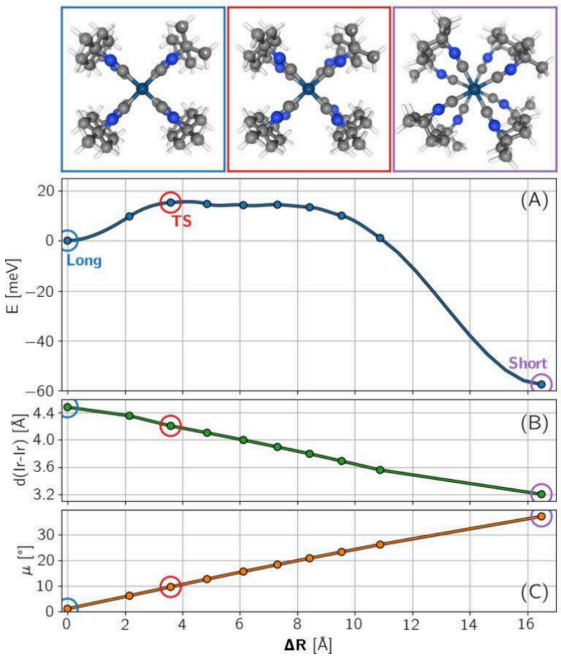


**Figure 9.** (A) Minimum energy path between the long/eclipsed and short/twisted isomers of IrDimen obtained with the PBE0 functional, the D4 dispersion correction, and a continuum solvation model for acetonitrile. The reaction coordinate is given as a cumulative root-mean-square displacement of the positions of the atoms with respect to the long/eclipsed isomer, $\Delta\mathbf{R}_n = \Sigma_i^n \sqrt{\Sigma_j^{3N}(q_j^i - q_j^{i-1})^2}$ for images $n$, where $N$ is the total number of atoms in the complex and $q_j$ are the atomic Cartesian coordinates. The solid line is a piecewise cubic interpolation between the energy of images along the path using the tangential atomic force. (B) Decrease in Ir−Ir distance along the minimum energy path. (C) Increase in the dihedral angle between square planar units of IrDimen (see Figure S10 in the Supporting Information for a definition of this angle) along the minimum energy path.

This calculation confirms that the potential energy surface is shallow with a very small energy barrier of ∼15 meV. The strong anharmonicity of the potential energy surface does not enable the use of harmonic transition state theory to estimate the rate of interconversion between the two isomers; however, the presence of a very small barrier is in agreement with the experimental observation that the interconversion is ultrafast with a time scale between 2 and 3 ps. Figures 9B and 8C show the change in Ir−Ir distance and angle between square planar units along the minimum energy path, confirming the dominant role of Ir−Ir contraction and torsion around the Ir−Ir bond in the interconversion between deformational isomers of IrDimen as proposed by Hill, Gray, and Hunter.[11,23] An interesting distinction, however, is the structure of the transition state. As shown in Figure 9, the transition state has a nearly eclipsed structure, while the empirical force-field developed by Hunter shows significant twisting about the Ir−Ir bond at the transition state.[11]

## CLOSING REMARKS

The $d^8$−$d^8$ metal dimer systems have absorption and emission properties that are highly sensitive to metal−metal distances. IrDimen provides a particularly interesting model to study these metal−metal interactions experimentally and theoretically because the complex has two distinct electronic ground state structures in equilibrium at room temperature, one with a 3.6 Å length and the other with a 4.4 Å Ir−Ir bond length. The steric force of the cyclohexane in the dimen ligand pushes the two square-planar components of the dimer away from one another, while an attractive dispersion force from both the ligands and metals pulls the moieties closer. The interplay of these counteracting forces results in two isomer conformations in solution. Through ultrafast X-ray solution scattering (XSS) and optical transient absorption spectroscopy (OTAS), we have revealed that the isomers lie in an equilibrium with just over half in the short/twisted conformation. Additionally, we demonstrated that these two deformational isomers interconvert with an ultrafast time constant of 2.3 ps.

The experimental results have been used to robustly assess the performance of a large range of density functional approximations, including dispersion interactions, in terms of their ability to describe the potential energy surface of IrDimen. We have determined that hybrid functionals, in conjunction with dispersion corrections and a solvent continuum model, can predict two minimum energy geometries in good agreement with the experimental data. The calculated energy differences between isomers—with and without entropy contributions—lie within the expected accuracy of the methods used,[50,51] and match the small differences in energy and activation barrier extracted from experimental methods. This represents a strong development in identifying computational methods to model multiple conformations of IrDimen.

To further explore the validity of specific computational methods, a broad library of $d^8$ dimer structures should be examined both experimentally and computationally. The shallow potential energy surface prevents harmonic approximations, so simulating structures with flexible isocyano-bridging ligands may provide a simple point of comparison. Additionally, a more in-depth comparison with Rh analogue complexes, particularly RhDimen, is vital to gaining deeper insight into the role the metal plays in the final structure, as RhDimen is reported to possess a similarly shallow and rugged


https://doi.org/10.1021/jacs.4c00817
J. Am. Chem. Soc. 2024, 146, 13962−13973

ground state potential energy surface, with multiple simulated conformations, but experimental evidence suggests the solution phase equilibrium strongly favors the long bond conformation.

## ■ ASSOCIATED CONTENT

### Supporting Information

The Supporting Information is available free of charge at https://pubs.acs.org/doi/10.1021/jacs.4c00817.

Additional details regarding scattering data processing and analysis, optical transient absorption data, and further computational details (PDF)

## ■ AUTHOR INFORMATION


### Corresponding Authors

**Adi Natan** − *PULSE Institute, SLAC Accelerator National Laboratory, Stanford University, Stanford, California 94025, United States*; Email: natan@stanford.edu

**Martin Meedom Nielsen** − *Department of Physics, Technical University of Denmark, 2800 Lyngby, Denmark*; orcid.org/0000-0002-8135-434X; Email: mmee@fysik.dtu.dk

**Kelly J. Gaffney** − *PULSE Institute, SLAC Accelerator National Laboratory, Stanford University, Stanford, California 94025, United States*; Email: kgaffney@slac.stanford.edu

### Authors

**Natalia E. Powers-Riggs** − *PULSE Institute, SLAC Accelerator National Laboratory, Stanford University, Stanford, California 94025, United States*; Present Address: Chemistry Department, University of San Francisco, San Francisco, California 94117, USA; orcid.org/0000-0002-9309-9622

**Benedikt O. Birgisson** − *Science Institute and Faculty of Physical Sciences, VR-III, University of Iceland, 107 Reykjavík, Iceland*

**Sumana L. Raj** − *PULSE Institute, SLAC Accelerator National Laboratory, Stanford University, Stanford, California 94025, United States*; Present Address: LCLS, SLAC National Laboratory, Menlo Park, California 94025, USA; orcid.org/0000-0001-5570-3350

**Elisa Biasin** − *PULSE Institute, SLAC Accelerator National Laboratory, Stanford University, Stanford, California 94025, United States*; Present Address: Physical Sciences Division, Physical and Computational Sciences Directorate, Pacific Northwest National Laboratory Richland, Washington 99354, USA

**Philipp Lenzen** − *Department of Physics, Technical University of Denmark, 2800 Lyngby, Denmark*; Present Address: PULSE Institute, SLAC Accelerator National Laboratory, Stanford University, Stanford, California 94025, USA

**Diana Bregenholt Zederkof** − *Department of Physics, Technical University of Denmark, 2800 Lyngby, Denmark*; Present Address: Scientific Instrument Femtosecond X-ray Experiments, European XFEL GmbH; orcid.org/0000-0001-5811-7525

**Morten Haubro** − *Department of Physics, Technical University of Denmark, 2800 Lyngby, Denmark*

**Dagrún K. V. Tveiten** − *Science Institute and Faculty of Physical Sciences, VR-III, University of Iceland, 107 Reykjavík, Iceland*

**Robert W. Hartsock** − *PULSE Institute, SLAC Accelerator National Laboratory, Stanford University, Stanford, California 94025, United States*

**Tim B. van Driel** − *LCLS, SLAC National Laboratory, Menlo Park, California 94025, United States*; orcid.org/0000-0003-4070-3168

**Kristjan Kunnus** − *LCLS, SLAC National Laboratory, Menlo Park, California 94025, United States*

**Matthieu Chollet** − *LCLS, SLAC National Laboratory, Menlo Park, California 94025, United States*; orcid.org/0000-0002-9629-890X

**Joseph S. Robinson** − *LCLS, SLAC National Laboratory, Menlo Park, California 94025, United States*

**Silke Nelson** − *LCLS, SLAC National Laboratory, Menlo Park, California 94025, United States*

**Ruaridh Forbes** − *LCLS, SLAC National Laboratory, Menlo Park, California 94025, United States*; orcid.org/0000-0003-2097-5991

**Kristoffer Haldrup** − *Department of Physics, Technical University of Denmark, 2800 Lyngby, Denmark*

**Kasper S. Pedersen** − *Department of Chemistry, Technical University of Denmark, 2800 Lyngby, Denmark*; orcid.org/0000-0002-4381-4544

**Gianluca Levi** − *Science Institute and Faculty of Physical Sciences, VR-III, University of Iceland, 107 Reykjavík, Iceland*; orcid.org/0000-0002-4542-0653

**Asmus Ougaard Dohn** − *Department of Physics, Technical University of Denmark, 2800 Lyngby, Denmark; PULSE Institute, SLAC Accelerator National Laboratory, Stanford University, Stanford, California 94025, United States*

**Hannes Jónsson** − *Science Institute and Faculty of Physical Sciences, VR-III, University of Iceland, 107 Reykjavík, Iceland*; orcid.org/0000-0001-8285-5421

**Klaus Braagaard Møller** − *Department of Chemistry, Technical University of Denmark, 2800 Lyngby, Denmark*; orcid.org/0000-0002-9797-7437

Complete contact information is available at: https://pubs.acs.org/10.1021/jacs.4c00817


### Notes

The authors declare no competing financial interest.

## ■ ACKNOWLEDGMENTS

N.P.R., E.B., S.L.R., A.N., R.W.H., and K.J.G. thank the U.S. Department of Energy, Office of Science, Office of Basic Energy Sciences, Chemical Sciences, Geosciences and Biosciences Division for supporting this work. B.O.B., G.L., and A.O.D. thank the Icelandic Research Fund (grant agreements no. 207014, 217734, and 196279, respectively). K.H., D.B.Z., and M.H. gratefully acknowledge support from the Novo Nordisk Foundation "NERD" program under Grant No. NNF20OC0061740. P.L., A.O.D., K.B.M., and M.M.N. gratefully acknowledge the support from the Independent Research Fund Denmark under Grant No. DFF-FP2 8021-00347B. The authors gratefully acknowledge support from the Linac Coherent Light Source, SLAC National Accelerator Laboratory, which is supported by the US Department of Energy, Office of Science, Office of Basic Energy Sciences, under contract no. DE-AC02-76SF00515. The European Synchrotron Radiation Facility (ESRF) is kindly acknowledged for provision of beamtime at the ID09 beamline. The calculations were carried out at the Icelandic High Perform-

ance Computing Center (IHPC). The authors thank Elvar Ö. Jónsson for help with the calculations.

## REFERENCES

(1) Gray, H. B.; Záliš, S.; Vlček, A. Electronic structures and photophysics of d8-d8 complexes. *Coord. Chem. Rev.* **2017**, *345*, 297−317.
(2) Yam, V. W.-W.; Au, V. K.-M.; Leung, S. Y.-L. Light-Emitting Self-Assembled Materials Based on d8 and d10 Transition Metal Complexes. *Chem. Rev.* **2015**, *115*, 7589−7728.
(3) Smith, D. C.; Gray, H. B. Photochemistry of binuclear d8 complexes. *Coord. Chem. Rev.* **1990**, *100*, 169−181.
(4) Atoji, M.; Richardson, J. W.; Rundle, R. E. On the Crystal Structures of the Magnus Salts, Pt(NH3)4PtCl41. *J. Am. Chem. Soc.* **1957**, *79*, 3017−3020.
(5) Chen, Y.; Li, K.; Lloyd, H. O.; Lu, W.; Chui, S. S.-Y.; Che, C.-M. Tetrakis(arylisocyanide) Rhodium(I) Salts in Water: NIR Luminescent and Conductive Supramolecular Polymeric Nanowires with Hierarchical Organization. *Angew. Chem.* **2010**, *122*, 10164−10167.
(6) Grimme, S.; Djukic, J.-P. Cation-Cation "Attraction": When London Dispersion Attraction Wins over Coulomb Repulsion. *Inorg. Chem.* **2011**, *50*, 2619−2628.
(7) Smith, D. C. Electronic Structure and Photochemical Reactivity of Binuclear Metal Complexes. PhD Dissertation, California Institute of Technology, Pasadena, California, 1989.
(8) Exstrom, C. L.; Britton, D.; Mann, K. R.; Hill, M. G.; Miskowski, V. M.; Schaefer, W. P.; Gray, H. B.; Lamanna, W. M. Structures of [M2(dimen)4](Y)2 (M = Rh, Ir; dimen = 1,8-Diisocyanomenthane; Y = PF6, Tetrakis[3,5-bis(trifluoromethyl)phenyl]borate, B(C6H5)4) Crystals Featuring an Exceptionally Wide Range of Metal-Metal Distances and Dihedral Twist Angles. *Inorg. Chem.* **1996**, *35*, 549−550.
(9) Gerlits, O.; Kovalevsky, A. Y.; Coppens, P. Solid-state spectroscopic properties and the geometry of binuclear rhodium(i) diisocyanoalkane complexes. *Dalton Transactions* **2004**, 3955−3962.
(10) Pižl, M.; Hunter, B. M.; Sazanovich, I. V.; Towrie, M.; Gray, H. B.; Záliš, S.; Vlček, A. Excitation-Wavelength-Dependent Photophysics of $d^8$-$d^8$ Di-isocyanide Complexes. *Inorg. Chem.* **2022**, *61*, 2745−2759.
(11) Hunter, B. M.; Villahermosa, R. M.; Exstrom, C. L.; Hill, M. G.; Mann, K. R.; Gray, H. B. M−M Bond-Stretching Energy Landscapes for $M_2(dimen)_4^{2+}$ (M = Rh, Ir; dimen = 1,8-Diisocyanomenthane) Complexes. *Inorg. Chem.* **2012**, *51*, 6898−6905.
(12) Záliš, S.; Hunter, B. M.; Gray, H. B.; Vlček, A. Electronic Structures of Reduced and Superreduced $Ir_2$(1,8-diisocyanomenthane)$_4^{n+}$ Complexes. *Inorg. Chem.* **2017**, *56*, 2874−2883.
(13) Dohn, A. O.; Jónsson, E. Ö.; Kjær, K. S.; van Driel, T. B.; Nielsen, M. M.; Jacobsen, K. W.; Henriksen, N. E.; Møller, K. B. Direct Dynamics Studies of a Binuclear Metal Complex in Solution: The Interplay Between Vibrational Relaxation, Coherence, and Solvent Effects. *J. Phys. Chem. Lett.* **2014**, *5*, 2414−2418.
(14) Garino, C.; Salassa, L. The photochemistry of transition metal complexes using density functional theory. *Philosophical Transactions of the Royal Society A: Mathematical, Physical and Engineering Sciences* **2013**, *371*, 20120134.
(15) Hopmann, K. H. How Accurate is DFT for Iridium-Mediated Chemistry? *Organometallics* **2016**, *35*, 3795−3807.
(16) Bursch, M.; Caldeweyher, E.; Hansen, A.; Neugebauer, H.; Ehlert, S.; Grimme, S. Understanding and Quantifying London Dispersion Effects in Organometallic Complexes. *Acc. Chem. Res.* **2019**, *52*, 258−266.
(17) Novozhilova, I. V.; Volkov, A. V.; Coppens, P. Theoretical Analysis of the Triplet Excited State of the $[Pt_2(H_2P_2O_5)_4]^{4-}$ Ion and Comparison with Time-Resolved X-ray and Spectroscopic Results. *J. Am. Chem. Soc.* **2003**, *125*, 1079−1087.
(18) Hunter, B. M.; Villahermosa, R. M.; Exstrom, C. L.; Hill, M. G.; Mann, K. R.; Gray, H. B. M−M Bond-Stretching Energy Landscapes for M2(dimen)42+ (M = Rh, Ir; dimen = 1,8-Diisocyanomenthane) Complexes. *Inorg. Chem.* **2012**, *51*, 6898−6905.
(19) Ihee, H. Visualizing Solution-Phase Reaction Dynamics with Time-Resolved X-ray Liquidography. *Acc. Chem. Res.* **2009**, *42*, 356−366.
(20) Haldrup, K.; Christensen, M.; Meedom Nielsen, M. Analysis of time-resolved X-ray scattering data from solution-state systems. *Acta Cryst. A* **2010**, *66*, 261−269.
(21) van Driel, T. B.; et al. Atomistic characterization of the active-site solvation dynamics of a model photocatalyst. *Nat. Commun.* **2016**, *7*, 13678.
(22) Haldrup, K.; Harlang, T.; Christensen, M.; Dohn, A.; van Driel, T. B.; Kjær, K. S.; Harrit, N.; Vibenholt, J.; Guerin, L.; Wulff, M.; Nielsen, M. M. Bond Shortening (1.4 Å) in the Singlet and Triplet Excited States of $Ir_2Dimen_4^{2+}$in Solution Determined by Time-Resolved X-ray Scattering. *Inorg. Chem.* **2011**, *50*, 9329−9336.
(23) Hartsock, R. W.; Zhang, W.; Hill, M. G.; Sabat, B.; Gaffney, K. J. Characterizing the Deformational Isomers of Bimetallic $Ir_2Dimen_4^{2+}$(dimen = 1,8-diisocyano-p-menthane) with Vibrational Wavepacket Dynamics. *J. Phys. Chem. A* **2011**, *115*, 2920−2926.
(24) Brito Cruz, C.; Gordon, J.; Becker, P.; Fork, R.; Shank, C. Dynamics of spectral hole burning. *IEEE J. Quantum Electron.* **1988**, *24*, 261−269.
(25) Schilling, D.; Mann, C.; Kunkel, P.; Schöppler, F.; Hertel, T. Ultrafast Spectral Exciton Diffusion in Single-Wall Carbon Nanotubes Studied by Time-Resolved Hole Burning. *J. Phys. Chem. C* **2015**, *119*, 24116−24123.
(26) Haldrup, K.; et al. Ultrafast X-Ray Scattering Measurements of Coherent Structural Dynamics on the Ground-State Potential Energy Surface of a Diplatinum Molecule. *Physics Review Letters* **2019**, *122*, No. 063001.
(27) Schmidbaur, H.; Schier, A. A briefing on aurophilicity. *Chem. Soc. Rev.* **2008**, *37*, 1931−1951.
(28) Alonso-Mori, R.; et al. The X-ray Correlation Spectroscopy instrument at the Linac Coherent Light Source. *Journal of Synchrotron Radiation* **2015**, *22*, 508−513.
(29) Blaj, G.; et al. X-ray detectors at the Linac Coherent Light Source. *Journal of Synchrotron Radiation* **2015**, *22*, 577−583.
(30) van Driel, T. B.; et al. The ePix10k 2-megapixel hard X-ray detector at LCLS. *Journal of Synchrotron Radiation* **2020**, *27*, 608−615.
(31) van Driel, T. B.; Kjær, K. S.; Biasin, E.; Haldrup, K.; Lemke, H. T.; Nielsen, M. M. Disentangling detector data in XFEL studies of temporally resolved solution state chemistry. *Faraday Discuss.* **2015**, *177*, 443−465.
(32) Biasin, E.; et al. Anisotropy enhanced X-ray scattering from solvated transition metal complexes. *Journal of Synchrotron Radiation* **2018**, *25*, 306−315.
(33) Caldeweyher, E.; Bannwarth, C.; Grimme, S. Extension of the D3 dispersion coefficient model. *J. Chem. Phys.* **2017**, *147*, No. 034112.
(34) Grimme, S.; Antony, J.; Ehrlich, S.; Krieg, H. A consistent and accurate ab initio parametrization of density functional dispersion correction (DFT-D) for the 94 elements H-Pu. *J. Chem. Phys.* **2010**, *132*, 154104.
(35) Becke, A. D.; Johnson, E. R. A density-functional model of the dispersion interaction. *J. Chem. Phys.* **2005**, *123*, 154101.
(36) Johnson, E. R.; Becke, A. D. A post-Hartree−Fock model of intermolecular interactions. *J. Chem. Phys.* **2005**, *123*, No. 024101.
(37) Johnson, E. R.; Becke, A. D. A post-Hartree-Fock model of intermolecular interactions: Inclusion of higher-order corrections. *J. Chem. Phys.* **2006**, *124*, 174104.
(38) Grimme, S.; Ehrlich, S.; Goerigk, L. Effect of the damping function in dispersion corrected density functional theory. *J. Comput. Chem.* **2011**, *32*, 1456−1465.
(39) Grimme, S. Supramolecular Binding Thermodynamics by Dispersion-Corrected Density Functional Theory. *Chemistry − A. European Journal* **2012**, *18*, 9955−9964.
(40) Weigend, F.; Ahlrichs, R. Balanced basis sets of split valence, triple zeta valence and quadruple zeta valence quality for H to Rn:


https://doi.org/10.1021/jacs.4c00817
J. Am. Chem. Soc. 2024, 146, 13962−13973

Design and assessment of accuracy. *Phys. Chem. Chem. Phys.* **2005**, *7*, 3297−3305.
(41) Ásgeirsson, V.; Jónsson, H. Exploring Potential Energy Surfaces with Saddle Point Searches. *Handbook of Materials Modeling* **2018**, 1−26.
(42) Jónsson, H.; Mills, G.; Jacobsen, K. W. In *Classical and Quantum Dynamics in Condensed Phase Simulations*; Berne, B. J. C. U., Ciccotti, G. U. R. L. S., Coker, D. F. B. U., Eds.; World Scientific: 1998; Chapter 16, pp 385−404.
(43) Henkelman, G.; Uberuaga, B. P.; Jónsson, H. A climbing image nudged elastic band method for finding saddle points and minimum energy paths. *J. Chem. Phys.* **2000**, *113*, 9901−9904.
(44) Asgeirsson, V.; Birgisson, B. O.; Bjornsson, R.; Becker, U.; Neese, F.; Riplinger, C.; Jónsson, H. Nudged Elastic Band Method for Molecular Reactions Using Energy-Weighted Springs Combined with Eigenvector Following. *J. Chem. Theory Comput.* **2021**, *17*, 4929−4945.
(45) Christensen, M.; Haldrup, K.; Bechgaard, K.; Feidenhans'l, R.; Kong, Q.; Cammarata, M.; Russo, M. L.; Wulff, M.; Harrit, N.; Nielsen, M. M. Time-Resolved X-ray Scattering of an Electronically Excited State in Solution. Structure of the 3A2u State of Tetrakis-$\mu$-pyrophosphitodiplatinate(II). *J. Am. Chem. Soc.* **2009**, *131*, 502−508.
(46) Diamond, S.; Boyd, S. CVXPY: A Python-Embedded Modeling Language for Convex Optimization. *Journal of Machine Learning Research* **2016**, *17*, 1−5.
(47) Wigner, E. The transition state method. *Trans. Faraday Soc.* **1938**, *34*, 29−41.
(48) Chandler, D. Statistical mechanics of isomerization dynamics in liquids and the transition state approximation. *J. Chem. Phys.* **1978**, *68*, 2959−2970.
(49) Chowdhury, S. R.; Nguyen, N.; Vlaisavljevich, B. Importance of Dispersion in the Molecular Geometries of Mn(III) Spin-Crossover Complexes. *J. Phys. Chem. A* **2023**, *127*, 3072−3081.
(50) Bykov, D.; Petrenko, T.; Izsák, R.; Kossmann, S.; Becker, U.; Valeev, E.; Neese, F. Efficient implementation of the analytic second derivatives of Hartree-Fock and hybrid DFT energies: A detailed analysis of different approximations. *Mol. Phys.* **2015**, *113*, 1961−1977.
(51) Perdew, J. P.; Schmidt, K. Jacob's ladder of density functional approximations for the exchange-correlation energy. *AIP Conf. Proc.* **2003**, *577*, 1−20.


https://doi.org/10.1021/jacs.4c00817
*J. Am. Chem. Soc.* 2024, 146, 13962−13973

# Paper III

## Localized and Delocalized Charge Distribution of a Diamine Cation: A Challenging Test for Density Functionals

Benedikt O. Birgisson, Hemanadhan Myneni, Elvar Ö. Jónsson, Ragnar Björnsson, and Hannes Jónsson

*To be submitted*

# Localised and Delocalised Charge Distribution in a Diamine Cation and Rydberg Excited State: A Challenging Test for Density Functionals

Benedikt O. Birgisson,[†] Hemanadhan Myneni,[†] Elvar Ö. Jónsson,[†] Ragnar Bjornsson,[‡] and Hannes Jónsson[*,†]

†*Science Institute and Faculty of Physical Sciences, Univ. of Iceland, Reykjavík, Iceland*

‡*Laboratoire Chimie et Biologie des Métaux, CEA-Grenoble, France*

¶*Department of Chemistry, Brown University, Providence, RI, USA*

E-mail: hannes_jonsson@brown.edu

**Abstract**

The balance between delocalised and localised charge distribution in the N,N'-dimethylpiperazine (DMP) molecule in the 3s Rydberg excited state and the fully ionised, $DMP^+$, provides a valuable test of density functionals, in particular the weight of Fock exchange (FE) in hybrid functionals and scaling of explicit self-interaction correction (SIC). Rydberg excitation measurements have shown evidence of a state where the hole is localised on one of the N atoms in addition to a lower energy delocalised state where the hole is distributed over both. Cations are generally assumed to have a nearly identical energy surface as high energy Rydberg states, but this has recently been called into question. We present results of calculations using density functionals of all rungs of Jacob's ladder, from LDA to the DM21 machine learned local hybrid as well as double hybrids. For the Rydberg DMP, a localised state is obtained with the PBE0 hybrid functional, while only the delocalised state is obtained for the cation. The LDA

and GGA functionals, such as PBE, however, only produce the delocalised state while hybrid functionals with stronger FE, such as PBE0(0.5FE) with double FE weight, as well as some double hybrids, produce a localised state also for the cation. The application of full SIC to PBE produces an energy surface that is similar to PBE0(0.5FE), while the scaling of SIC by 0.5 gives results analogous to PBE0.

# Introduction

The need to properly describe the relative energy of a localised and a delocalised electron distribution is a challenge that often comes up in the theoretical description of molecules, solid materials and biological systems. In mixed-valence compounds, for example, where two equivalent or near-equivalent redox sites are present, ionisation can result in the formation of either a localised or a delocalised electronic state.[1–5] Accurate description of these phenomena in electronic structure calculations has turned out to be a significant challenge, revealing deficiencies in both wave function theory (WFT) and density functional theory (DFT) based approaches. In commonly used implementations of DFT, i.e. Kohn-Sham functionals, an overemphasis on delocalisation is often present.[6,7] The semi-local functional form for the exchange-and-correlation term in the functional leads to incomplete cancellation of the non-local self-interaction error in the Kohn-Sham estimate of the classical Coulomb interaction, the Hartree term, since it is based only on the total electron density rather than orbital densities. In Hartree-Fock (HF) calculations, however, where the self-interaction in the Hartree term gets cancelled out by the self-interaction in the infinite range Fock exchange (FE), there is an overemphasis on localised states. Hybrid functionals, where FE based on Kohn-Sham orbitals is included with some weight, can improve the balance between localised and delocalised states but the calculated results depend strongly on the value chosen for the weight factor. The most commonly used hybrid functionals, which have a weight of 0.20 to 0.25, can still overemphasise delocalisation. A common pragmatic way of dealing with this problem is to increase the weight of FE and for some systems it has been found that a weight

larger than 0.35 is necessary to describe correctly molecules with highly localised charge.[8] In the original hybrid functional, referred to here as BHLYP,[9] where the weight coefficient was derived approximately using the adiabatic connection formula, the value is even larger, 0.5. However, too large weight on FE, can lead to an erroneously localised description of intrinsically delocalised systems.

DFT functionals can be tested against high-level WFT results for small enough molecules. Kaupp and coworkers have discussed several inorganic[10,11] and organic mixed-valence systems[12–16] that present considerable challenge for DFT approaches. Overall, global hybrid functionals with a factor of 0.35 to 0.45 for Fock exchange, as well as range-separated and local hybrid functionals, have been found to give good agreement with high-level WFT calculations in many cases. Range-separated hybrid DFT functionals have recently been been shown to describe well delocalisation in three organic mixed valence molecules.[17]

A less explored way of dealing with the problem is to apply explicit self-interaction correction such as that proposed by Perdew and Zunger (PZ-SIC).[18] There, a correction is made for each orbital separately so it represents an independent electron approach and the full correction is found to lead to results similar to HF calculations in many cases, such as for the atomisation energy of molecules.[19] A scaling of the PZ-SIC by a half based on a justification analogous to that used in the derivation of the original hybrid functional[9] has been shown to give good estimates of atomisation energy as well as band gaps of solids.[19,20] However, in order to obtain the correct -1/$r$ long range form of the effective potential, which is, in particular, important for the description of the diffuse electron in a Rydberg state of a molecule or a loosely bound anion, the full PZ-SIC is required.[21,22] PZ-SIC has been implemented in a variational, self-consistent way with complex valued orbitals[23–26] and it has been shown to give good results in studies of several molecules and solids, in particular where the delocalisation error is significant in commonly used Kohn-Sham functionals.[27]

In a recent effort, machine learning has been used to construct density functionals of the local hybrid form where, among other things, data on the balance between localised and

delocalised states is included in the training.[28] This deep mind functional, referred to as DM21, is generated by training a neural network with extensive molecular data in particular where fractional charge and spin problems occur in regular Kohn-Sham functionals. It has been shown to describe well main group thermochemistry and systems exhibiting energy or density errors due to self-interaction error. A few variants have also been developed with different training sets, namely DM21m, DM21mc and DM21mu.

The N,N'-dimethylpiperazine (DMP) molecule has been shown to be a challenging case where both a localised state with spin density centred on one of the N atoms exists and a more delocalised state with the charge distributed on both N atoms.[29] Upon excitation, the localised state is initially formed, but the molecule later converts to a more stable delocalised state where the binding energy for the Rydberg electron is lower. In a Rydberg state, an electron is excited into a diffuse orbital with large spatial extent and provides, to first approximation, a nearly uniform background charge for the molecular ion core. The question is whether a localised state similarly exists for the cation where an electron has been fully removed. The molecular structure corresponding to the two states as obtained for the cation using the BHLYP functional is shown in figure 1. The two states correspond to significant differences in the atomic coordinates and, thereby, different minima on the potential energy surface. The Rydberg state energy surface is generally assumed to be nearly identical to that of the corresponding cation, consistent with the narrowness of peaks in the ionisation spectra of Rydberg molecules. Ionisation spectra of Rydberg molecules have narrow peaks consistent with little vibrational broadening indicating that the the energy surfaces of the Rydberg and cation have similar shape. The existence of a localised state for the Rydberg excited molecule has, therefore, been taken to indicate the existence of a localised state for the cation.[29]

Calculations using several electronic structure methods do not, however, produce a localised state energy minimum on the $DMP^+$ energy surface, suggesting the cation either is highly challenging for electronic structure methods or, alternatively, that the Rydberg state

energy surface is significantly different from that of the cation. The BHLYP functional predicts the presence of a localised state energy minimum, while most commonly used density functionals do not.[29] When full PZ-SIC is applied to the PBE functional[30,31] as is needed to describe well the highly diffuse Rydberg orbital, an energy minimum on the energy surface corresponding to a localised state is produced. However, some trusted WFT methods, such as the single reference coupled cluster CCSD(T) approach, do not produce a local minimum on the energy surface representing the localised state (even though CCSD does) while higher-level multi-reference MRCI+Q calculations do.[32] The existence of a localised state of the $DMP^+$ cation has become a controversial topic.[33,34] Most recently, Kaupp and co-workers[35] presented a comparison of state-specific and state-averaged multireference calculations, demonstrating that state-averaged calculations are in agreement with CCSD(T) in that a localised state is not produced. They suggest that the state-specific MRCI+Q calculations used in Ref.[32] lead to artificial symmetry-breaking. The 3s Rydberg DMP, however, calculated with equation-of-motion coupled cluster calculations is found to produce a localised state separated by a small energy barrier from the delocalised state. The energy of the Rydberg electron is lower when the hole is more localised and if the energy surface is sufficiently flat, this stabilisation could induce a local energy minimum for a localised state.

The $DMP^+$ cation and comparison with the Rydberg excited state thus represents a significant challenge for electronic structure methods, whether they are based on wave function or density functional approaches. The large spatial extent of the Rydberg orbital provides, furthermore, a challenge when calculations are carried out using atomic basis sets because of the need to include diffuse enough basis functions. Otherwise, the Rydberg orbital can be artificially confined, as has been demonstrated recently in calculations using a real space grid representation.[36]

Here, we report results of density functional calculations of the DMP cation and 3s Rydberg states, comparing functionals of all rungs of Jacob's ladder: LDA, GGA, meta-GGA, hybrid-GGA, hybrid meta-GGA, and double hybrids. Additionally, range-separated

hybrid functionals such as ωB97X-V and ωB97M-V and the recent machine-learned local hybrid DM21 functional is applied (as well as its other variants DM21m, DM21mc and DM21mu).[28] Finally, the effect of full PZ-SIC applied to PBE is re-evaluated with tighter convergence criteria than was used previously[29] and comparison made with results using a downscaled correction, PBE-SIC/2, which has previously been shown to give better results for atomisation energy of molecules and band gap of solids.

# Methods

Most of the DFT calculations were carried out using the aug-cc-pVDZ[37,38] basis set as implemented in the ORCA quantum chemistry software version 5.0.0.[39] However, the self-interaction corrected PBE calculations (both full correction, PBE-SIC, and scaled correction, PBE-SIC/2, were carried out using the GPAW software and a grid based representation of the valence electron orbitals combined with the projector augmented wave representation of the effect of the inner electrons.[26] A grid representation of the aug-cc-pVDZ basis functions is used in those calculations. In order to test the consistency of the two approaches, the calculations using the PBE functional were done in both ways and the difference in the resulting energy surface found to be insignificant. Calculations using the DM21 functionals[28] were carried out with the PySCF software[40–42] and the aug-cc-pVDZ basis set.

The Rydberg excited state calculations were carried out using a variational, orbital optimised, state specific method where an excited state is obtained by converging on the corresponding saddle point on the electronic energy surface[43,44] as implemented in version 6.0.0 of the ORCA quantum chemistry software.

Calculations of the energy barrier between the localised state, when present, and the delocalised state were carried out using the climbing image nudged elastic band method[45–47] including 5 intermediate images. The calculations were considered to be converged when the magnitude of the force on each atom in the climbing image dropped below 0.01 eV/Å.

Energy surfaces characterising the cation were generated by producing a grid of 78 values for the two dihedral angles, D1 and D2, of the six-membered ring (illustrated in Fig. 1) and minimising the energy with respect to the remaining degrees of freedom in atomic positions, except in the DM21 calculations where the atomic coordinates obtained with BHLYP were used because analytical atomic forces have not become available for this functional. The calculated points were interpolated with a biharmonic spline interpolation using Matlab[48] to produce smooth energy surfaces. For all the functionals used here, the global minimum on the energy surface corresponds to a delocalised electronic state. A localised state is also found for some of the functionals, i.e. two higher energy minima on the energy surface corresponding to symmetrically equivalent molecular structures where the positive charge is centred on one of the two N-atoms.

# Results

Figure 1 shows how the energy of $DMP^+$ varies as a function of the two dihedral angles, D1 and D2, for the original hybrid functional, BHLYP,[9] which has a weight of 0.5 on FE. The insets show the atomic structure of the cation in the two states and the definition of the two dihedral angles that are used here to characterise the structure. The energy is minimised with respect to the remaining degrees of freedom. This energy surface has been reported previously in Ref.[32] and is reproduced here for reference because the obtained atomic coordinates are used in some of the subsequent calculations. Two symmetry equivalent minima corresponding to a localised state are clearly seen, at around (130°,-170°) and (170,-130°), in addition to the global minimum corresponding to the delocalised state at (90°,-90°).

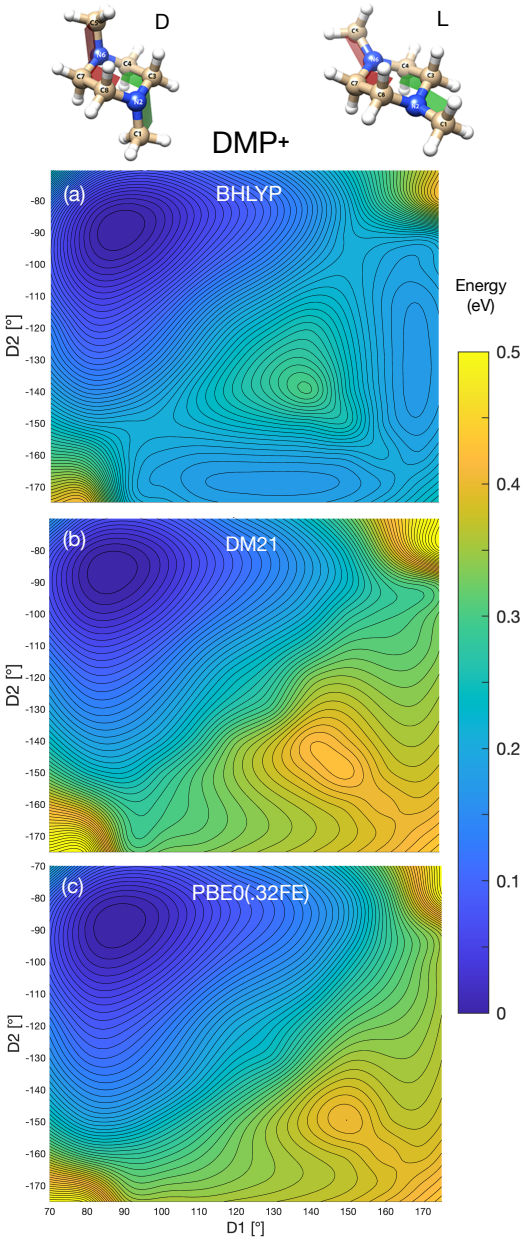


Figure 1: Structure and energy surfaces of $DMP^+$. Top: Delocalised (left) and localised (right) states. Planes defining the two dihedral angles of the six-membered ring, D1 (C1,N2,C3,C4) and D2 (C5,N6,C7,C8), are shown in green and red. (a): Energy obtained using the BHLYP functional[9] where the weight on FE is 0.50. The atomic structure used for generating the energy surface is obtained by fixing the two dihedral angles for a grid of values and minimising the energy with respect to the remaining degrees of freedom. (b): Energy obtained using the neural network optimised DM21 functional[28] of a local hybrid form using the atomic structure obtained from the calculation in (a). Here, only the delocalised minimum is present, but energy valleys stretching towards the regions of the localised state are formed. (c): Energy obtained using the PBE0 functional[49] with increased FE weight from 0.25 to 0.32 in order to match roughly the DM21 energy surface shown in (b).

Figure 1 also shows an energy surface obtained with the neural network generated DM21 functional which is trained to give piece-wise linear energy dependence for both fractional charge and spin.[28] It can, therefore, be expected to give an accurate estimate of the balance between localised and delocalised charge distribution. Since analytical atomic forces are not available for this functional, the atomic coordinates obtained from the BHLYP calculation shown in (a) are used to generate the points on the energy surface. Unlike the BHLYP results, local energy minima corresponding to a localised state of $DMP^+$ are not evident here, but there are clear energy valleys up from the delocalised state minimum towards the regions corresponding to the localised state.

Figure 1 also shows the energy surface generated using the global hybrid PBE0 functional[49] where the weight of FE has been increased from the usual value of 0.25 to 0.32, referred to as PBE0(.32FE), in order to match roughly the DM21 energy surface. This shows that a pretty good match can be obtained for this energy surface with a global hybrid and the optimal value for the FE weight is similar to what has been used for mixed-valence systems, as mentioned above.

Figure 2 shows the energy surfaces generated using two commonly used functionals, the PBE functional,[30,31] which is of the generalised gradient approximation (GGA) form, and the hybrid PBE0 functional[49] with the usual FE weight of 0.25. Here, only D1 and D2 are fixed and the energy minimised with respect to the remaining degrees of freedom. For the PBE functional, there is a hint of an energy valley along the symmetry line, instead of the regions corresponding to the localised charge distribution. The inclusion of FE with this low weight for FE does not change the shape of the energy surface much, mainly raises the energy near the symmetry line. As shown in figure 1(c), an increase of the weight from 0.25 to 0.32 is enough to produce a significant change and create energy valleys in the region of the localised state.

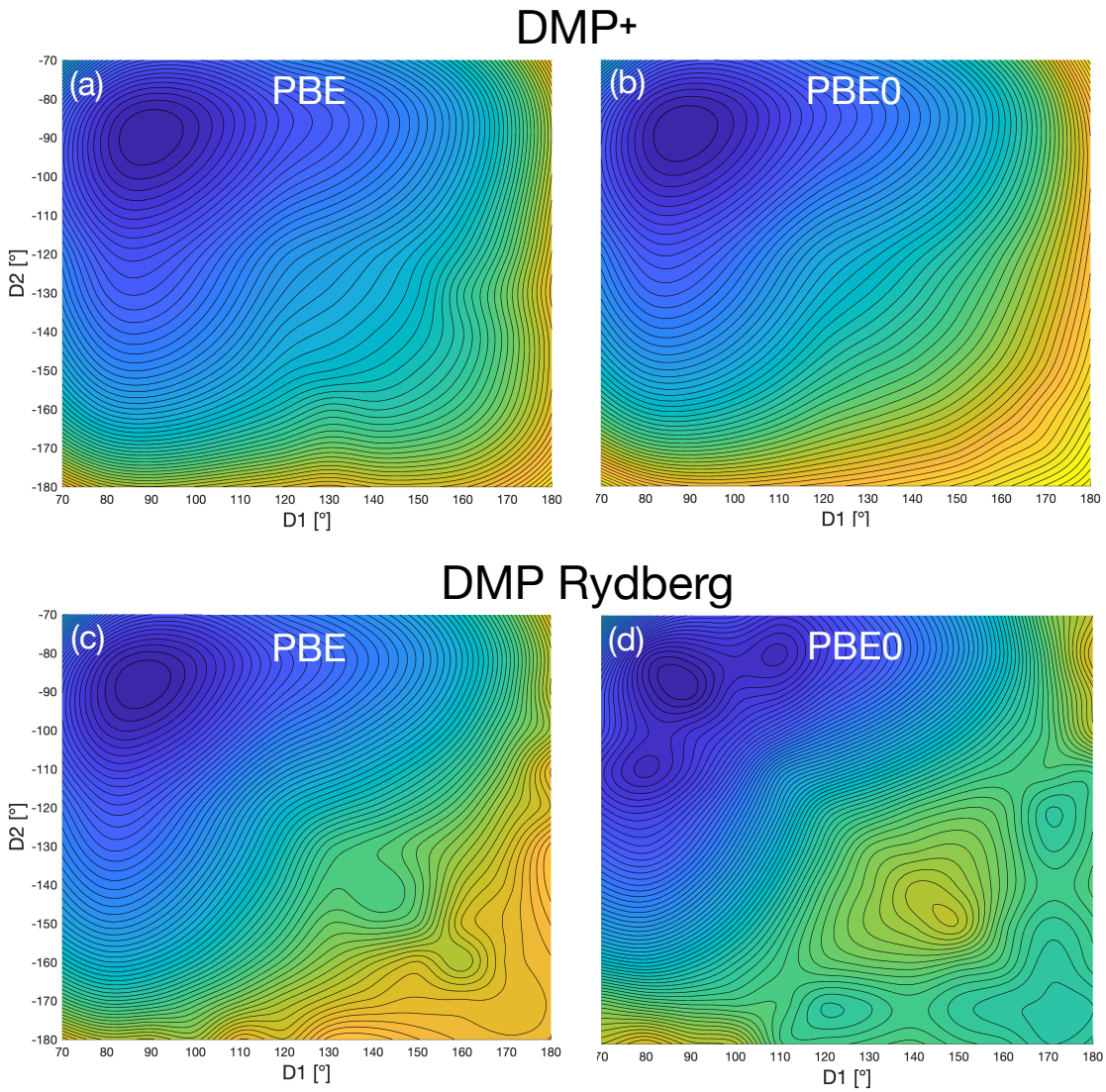


Figure 2: Energy surfaces for the $DMP^+$ ion (top) and the 3s Rydberg state of DMP (bottom). (a) and (c) show results of calculations using the PBE generalised gradient approximation functional, while the PBE0 global hybrid functional with the usual weight of 0.25 for FE is used in the calculations shown in (b) and (d). A clear difference is seen between the cation and Rydberg state energy surfaces, especially for the PBE0 hybrid functional where the self-interaction error has been reduced by inclusion of FE. The colour scale is the same as in figure 1.

Figure 2 also shows the energy surfaces of the DMP molecule in the 3s Rydberg state using the PBE and PBE0 functionals. For the PBE functional, there is still only an energy

minimum corresponding to the delocalised state, but when the PBE0 functional is used, additional minima appear corresponding to a localised hole. There is indeed clear difference between the energy surfaces for the $DMP^+$ ion and the Rydberg state, especially for the PBE0 functional. The local minimum on the PBE0 surface at around (175°,-175°) corresponds to an equitorial arrangement of the methyl group at the N atom where the hole is located, while the slightly shallower local minima at around (120°,-170°) and (170°,-120°) correspond to axial arrangement.

While the PBE0 functional does not produce minima on the energy surface of the $DMP^+$ ion corresponding to the localised state, the BHLYP surface does, as shown in figure 1. The reason for this difference is mainly the different weight of FE. Figure 3 shows the effect of increasing the weight to 0.5 in a functional referred to here as PBE0(0.5FE). The shape of the PBE0(0.5FE) surface is quite similar to that of BHLYP, although the location of the local minima is shifted a bit. The energy of the localised state with respect to the delocalised state is quite similar, 0.2 eV, but the energy barrier for the transition from the localised state to the delocalised on is a bit lower, see table 1. The variation of the energy along the minimum energy path from a localised state to the delocalised state is shown in figure 4.

The improvement in accuracy by going from GGA functional form to a hybrid by including FE results from a reduction of the self-interaction error. This can be illustrated by applying an explicit self-interaction correction of the Perdew-Zunger form to the PBE functional. The resulting energy surface is shown in figure 3 (right). Clear minima are then present on the energy surface corresponding to the localised electronic state. The overall shape of the energy surface is similar to that of the PBE0(0.5FE) functional. The energy of the localised state with respect to that of the delocalised state is 0.23 eV, close to the value obtained from PBE0(0.5FE), but the energy barrier for the transition to the delocalised state is a bit higher, 0.046 eV (see table 1). The variation of the energy along the minimum energy path from a localised state to the delocalised state is shown in figure 4. The path is shorter than the one calculated with the PBE0(0.5FE) functional mainly because a methyl

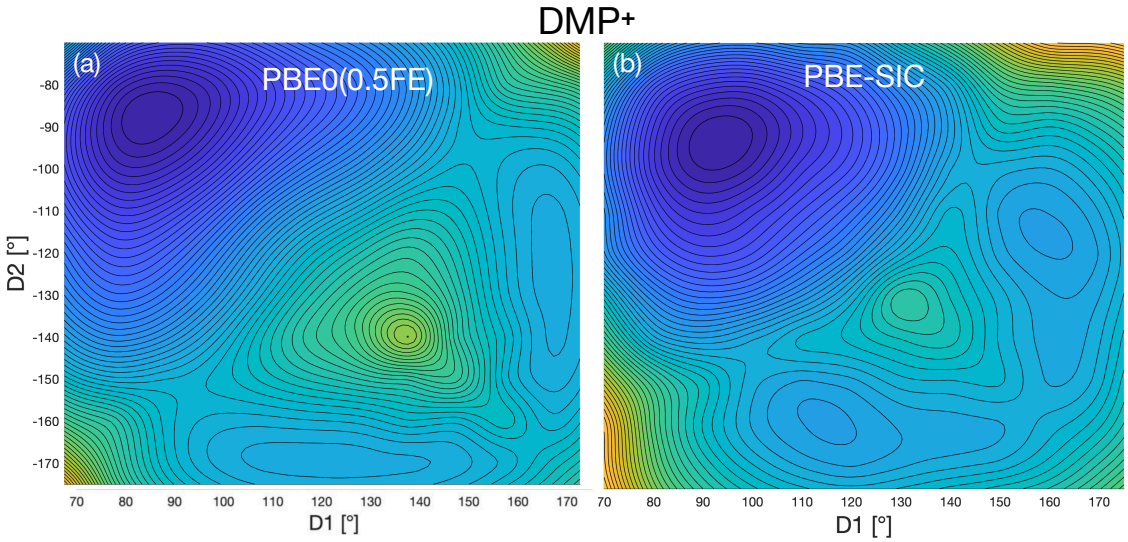


Figure 3: Energy surfaces for the $DMP^+$ ion. (a) Using PBE0(0.5FE) functional where the weight on FE is 0.5. Localised state minima are present, in addition to the delocalised state global minimum. (b) Using using the PBE functional with full orbital based Perdew-Zunger self-interaction correction. The two energy surfaces are qualitatively similar and give similar energy difference between localised and delocalised states, as well as energy barrier between the two states (see table 1, and figure 4). The colour scale is the same as in figure 1.

group rotates less, but this involves only a small energy change. Here, the full orbital based Perdew-Zunger correction is applied,

Calculations are also carried out using a functional where SIC is scaled by a half as has been shown previously to give more accurate results for both atomisation energy of molecules and band gap of solids. This functional is referred to as PBE-SIC/2. When a careful energy minimisation is started using the atomic structure obtained from the PBE-SIC calculation for the localised state, the configuration of the atoms changes to that of the delocalised state, showing that only the delocalised state is obtained with the PBE-SIC/2 functional. The scaling down of the self-interaction error reduces the stability of the localised state enough for the local energy minimum on the PBE-SIC energy surface to vanish. Comparison of the energy surfaces for PBE0(0.5FE) and PBE-SIC shows that the application of full SIC has similar effect as including FE with a coefficient of 0.5 in the PBE0(0.5FE) functional, while SIC scaled down by 0.5 gives similar results as the PBE0 functional.

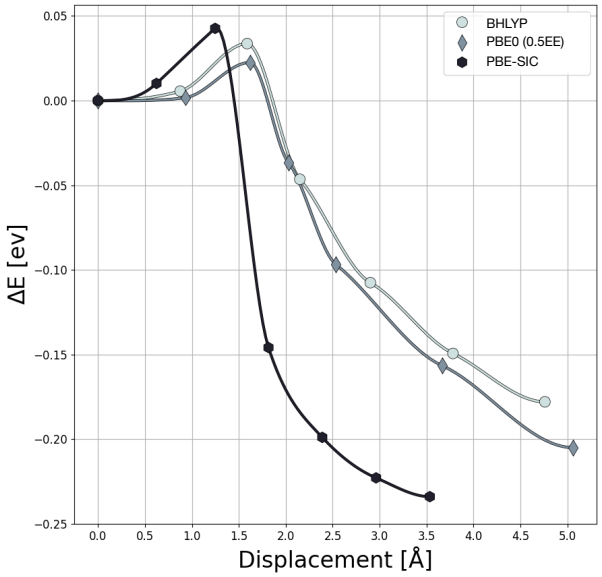


Figure 4: Energy along the minimum energy path between the localised and delocalised states of $DMP^+$ calculated using the BHLYP, PBE0(50) and PBE-SIC functionals. The total path length differs mainly because of a rotation of the methyl groups which, however, correspond to only small change in the energy.

Table 1: Energy barrier, $E_b$, for the transition from the localised electronic state (when present) to the delocalised state, and the corresponding change in energy, $\Delta E$, for the $DMP^+$ ion. The values for the functional calculations are obtained from full nudged elastic band calculations, not from the two-dimensional energy surfaces. The wave function based multi-reference configuration interaction, MRCI+Q, results are taken from Ref.[32]

| Functional | $E_b$ [eV] | $\Delta E$ [eV] |
|---|---|---|
| PBE0(0.5FE) | 0.022 | -0.21 |
| BHLYP | 0.033 | -0.18 |
| PBE-SIC | 0.046 | -0.23 |
| B2GPPLYP | 0.002 | -0.48 |
| DSD-BLYP | 0.013 | -0.56 |
| DSD-PBEP86 | 0.017 | -0.49 |
| MRCI+Q | 0.054 | -0.38 |

Several other functionals are tested. The full list is given in table 2 where it is specified whether or not a metastable localised state is found. In each case, a minimisation of the energy with respect to atom coordinates is carried out using a careful optimisation based on accelerated steepest descent starting from an initial configuration corresponding to the

localised state. Spin population analysis is used to determine whether a delocalised or a delocalised electronic state is obtained in the end. For all the GGA and meta-GGA functionals, such calculations produce only the delocalised state minimum. This includes the SCAN and r$^2$SCAN meta-GGA functionals. Global hybrid functionals, such as B3LYP and PBE0, also only give the delocalised sate unless the weight on Fock exchange is increased to 0.4 or more. Range-separated hybrid functionals are also not found to produce a metastable localised electronic state.

Finally, calculations are carried out using four double-hybrid density functionals that incorporate both FE and MP2 correlation. They typically include higher weight on FE than regular hybrids, enabled by the inclusion of a fraction of MP2 correlation. The B2GPPLYP (with 0.65FE),[50] B2PLYP (with 0.69FE)[50] and DSD-BLYP (with 0.70FE)[51] functionals give a metastable localised state as well as the delocalised state, while the B2PLYP (with 0.53FE)[52] functional only gives the delocalised state, see Table 2. The energy of the localised state, when present, is quite high, as shown in Table 1. The energy barrier for a transition from the localised state to the delocalised state is similar for the DSD-PBEP86 and DSD-BLYP functionals, 0.017 eV and 0.013 eV, close to that obtained with the PBE0(0.5FE) functional. The B2GPPLYP functional produces a smaller barrier, see table 1. The more recently developed local hybrid functionals[53] are interesting alternatives but are not included in this work.

Table 2: List of the various density functionals tested and an indication whether a local minimum corresponding to a localised state, L, is found on the energy surface of the $DMP^+$ ion.

| Functional | L state |
|---|---|
| **GGA:** | |
| BLYP[54,55] | - |
| BP86[56,57] | - |
| OLYP[55,58] | - |
| PBE[30,59] | - |
| PW91[60] | - |
| RPBE[61] | - |
| **meta-GGA:** | |
| B97M-D3BJ[62] | - |
| TPSS[63] | - |
| revTPSS[64] | - |
| r2SCAN[65] | - |
| **Global hybrids:** | |
| TPSS0[66] | - |
| TPSSh[66] | - |
| B3LYP[67] | - |
| PBE0[49] | - |
| PW6B95[68] | - |
| BHLYP[9] | ✓ |
| B3LYP(0.5FE) | ✓ |
| PBE0(0.5FE) | ✓ |
| **Self-interaction correction:** | |
| PBE-SIC/2[19] | - |
| PBE-SIC[18] | ✓ |
| **Range-Separated hybrids:** | |
| CAM-B3LYP[69] | - |
| $\omega$B97M-D3BJ[70] | - |
| $\omega$B97X-D3BJ[70] | - |
| **Double hybrids:** | |
| B2PLYP[52] | - |
| B2GPPLYP[71] | ✓ |
| DSD-BLYP[51] | ✓ |
| DSD-PBEP86[50] | ✓ |
| **Neural network:** | |
| DM21[72] | - |
| DM21m[72] | - |
| DM21mc[72] | - |
| DM21mu[72] | - |

# Discussion

The balance between localised and delocalised charge distribution of the $DMP^+$ ion and 3s Rydberg excited state of DMP represents a sensitive and challenging test of electronic density functionals. They represents a rare case where both a delocalised and localised state can be present on the same adiabatic energy surface. While it is clear from experimental measurements that a localised state exists for the Rydberg DMP,[29] it most likely does not exist for the $DMP^+$ ion. The energy surface of $DMP^+$ must in any case be relatively flat in the region of the localised state in order for the Rydberg electron to induce such a minimum since the Rydberg electron is highly dispersed in space. The various density functionals tested here give quite different shape for the $DMP^+$ surface defined as the variation of the energy as a function of the two dihedral angles of the six-membered ring shown in figure 1. Three of the four double hybrid functionals tested here, predict the presence of a local, symmetry broken minimum for the $DMP^+$ ion corresponding to a localised electronic state. Lower on the Jacob's ladder, the generalised gradient approximation functionals, such as the PBE functional, do not produce a localised state and the PBE energy surface shown in figure 1 does not even display energy valleys in the region of the localised state. On the contrary, a hint of a valley lies along the symmetry line. The shape of the surface changes by going to a global hybrid functional with the inclusion of FE and the surface produced with the PBE0 functional where the weight on FE is 0.25 shows a hint of valleys in the direction of the symmetry broken localised state. These become clearer when the weight is increased to 0.32 and a fairly good match is then obtained with the machine learned DM21 functional where the input data base includes data on fractional charge and spin. In order to produce a local minimum on the energy surface, the weight on FE needs to be increased further. With a weight of 0.5 as in either the PBE0(0.5FE) or the BHLYP functionals, a distinct energy minimum is formed corresponding to a localised state. This evolution of the shape of the energy surface as a function of increased weight on FE is a reflection of the extent to which the self-interaction in the estimate of the classical Coulomb interaction from

the total electron density is canceled out and even eventually overcorrected. The FE term in the hybrid functionals contains self-interaction of opposite sign to the one in the classical Coulomb interaction as well as the infinite range exchange terms. The self-interaction in the classical Coulomb interaction favours delocalisation while FE favours localisation. In the extreme case of pure HF, only the localised state is present for the $DMP^+$ ion.[29]

The role played by the self-interaction error can be seen clearly by making an explicit self-interaction correction to the PBE functional. The orbital-by-orbital correction proposed by Perdew and Zunger[18] is exact for a system with only one electron, but does not take many-body effects into account. The full correction is needed in order to obtain the correct -1/$r$ long range form of the effective potential of an electron, an important feature for accurate representation of diffuse orbitals in Rydberg excited states and loosely bound anions.[21,22] But, it has been shown,[19,20] and justified by reference to the adiabatic connection formula, as in the original hybrid functional,[9] that the correction term should be scaled by 0.5. This gives significantly improved results for atomisation energy of molecules and band gap of solids. It has also been shown to give good results for the delicate balance between different energy surfaces of the Mn dimer.[73] One of the interesting results from the present analysis of the energy surface of the $DMP^+$ ion is that full correction applied to PBE gives results that are similar to having a weight of 0.5 on FE in the PBE0(0.5FE) and BHLYP functionals, while scaling the correction by 0.5 is closer to the PBE0 functional where the weight on FE is 0.25.

The energy barrier for a transition from the localised state to the delocalised state of $DMP^+$ turns out to be in the range of 0.02 to 0.045 eV for the functionals where a localised state minimum is present, namely the DSD-PBEP86 double hybrid functional, the BHLYP and PBE0(0.5FE) global hybrid functionals, and the PBE functional with full self-interaction correction applied, PBE-SIC, as shown in table 1. This estimate of the activation energy for PBE-SIC is lower than a previously reported estimate[29] mainly because the calculation is carried out to a better convergence here. The convergence tolerance for the force acting

on the climbing image in the CI-NEB calculations is 0.01 eV/Å in the present case, while it was 0.05 eV/Å in the previous calculation (a default setting in the GPAW software). Improvements in the implementation of PZ-SIC in GPAW in recent years[23–26] has made it possible to reach better convergence. There, the full PZ-SIC was applied in order to obtain the correct -1/$r$ long range form of the effective potential as the goal was in part to obtain an accurate estimate of the Rydberg electron binding energy.[29] The scaling down of the PZ-SIC by a factor of 0.5, i.e. the PBE-SIC/2 functional, eliminates the localised state of $DMP^+$. Optimally, the Rydberg orbital should be subject to full PZ-SIC while a scaled-down correction should be applied to the rest of the orbitals. The difference between the two methods for addressing the self-interaction error in semi-local Kohn-Sham functionals, the inclusion of FE in hybrid functionals and the explicit PZ-SIC, is mainly the off-diagonal terms in the infinite range FE. They ensure the hybrid functionals are unitary invariant and thereby simplify the computational effort while the application of PZ-SIC makes the functional explicitly dependent on the orbital densities rather than just the total electron density.

Whenever possible, tests of density functionals are carried out against results of high-level wave function based approaches. The DMP molecule is, however, large enough to make this a significant challenge. For reference, table 2 also lists results obtained with wave function based multi-reference configuration interaction, MRCI+Q, reported in Ref.[32] As explained there, an energy surface was generated using atomic coordinates obtained from BHLYP calculations because the MRCI+Q calculations require too large computational effort for the structural relaxation. The value of the energy can, therefore, be expected to be a bit higher in general. Clear minima corresponding to the localised state are present on the energy surface presented in Ref.[32] and the overall shape somewhat similar to that obtained with PBE0(0.5FE) and PBE-SIC. From MRCI+Q calculations using the fully relaxed atom coordinates and first order saddle point obtained by BHLYP, the energy of the localised state is found to be 0.38 eV with respect to that of the delocalised state and the energy barrier

0.054 eV, a bit higher than for the density functionals that include FE with a weight of 0.5. Subsequent state averaged calculations carried out by Kaupp and coworkers,[35] however, do not show an energy minimum corresponding to a localised state and it is argued there that the state-specific CASSCF calculation which underlies the MRCI method induces a cusp that leads to an artificial energy barrier in the MRCI+Q calculations.

The energy surface for the Rydberg DMP obtained from the PBE0 functional turns out to be significantly different from the energy surface of the $DMP^+$ ion. Minima corresponding to localised states are present on the Rydberg surface, while they are absent on the cation surface. This is an interesting result since the energy surface of a Rydberg state is often assumed to be quite similar to that of the corresponding cation. This result is in agreement with the reported results of Kaupp and coworkers.[35] For the PBE functional the difference between the two surfaces is not as large and neither one shows a localised state minimum in our calculations. This means that the self-interaction error in the PBE functional needs to be removed to a sufficient extent in order for the presence of the Rydberg electron to induce an energy minimum corresponding to a localised state. Kaupp and coworkers, however, did report a very shallow energy minimum for the PBE functional when the Rydberg was calculated using time-dependent DFT.[35]

The PBE0 energy surface for the Rydberg DMP appears to be qualitatively consistent with the experimental measurements presented in Ref.[32] even though a localised state is not predicted for the cation. An increase in the weight on FE from 0.25 to 0.32 reproduces qualitatively the energy surface generated from the machine learned DM21 functional, as shown in figure 1. A value of 0.5 as in PBE0(0.5FE), shown in figure 2, is apparently too large.

# Conclusions

The energy surfaces of the $DMP^+$ ion and the 3s Rydberg state of DMP show well the balance between delocalised and localised charge distribution and provide valuable tests for the weight of FE in hybrid functionals, or alternatively the extent to which explicit orbital-based self-interaction correction should be included. Using the PBE generalised gradient approximation functional as a basis, the inclusion of FE with a weight of 0.25 as in the PBE0 functional, stabilises localisation enough for the Rydberg energy surface to produce minima corresponding to localised states, a lower one with an equatorial position of a methyl group at the N atom where the hole resides, and a higher one with an axial position. The $DMP^+$ energy surface for PBE0, however, does not show evidence of localised states. This qualitative difference between the cation surface and the Rydberg surface is noteworthy because it is generally assumed that the energy surface of a Rydberg excited state is similar to that of the cation.

When the weight of FE is increased to 0.5, the value in the original hybrid functional, BHLYP,[9] deduced from adiabatic connection and in the PBE0(0.5FE) functional, also the $DMP^+$ energy surface supports a localised state. Similar $DMP^+$ energy surface is obtained when the full PZ-SIC is applied. However, when the SIC is scaled down by a factor of 0.5, which again can be justified from the adiabatic connection, the localised state minimum disappears. There seems to be a rough correspondence between a weight of 0.5 on FE and full SIC on the one hand, and a weight of 0.25 on FE and downscaling of SIC by 0.5 on the other hand.

Given the large data base for training and the emphasis on accurate representation of the variation of the energy as a function of fractional charge, it is likely that the machine learned functional DM21 gives the most accurate estimate of the presence localised charge state. While it does not produce minima on the energy surface of $DMP^+$ for a localised state, it does show clear energy valleys towards those regions, more so than the PBE0 surface. Similar shape can be obtained by increasing the weight on FE to a value of 0.32.

The range-separated hybrid functionals tested do not produce a metastable localised state for $DMP^+$, but most of the double-hybrid functionals do.

## Acknowledgement

This work was funded by the Icelandic Research Fund, grant no. 207014-053 and the University of Iceland Research Fund. The calculations were performed on resources provided by the Icelandic Research E-Infrastructure facility. We thank Vilhjálmur Ásgeirsson, Gianluca Levi, Marta Galyńska and Aleksei Ivanov for helpful discussions and assistance with some of the early stages of this work.

## Supporting Information Available

Additional data on atomic coordinates are available on Zenodo.

## References

(1) Demadis, K. D.; Hartshorn, C. M.; Meyer, T. J. The Localized-to-Delocalized Transition in Mixed-Valence Chemistry. *Chemical Reviews* **2001**, *101*, 2655–2686, PMID: 11749392.

(2) Hankache, J.; Wenger, O. S. Organic Mixed Valence. *Chemical Reviews* **2011**, *111*, 5138–5178.

(3) Heckmann, A.; Lambert, C. Organic Mixed-Valence Compounds: A Playground for Electrons and Holes. *Angewandte Chemie International Edition* **2012**, *51*, 326–392.

(4) Blondin, G.; Girerd, J. J. Interplay of electron exchange and electron transfer in metal polynuclear complexes in proteins or chemical models. *Chemical Reviews* **1990**, *90*, 1359–1376.

(5) Solomon, E. I.; Xie, X.; Dey, A. Mixed valent sites in biological electron transfer. *Chem. Soc. Rev.* **2008**, *37*, 623–638.

(6) Cohen, A. J.; Mori-Sánchez, P.; Yang, W. Challenges for Density Functional Theory. *Chemical Reviews* **2012**, *112*, 289–320.

(7) Bryenton, K. R.; Adeleke, A. A.; Dale, S. G.; Johnson, E. R. Delocalization error: The greatest outstanding challenge in density-functional theory. *WIREs Computational Molecular Science* **2022**, *13*, e1631.

(8) Parthey, M.; Kaupp, M. Quantum-chemical insights into mixed-valence systems: within and beyond the Robin–Day scheme. *Chem. Soc. Rev.* **2014**, *43*, 5067–5088.

(9) Becke, A. D. A new mixing of Hartree–Fock and local density-functional theories. *J. Chem. Phys.* **1993**, *98*, 1372.

(10) Kaupp, M.; Karton, A.; Bischoff, F. A. $[Al2O4]^{-}$, a Benchmark Gas-Phase Class II Mixed-Valence Radical Anion for the Evaluation of Quantum-Chemical Methods. *Journal of Chemical Theory and Computation* **2016**, *12*, 3796–3806.

(11) Klawohn, S.; Kaupp, M.; Karton, A. MVO-10: A Gas-Phase Oxide Benchmark for Localization/Delocalization in Mixed-Valence Systems. *Journal of Chemical Theory and Computation* **2018**, *14*, 3512–3523.

(12) Kaupp, M.; Renz, M.; Parthey, M.; Stolte, M.; Würthner, F.; Lambert, C. Computational and spectroscopic studies of organic mixed-valence compounds: where is the charge? *Phys. Chem. Chem. Phys.* **2011**, *13*, 16973–16986.

(13) Renz, M.; Theilacker, K.; Lambert, C.; Kaupp, M. A Reliable Quantum-Chemical Protocol for the Characterization of Organic Mixed-Valence Compounds. *Journal of the American Chemical Society* **2009**, *131*, 16292–16302.

(14) Renz, M.; Kess, M.; Diedenhofen, M.; Klamt, A.; Kaupp, M. Reliable Quantum Chemical Prediction of the Localized/Delocalized Character of Organic Mixed-Valence Radical Anions. From Continuum Solvent Models to Direct-COSMO-RS. *Journal of Chemical Theory and Computation* **2012**, *8*, 4189–4203.

(15) Renz, M.; Kaupp, M. Predicting the Localized/Delocalized Character of Mixed-Valence Diquinone Radical Anions. Toward the Right Answer for the Right Reason. *The Journal of Physical Chemistry A* **2012**, *116*, 10629–10637.

(16) Kaupp, M.; Gückel, S.; Renz, M.; Klawohn, S.; Theilacker, K.; Parthey, M.; Lambert, C. Electron transfer pathways in mixed-valence paracyclophane-bridged bis-triarylamine radical cations. *Journal of Computational Chemistry* **2016**, *37*, 93–102.

(17) Körzdörfer, T.; Brédas, J.-L. Organic Electronic Materials: Recent Advances in the DFT Description of the Ground and Excited States Using Tuned Range-Separated Hybrid Functionals. *Accounts of Chemical Research* **2014**, *47*, 3284–3291.

(18) Perdew, J. P.; Zunger, A. Self-interaction correction to density-functional approximations for many-electron systems. *Phys. Rev. B* **1981**, *23*, 5048–5079.

(19) Klüpfel, S.; Klüpfel, P.; Jónsson, H. The effect of the Perdew-Zunger self-interaction correction to density functionals on the energetics of small molecules. *J. Chem. Phys.* **2012**, *137*, 124102.

(20) Jónsson, H. Simulation of Surface Processes. *Proceedings of the National Academy of Sciences* **2011**, *108*, 944.

(21) Gudmundsdottir, H.; Zhang, Y.; Weber, P. M.; Jónsson, H. Self-interaction corrected density functional calculations of molecular Rydberg states. *J. Chem. Phys.* **2013**, *139*, 194102.

(22) Zhang, Y.; Weber, P.; Jónsson, H. *J. Phys. Chem. Letters* **2016**, *7*, 2068.

(23) Lehtola, S.; Jónsson, E. Ö.; Jónsson, H. Effect of complex-valued optimal orbitals on atomization energies with the Perdew–Zunger self-interaction correction to density functional theory. *J. Chem. Theory Comput.* **2016**, *12*, 4296.

(24) Ivanov, A. V.; Jónsson, E. Ö.; Vegge, T.; Jónsson, H. Direct Energy Minimization Based on Exponential Transformation in Density Functional Calculations of Finite and Extended System. *Computer Physics Communications* **2021**, *267*, 108047.

(25) Ivanov, A. V.; Levi, G.; Jónsson, E. Ö.; Jónsson, H. Method for Calculating Excited Electronic States Using Density Functionals and Direct Orbital Optimization with Real Space Grid or Plane-Wave Basis Set. *J. Chem. Theory Comput.* **2021**, *17*, 5034.

(26) Mortensen, J. J.; et al. GPAW: Open Python Package for Electronic-structure Calculations. *J. Chem. Phys.* **2024**, *160*, 092503.

(27) Gudmundsdottir, H.; Jónsson, E. Ö.; Jónsson, H. Calculations of Al dopant in $\alpha$-quartz using a variational implementation of the Perdew–Zunger self-interaction correction. *New J. Phys.* **2015**, *17*, 083006.

(28) Kirkpatrick, J. et al. Pushing the frontiers of density functionals by solving the fractional electron problem. *Science* **2021**, *374*, 1385–1389.

(29) Cheng, X.; Zhang, Y.; Jónsson, E. O.; Jónsson, H.; Weber, P. M. Charge localization in a diamine cation provides a test of energy functionals and self-interaction correction. *Nature Communications* **2016**, *7*, 11013.

(30) Perdew, J. P.; Burke, K.; Ernzerhof, M. Generalized Gradient Approximation Made Simple. *Phys. Rev. Lett.* **1996**, *77*, 3865–3868.

(31) Perdew, J. P.; Burke, K.; Ernzerhof, M. Generalized Gradient Approximation Made Simple [Phys. Rev. Lett. 77, 3865 (1996)]. *Phys. Rev. Lett.* **1997**, *78*, 1396–1396.

(32) Gałyńska, M.; Ásgeirsson, V.; Jónsson, H.; Bjornsson, R. Localized and Delocalized States of a Diamine Cation: Resolution of a Controversy. *The Journal of Physical Chemistry Letters* **2021**, *12*, 1250–1255.

(33) Ali, Z.; Aquino; F.W.; Wong, B. The diamine cation is not a chemical example where density functional theory fails. *Nature Communications* **2018**, *9*, 4733.

(34) Cheng, X.; Zhang, Y.; Jónsson, E. Ö.; Jónsson, H.; Weber, P. M. Reply to: "The diamine cation is not a chemical example where density functional theory fails". *Nature Communications* **2018**, *9*, 5348.

(35) Reimann, M.; Kirsch, C.; Sebastiani, D.; Kaupp, M. Rydberg electron stabilizes the charge localized state of the diamine cation. *Nat. Comm.* **2024**, *15*, 293.

(36) Sigurdarson, A. E.; Schmerwitz, Y. L. A.; Tveiten, D. K. V.; Levi, G.; Jónsson, H. Orbital-optimized Density Functional Calculations of Molecular Rydberg Excited States with Real Space Grid Representation and Self-Interaction Correction. *J. Chem. Phys.* **2023**, *159*, 214109.

(37) Dunning, T. H. Gaussian basis sets for use in correlated molecular calculations. I. The atoms boron through neon and hydrogen. *The Journal of Chemical Physics* **1989**, *90*, 1007–1023.

(38) Kendall, R. A.; Dunning, T. H.; Harrison, R. J. Electron affinities of the first-row atoms revisited. Systematic basis sets and wave functions. *The Journal of Chemical Physics* **1992**, *96*, 6796–6806.

(39) Neese, F. Software update: The ORCA program system—Version 5.0. *WIREs Computational Molecular Science* **2022**, *12*, e1606.

(40) Sun, Q. et al. Recent developments in the PySCF program package. *The Journal of Chemical Physics* **2020**, *153*, 024109.

(41) Sun, Q.; Berkelbach, T. C.; Blunt, N. S.; Booth, G. H.; Guo, S.; Li, Z.; Liu, J.; McClain, J. D.; Sayfutyarova, E. R.; Sharma, S.; Wouters, S.; Chan, G. K.-L. PySCF: the Python-based simulations of chemistry framework. *WIREs Computational Molecular Science* **2018**, *8*, e1340.

(42) Sun, Q. Libcint: An efficient general integral library for Gaussian basis functions. *Journal of Computational Chemistry* **2015**, *36*, 1664–1671.

(43) Levi, G.; Ivanov, A. V.; Jónsson, H. Variational Density Functional Calculations of Excited States via Direct Optimization. *J. Chem. Theo. Comput.* **2020**, *16*, 6968.

(44) Levi, G.; Ivanov, A. V.; Jónsson, H. Variational Calculations of Excited States via Direct Optimization of the Orbitals in DFT. *Faraday Discussions* **2020**, *224*, 448.

(45) Henkelman, G.; Uberuaga, B. P.; Jónsson, H. A climbing image nudged elastic band method for finding saddle points and minimum energy paths. *The Journal of Chemical Physics* **2000**, *113*, 9901–9904.

(46) Henkelman, G.; Jónsson, H. Improved tangent estimate in the nudged elastic band method for finding minimum energy paths and saddle points. *The Journal of Chemical Physics* **2000**, *113*, 9978–9985.

(47) Ásgeirsson, V.; Birgisson, B. O.; Bjornsson, R.; Becker, U.; Neese, F.; Riplinger, C.; Jónsson, H. Nudged Elastic Band Method for Molecular Reactions Using Energy-Weighted Springs Combined with Eigenvector Following. *Journal of Chemical Theory and Computation* **2021**, *17*, 4929–4945.

(48) MATLAB version 9.8.0.1359463 (R2020a) Update 1. The Mathworks, Inc.: Natick, Massachusetts, 2020.

(49) Perdew, J. P.; Ernzerhof, M.; Burke, K. Rationale for mixing exact exchange with density functional approximations. *J. Chem. Phys.* **1996**, *105*, 9982.

(50) Kozuch, S.; Martin, J. M. L. DSD-PBEP86: In Search of the Best Double-Hybrid DFT with Spin-Component Scaled MP2 and Dispersion Correction. *Physical Chemistry Chemical Physics* **2010**, *12*, 2940–2953.

(51) Kozuch, S.; Martin, J. M. L. Spin-component-scaled double hybrids: An extensive search for the best fifth-rung functionals blending DFT and perturbation theory. *Journal of Computational Chemistry* **2011**, *32*, 2325–2338.

(52) Grimme, S. Semiempirical GGA-type density functional constructed with a long-range dispersion correction. *Journal of Computational Chemistry* **2006**, *27*, 1787–1799.

(53) Maier, T. M.; Arbuznikov, A. V.; Kaupp, M. Local hybrid functionals: Theory, implementation, and performance of an emerging new tool in quantum chemistry and beyond. *WIREs Computational Molecular Science* **2019**, *9*, e1378.

(54) Becke, A. D. Density-functional exchange-energy approximation with correct asymptotic behavior. *Physical Review A* **1988**, *38*, 3098–3100.

(55) Lee, C.; Yang, W.; Parr, R. G. Development of the Colle-Salvetti correlation-energy formula into a functional of the electron density. *Physical Review B* **1988**, *37*, 785–789.

(56) Becke, A. D. Density-functional exchange-energy approximation with correct asymptotic behavior. *Physical Review A* **1988**, *38*, 3098–3100.

(57) Perdew, J. P. Density-functional approximation for the correlation energy of the inhomogeneous electron gas. *Physical Review B* **1986**, *33*, 8822–8824.

(58) Handy, N. C.; Cohen, A. J. Left-right correlation energy. *Molecular Physics* **2001**, *99*, 403–412.

(59) Ernzerhof, M.; Scuseria, G. E. Assessment of the Perdew–Burke–Ernzerhof exchange-correlation functional. *The Journal of Chemical Physics* **1999**, *110*, 5029–5036.

(60) Perdew, J. P.; Wang, Y. Accurate and Simple Analytic Representation of the Electron-Gas Correlation Energy. *Physical Review B* **1992**, *45*, 13244–13249.

(61) Hammer, B.; Hansen, L. B.; Nørskov, J. K. Improved adsorption energetics within density-functional theory using revised Perdew-Burke-Ernzerhof functionals. *Physical Review B* **1999**, *59*, 7413–7421.

(62) Lin, Y.-S.; Li, G.-D.; Mao, S.-P.; Chai, J.-D. Long-range corrected hybrid density functionals with improved dispersion corrections. *Journal of Chemical Theory and Computation* **2013**, *9*, 263–272.

(63) Tao, J.; Perdew, J. P.; Staroverov, V. N.; Scuseria, G. E. Climbing the Density Functional Ladder: Nonempirical Meta–Generalized Gradient Approximation Designed for Molecules and Solids. *Physical Review Letters* **2003**, *91*, 146401.

(64) Perdew, J. P.; Ruzsinszky, A.; Csonka, G. I.; Vydrov, O. A.; Scuseria, G. E.; Constantin, L. A.; Zhou, X.; Burke, K. Restoring the Density-Gradient Expansion for Exchange in Solids and Surfaces. *Physical Review Letters* **2009**, *103*, 026403.

(65) Furness, J. W.; Kaplan, A. D.; Ning, J.; Perdew, J. P.; Sun, J. Accurate and Numerically Efficient r2SCAN Meta-Generalized Gradient Approximation. *Journal of Physical Chemistry Letters* **2020**, *11*, 8208–8215.

(66) Staroverov, V. N.; Scuseria, G. E.; Tao, J.; Perdew, J. P. Comparative assessment of a new nonempirical density functional: Molecules and hydrogen-bonded complexes. *Journal of Chemical Physics* **2003**, *119*, 12129–12137.

(67) Stephens, P. J.; Devlin, F. J.; Chabalowski, C. F.; Frisch, M. J. Ab Initio Calculation of Vibrational Absorption and Circular Dichroism Spectra Using Density Functional Force Fields. *Journal of Physical Chemistry* **1994**, *98*, 11623–11627.

(68) Zhao, Y.; Truhlar, D. G. Design of Density Functionals That Are Broadly Accurate for Thermochemistry, Thermochemical Kinetics, and Noncovalent Interactions. *Journal of Chemical Physics* **2005**, *123*, 161103.

(69) Yanai, T.; Tew, D. P.; Handy, N. C. A new hybrid exchange–correlation functional using the Coulomb-attenuating method (CAM-B3LYP). *Chemical Physics Letters* **2004**, *393*, 51–57.

(70) Lin, Y.-S.; Li, G.-D.; Mao, S.-P.; Chai, J.-D. Long-range corrected hybrid density functionals with improved dispersion corrections. *Journal of Chemical Theory and Computation* **2016**, *12*, 1280–1291.

(71) Karton, A.; Tarnopolsky, A.; Lamère, J.-F.; Schatz, G. C.; Martin, J. M. L. Highly Accurate First-Principles Benchmark Data Sets for the Parametrization and Validation of Density Functional Theory Functionals. *Journal of Chemical Physics* **2008**, *129*, 124114.

(72) Kirkpatrick, J. et al. Pushing the frontiers of density functionals by solving the fractional electron problem. *Science* **2021**, *374*, 1385–1389.

(73) Ivanov, A. V.; Ghosh, T.; Jónsson, E. Ö.; Jónsson, H. Mn Dimer can be Described Accurately with Density Functional Calculations when Self-interaction Correction is Applied. *J. Phys. Chem. Letters* **2021**, *12*, 4240.